

INVESTIGATION AND DEVELOPMENT TOWARDS
A CLINICALLY PRACTICAL PROTON COMPUTED
TOMOGRAPHY SYSTEM FOR TREATING CANCER

by

JOHN VINCENT COTTERILL

A thesis submitted to
the University of Birmingham
for the degree of
DOCTOR OF PHILOSOPHY

Department of Particle Physics
School of Physics and Astronomy
College of Engineering and Physical Sciences
University of Birmingham
January 2021

UNIVERSITY OF
BIRMINGHAM

University of Birmingham Research Archive

e-theses repository

This unpublished thesis/dissertation is copyright of the author and/or third parties. The intellectual property rights of the author or third parties in respect of this work are as defined by The Copyright Designs and Patents Act 1988 or as modified by any successor legislation.

Any use made of information contained in this thesis/dissertation must be in accordance with that legislation and must be properly acknowledged. Further distribution or reproduction in any format is prohibited without the permission of the copyright holder.

Abstract

Imaging of a patient for the planning of a proton therapy treatment for cancer is currently conducted using x-ray Computed Tomography (CT). Uncertainties arise from the conversion of the measured parameters of the CT to proton stopping powers required for treatment planning. This conversion results in a 3.5% uncertainty on the range of the proton and is equivalent to a 1.2cm uncertainty on a 230MeV proton beam in water. This uncertainty on the distal edge of the beam can result in excess dose to healthy tissue or insufficient dose to the tumour.

The uncertainties associated with this image conversion may be removed if the proton stopping powers are measured directly using proton Computed Tomography (pCT). No such system currently exists in operation clinically. The high spatial density of incident protons, high current, and large energy range, make designing a system difficult, especially whilst remaining practical for mounting on a rotating gantry.

This work describes studies into proposed solutions and specifications of a device suitable for clinical operation. Individual proton tracking is achieved using silicon strip trackers; two placed before the patient, and two after. Each tracker consists of three silicon strip sensors, in an x-u-v orientation, with each layer rotated at 120° with respect to each other. Simulations were performed using Geant4 to optimise the strip pitch and silicon thickness through examination of the achievable position and tracking resolutions. These studies found that a strip pitch of $200\mu\text{m}$ and a silicon thickness of $150\mu\text{m}$ was optimal for the tracking system when considering additional clinical constraints.

One proposed solution for a more compact system was the Hybrid Approach, in which the energy is measured using a single layer of silicon pixels. The average signal for each pixel was assigned to every proton traversing it, from which the Water Equivalent Path Length (WEPL) could be inferred. This system configuration was examined using simulation and experiment, with promising results for the approach, but distortion to the internal structures of an imaged object in a 2D proton radiograph was observed. This reduction in image quality was confirmed to originate from the proton scatter.

A deeper examination of the proton scatter led to the development of an alternative Scattering Approach to pCT. This approach used the variation in the plane projected scattering angle to produce an image. The device using this approach is more clinically practical as only proton tracking devices are required. Results from both simulation and experiment showed significant improvements to the position of internal structures in 2D radiographs in comparison to the Hybrid approach. A 3D reconstruction algorithm was also developed to produce a pCT, and compared with an x-ray CT, both using experimental data. The reconstructed image showed internal structure on a $200\mu\text{m}$ scale, an improvement of five times that which is typically found clinically with x-rays.

For Mum.

For your endless love, support, and painful days of proofreading.

Acknowledgements

This has been one of the most intense, inspiring, focused and exciting periods of my life. I have had the most amazing opportunity to contribute to a truly impactful field, with support and guidance from some amazing people. It has not been a straight forward journey, and so my utmost and sincere thanks go to those who have supported me along the way.

To my Supervisors, Phil, Stuart, and Tony, I will be forever grateful for you giving me the opportunity to do this work. Your guidance and support throughout this time has been incredibly valuable to me.

Phil, you are a true God of knowledge. It is always reassuring having you in a meeting, knowing that you are poised to stop any bad ideas progressing, or answering questions no one else has an answer to. Your dedication for collaboration is something which is sadly too often missing in research, and so you remain a true inspiration.

Stuart, you are the embodiment of what the NHS and research should be. Your passion for patient care is unquestionable, alongside your dedication to developing new techniques through research. It has been so valuable to have your clinical expertise to hand, which has helped to keep the focus on the end goal of this research.

Tony, you deserve every recognition for being an outstanding Supervisor. From the first day, you were there guiding and teaching me, even when you weren't officially my Supervisor at the time. You have always been around to support me with experimental

work, and never once faltered in motivation, despite what seemed like endless rescheduling on the cyclotron. I really hope one day, you finally manage to catch 'em all.

My sanity would have been lost if it wasn't for some of you. To Alasdair, Andy, Jamés, Tim, Matt, Briglin, Kendrick, Elliot, Russell, Jack, Rob, Ryan, Robbie, Gov, Dan, Nandish, Sam, Sam, and Marc, I may not have ever shared an office with most of you, but that never stopped me joining you for lunch. Some of you have finished, some finishing, and some yet to finish. So I say to you "well done", "good luck", and "try not to quit". I do know people who aren't Particle Physicists though, so for Alison, Katy, Zoe, and Tammy, I thank you for accompanying us gents for drinks, meals, and nights out.

To the rest of the Party, Alasdair, Alison, Robbie, Tom, and Amelia, I give my thanks. Our adventures never go as planned, but remain some of my favourite times, and were a welcome respite from the isolation of lockdown.

Lindsey, thank you for being someone to talk to about Physics and coffee, and complain about lab and my lack of a hedgehog. I still can't believe Pierre's is closed on Wednesdays.

Alice, you have my eternal thanks for your support, which undoubtedly kept me above water through challenging times.

Mum, words cannot explain how much I love you. Not once have you faltered with your love, support, interest, dedication, encouragement and guidance. You are everything a Mother should be, and more.

Lastly, and possibly the most important of all, my thanks go to Miss Silvia. I would never have finished writing this without you.

“I must continue on the path I have taken now. If I don’t do anything, if I don’t study, if I don’t go on seeking any longer, I am lost. Then woe is me. That is how I look at it: to continue, to continue, that is what is necessary.

But you will ask, What is your definite aim?

That aim becomes more definite, will stand out slowly and surely, as the rough draft becomes a sketch, and the sketch becomes a picture - little by little, by working seriously on it, by pondering over the idea, vague at first, over the thought that was fleeting and passing, till it gets fixed.”

- Vincent van Gogh

July 1880 [1]

Contents

1	Introduction to Cancer and Radiotherapy	1
1.1	Cancer	1
1.1.1	Hallmarks of Cancer	2
1.2	Radiotherapy	4
1.2.1	Absorbed Dose	5
1.2.2	Therapeutic Ratio	6
1.2.3	Fractionation and Non-Uniform Doses	7
1.2.4	Volume Definitions	8
1.3	Photon Interactions with Matter	9
1.3.1	Coherent Scattering	10
1.3.2	Photoelectric Effect	10
1.3.3	Compton Scattering	12
1.3.4	Pair Production	13
1.3.5	Interaction Mechanism Dominance	14
1.3.6	Photon Dose Distribution	15
1.4	Photon Therapy Techniques	17
1.4.1	3DCRT	17
1.4.2	IMRT	19
1.4.3	IGRT	19
1.4.4	VMAT	20
1.5	Proton Therapy	20

1.5.1	Proton Interaction with Matter	21
1.5.1.1	Inelastic Coulomb Interaction	21
1.5.1.2	Elastic Coulomb Interaction	22
1.5.1.3	Nuclear Interaction	22
1.5.2	Stopping Power	23
1.5.3	Proton Dose Distribution - The Bragg Peak	24
1.5.4	Proton Range	25
1.5.5	Linear Energy Transfer	27
1.5.6	The Advantage of Proton Therapy	27
1.5.7	Heavy Ion Therapy	30
2	Particle Detection	32
2.1	Semiconductors	34
2.1.1	Energy Band Theory	34
2.1.2	Conductors, Semiconductors and Insulators	35
2.1.3	Doping	36
2.1.4	Charge Carrier Migration	39
2.1.5	A p-n Junction	40
2.2	Silicon Strip Sensors	43
2.3	MOSFET	45
2.4	Signal Processing	46
2.4.1	Readout Architectures	48
2.5	Ambiguities	49
2.6	Silicon Pixel Sensors	51
2.6.1	Pixel Readout Architecture	53
3	Proton Computed Tomography	55
3.1	Motivation for Proton Computed Tomography	55
3.2	Stoichiometric Calibration	57

3.3	Proton Stopping Power Uncertainties	58
3.4	General pCT System Layout	60
3.5	Water Equivalent Path Length	61
3.5.1	WEPL Uncertainty	62
3.5.1.1	Energy Measuring RERD	63
3.5.1.2	Range Measuring RERD	64
3.6	PRaVDA	65
3.6.1	Tracking Detectors	65
3.6.2	Range Telescope	68
3.6.3	Phase Sweep	69
3.6.4	Data Readout	70
3.6.5	Track Reconstruction	71
3.6.6	Super Simulation (SuSi)	73
3.7	OPTIma	75
3.7.1	Overview	75
3.7.2	Design Challenges	75
4	Optimal Parameters for a Silicon Strip Tracker used for Proton Computed Tomography	78
4.1	Introduction	78
4.2	Simulation Set-up	80
4.3	Analysis Method	81
4.4	Results	83
4.5	Discussion	84
4.5.1	Position Resolution	84
4.5.2	Tracking Resolution	89
4.6	Conclusions	91

5 Investigation of a Novel Hybrid System for Proton Computed Tomography	93
5.1 Introduction	93
5.2 System Set-up	96
5.2.1 Beam Set-up	96
5.2.1.1 Broad Beam	97
5.2.1.2 Moving Collimator	98
5.2.1.3 Beam Distributions	99
5.2.2 Trackers	99
5.2.3 Phantoms	100
5.2.3.1 Balsa Wood Phantom	100
5.2.3.2 Perspex Phantom	102
5.2.3.3 Calibration Arms	104
5.2.4 Pixel Sensors	104
5.2.4.1 Priapus	104
5.2.4.2 LASSENA	106
5.2.4.3 Pixel Sensor Simulation Model	107
5.3 Analysis Method	107
5.4 Calibration	109
5.4.1 Calibration Methods	110
5.4.1.1 Calibration using Reconstructed Tracks and Normalisation	111
5.4.2 Calibration using Hits in Tracker 3 without Normalisation	111
5.4.3 Calibration Methods Comparison	112
5.5 Balsa Phantom Study	114
5.5.1 Set-up	114
5.5.2 Simulated Calibration	116
5.5.3 Simulated Projection	116
5.5.4 Experimental Calibration	120

5.5.5	Experimental Projection	120
5.6	Perspex Phantom Study	122
5.6.1	Motivation	122
5.6.2	Set-up	123
5.6.3	Simulated Calibration	127
5.6.4	Simulated Projection	127
5.6.4.1	Projection to the Phantom Plane	129
5.6.4.2	Insert Position	130
5.6.5	Experimental Calibration	132
5.6.6	Experimental Projection	133
5.7	Conclusions	134
6	Using Proton Scattering Information to Improve Imaging	137
6.1	Introduction	137
6.2	Scattering Theory	139
6.3	Modelling the Scatter	141
6.3.1	Outline	141
6.3.2	Scattering Model Process	141
6.3.3	Scattering Model Results	143
6.4	A Tracking Only Approach to pCT	146
6.4.1	Motivation	146
6.4.2	Measuring Scattering Parameters	147
6.4.3	Scattering Calibration	149
6.4.4	Balsa Phantom Results	151
6.4.5	Perspex Phantom Results	158
6.4.6	Experimental pCT	162
6.4.6.1	A Simple pCT Reconstruction Algorithm	163
6.4.6.2	pCT Image	164
6.4.6.3	xCT	165

6.5	Conclusions	167
7	Conclusions and Outlook	170

List of Figures

1.1	The changes required to a cell for it to become a cancer [6].	2
1.2	Example sigmoid curves representing the Tumour Control Probability (TCP) and the Normal Tissue Complication Probability (NTCP) [13].	7
1.3	A diagram representing a prostate tumour treatment plan with GTV, CTV, PTV and OAR volumes [9].	10
1.4	The coherent scattering process where an incident photon is scattered at a small angle with little to no energy change.	11
1.5	The photoelectric interaction of a photon with an atom. Nuclei are represented in blue and electrons in green.	11
1.6	The Compton interaction of an incident photon with an electron.	12
1.7	The process of pair production where an incident photon interacts with a nucleus to create an electron and a positron.	14
1.8	The dominant photon interaction mechanisms for differing energy and atomic number of the material traversed [16]. σ_f , σ_C and σ_p are the photoelectric effect, Compton and pair production cross sections which represent the probability of each interaction occurring.	15
1.9	The energy spectra of photons for a 100kV beam used for imaging, and a 6MV beam used for treatment [9].	16

1.10	The relationship between the dose of a photon beam and the depth through a patient. The region from 0 to z_{max} shows the dose buildup region and ends at the point of maximum dose, D_{max} (normalised to 100). D_s and D_{ex} are the entry and exit doses to the patient respectively [13].	17
1.11	Dose maps of 3DCRT and IMRT treatment plans for a given tumour volume [19].	18
1.12	The dominant interaction mechanisms of protons with matter in proton therapy [27].	22
1.13	Relative dose as a function of depth for a 36MeV proton beam through Perspex. The red curve is the dose determined from Geant4 simulation. The blue points are measurements made on the Birmingham beamline. . .	24
1.14	The fluence of a proton beam through water which has been normalised to the fluence near the end of range [27]. Fluence is initially affected most strongly by nuclear interactions. Absorption of protons within the medium dominates once the protons have deposited most of their energy.	26
1.15	A comparison of Linear Energy Transfer (LET) between low LET (photons) and high LET (protons at the end of their range) particles [9].	28
1.16	Dose map of the same region shown in Figure 1.11b with a proton treatment [19].	28
1.17	Relative dose as a function of depth for a 3480MeV carbon ion beam through water. The dose has been determined using Geant4 simulation and compared with similar results in literature [38].	30
2.1	The normalised probability distribution describing energy loss, Δ , per micron of 500MeV pions in silicon. The most probable value is $\frac{\Delta_p}{x}$ and w is the full width at half maximum [42].	33
2.2	A schematic diagram of the energy levels in an atom, hypothetical molecule, and a crystal structure for lithium [46].	34

2.3	A simplified representation of the band gap separation between the valence and conduction bands for an insulator, semiconductor and conductor. . . .	36
2.4	A schematic representation of the diamond lattice structure of pure silicon and silicon with impurities. Each atom forms 4 covalent bonds to its neighbours.	37
2.5	A schematic representation of the band gap of n-type, intrinsic and p-type semiconductors [41]. Excitation from an energy state within the forbidden region results in an electron and a fixed positive ion, or a hole and a fixed negative ion.	38
2.6	A p-n junction in equilibrium [44]. Mobile charge carriers are indicated with circles and combine within the depletion region. The remaining immobile ions set up an opposing electric field which limits further combination. . .	40
2.7	The distribution of charge, electric field and potential at a boundary between a p-type and n-type semiconductor.	41
2.8	A schematic diagram of a silicon strip sensor under a reverse bias voltage with incomplete depletion.	44
2.9	The behaviour of an ideal MOSFET with different voltages on the gate [52].	45
2.10	A schematic diagram of signal processing by electronics from a single channel of a detector. A signal is generated in a channel which gets integrated by a preamplifier, shaped by a pulse shaper (giving the signal a decay and rise time of τ_d and τ_i respectively) and digitised for readout [53].	47
2.11	A schematic representation of the superposition of signals which have not decayed sufficiently (left) and those which have (right) for accurate signal size analysis. [53].	48
2.12	Schematic representation of the problem with x-y configuration due to ghost hits and the alternative x-u-v configuration adopted for tracking to reduce ambiguities.	50

2.13	A schematic representation of the simplest MAPS design with only NMOS transistors. Additional well structures can be added to achieve full CMOS capability.	52
2.14	A circuit diagram showing the structure of the 3T readout architecture for a silicon pixel device [56].	53
3.1	A calibration curve for the conversion of HU to RSP. The solid line (A) shows the Stoichiometric calibration method. Lines B and C represent the tissue substitute calibration method for Mylar/Melinex/PTFE and B110/SB5 materials respectively. The square points are calculations based on tissue substitute materials and the stars represent calculations based on the chemical composition of real tissues [63].	58
3.2	A schematic representation of a pCT system comprising tracking planes and a Residual Energy Range Detector used to image a phantom [64]. . . .	61
3.3	The PRaVDA system showing proximal and distal trackers, phantom, and the Range Telescope [68].	65
3.4	A single PRaVDA silicon strip layer showing readout from both sides. Each arrow represents 128 channels read out by an ASIC.	66
3.5	Images showing the mounting of silicon strip layers on 12mm thick aluminium stiffeners and inside a tracker unit.	67
3.6	A cyclotron clocking waveform showing the regular structure of proton emission.	69
3.7	Phase sweep relation between the phase delay and track reconstruction efficiency of the system.	71
3.8	Diagrams representing the reconstruction of proton hits in a tracker and complete tracks through the PRaVDA trackers.	73
4.1	The simulation set-up used for the studies to optimise strip pitch and silicon thickness. TP refers to the Truth Planes.	80

4.2	A schematic representation of the separation between the reconstructed and true proton positions through a plane.	82
4.3	1D and 2D distributions of the difference between the reconstructed and true position of a proton on a plane. Reconstruction at a tracker's u-plane gives the position resolution, and reconstruction at a truth plane after track projection gives the tracking resolution.	83
4.4	The position resolution as a function of incident proton energy for protons reconstructed in Tracker 1.	85
4.5	The position resolution as a function of incident proton energy for protons reconstructed in Tracker 4.	85
4.6	The tracking resolution as a function of incident proton energy for protons projected to Truth Plane 1 using reconstructed hit positions in Trackers 1 and 2.	86
4.7	The tracking resolution as a function of incident proton energy for protons projected to Truth Plane 2 using reconstructed hit positions in Trackers 1 and 2.	86
4.8	The tracking resolution as a function of incident proton energy for protons projected to Truth Plane 3 using reconstructed hit positions in Trackers 3 and 4. Note that the y-axis range differs from Figures 4.6 and 4.7 for clarity of the results.	87
4.9	The tracking resolution as a function of incident proton energy for protons projected to Truth Plane 4 using reconstructed hit positions in Trackers 3 and 4. Note that the y-axis range differs from Figures 4.6 and 4.7 for clarity of the results.	87
5.1	Set-up of the PRaVDA Hybrid system on the Birmingham beamline. . . .	97
5.2	Geant4 model of a moving collimator with a 6mm aperture. Red represents aluminium and blue represents tantalum.	98

5.3	Distribution of protons in a broad and a pseudo-spot scanned beam on the Birmingham MC40 cyclotron.	100
5.4	The balsa wood phantom. Green represents Perspex, orange represents air and white represents balsa wood.	101
5.5	Schematic diagrams of the hollow Perspex phantom.	103
5.6	Schematic diagrams of the calibration arms comprising various thicknesses of Perspex.	105
5.7	Normalisation process using reconstructed hits in Priapus with simulated data.	109
5.8	System set-up on the Birmingham MC40 cyclotron for calibration.	110
5.9	The method of determining the average signal per proton within a pixel. The red region in Figure 5.9a shows the region of interest containing the pixels considered for the histogram shown in Figure 5.9b.	112
5.10	An alternative calibration method which uses proton hits in Tracker 3 to determine the average number of protons per pixel.	113
5.11	A calibration curve obtained using two alternative methods using simulated data. The blue points shows the average signal (Digital Number) generated per proton after normalisation with reconstructed tracks. The green points show the alternative averaging method which uses an average number of proton hits per pixel in Tracker 3.	113
5.12	Set-up of the balsa phantom experiment and simulation. Dimensions are in mm and the diagram is not to scale.	115
5.13	The calibration curve for the balsa phantom set-up fitted with Equation 5.2 using simulated data.	116
5.14	Average signal (in units of Digital Number) per proton per pixel in Priapus normalised from reconstructed hits in Priapus for broad beam and spot scan simulated data.	117

5.15	Water Equivalent Path Length (WEPL) per proton per pixel in Priapus normalised from reconstructed hits in Priapus for broad beam and spot scan simulated data.	118
5.16	Profiles through the top and bottom halves of the balsa phantom using simulated data. The blue curve represents WEPL based on the geometry of the phantom and relative densities of the materials. The red lines indicate the insert and outermost edges of the phantom.	119
5.17	Calibration curve obtained from experimental data using the balsa phantom set-up. Calibration was performed by counting hits in Tracker 3.	120
5.18	2D distribution of the WEPL of the balsa wood phantom using the calibration curve shown in Figure 5.17 on experimental data.	121
5.19	The average signal per proton (after normalisation) for a projection of the balsa wood phantom using experimental data.	122
5.20	Set-up of the Perspex phantom experiment and simulation. Dimensions are in mm and the diagram is not to scale.	124
5.21	Images of the experimental set-up with the Perspex phantom.	125
5.22	The rotation of the Perspex phantom in relation to the proton beam. . . .	126
5.23	2D distributions of the average signal per proton of the Perspex phantom at two orientations using simulated data. Inserts are aligned perpendicular and parallel to the beam for Figures 5.23a and 5.23b respectively.	128
5.24	2D distributions of the WEPL per proton of the Perspex phantom at two orientations using simulated data. Inserts are aligned perpendicular and parallel to the beam for Figures 5.24a and 5.24b respectively.	128
5.25	2D distributions of the WEPL of the Perspex phantom at the phantom plane for two orientations using simulated data. Inserts are aligned perpendicular and parallel to the beam for Figures 5.25a and 5.25b respectively.	129

5.26	Line profiles of the WEPL at a value of $y=0\text{mm}$ for the simulated distributions shown in Figure 5.24.	131
5.27	The calibration curve obtained for the Perspex phantom experiment. The region of interest considered to count the number of protons per pixel was located in Tracker 2 due to miss-alignment of the beam.	133
5.28	2D distributions of the total signal in each pixel using experimental data from the Perspex phantom at two orientations. Inserts are aligned perpendicular and parallel to the beam for Figures 5.23a and 5.23b respectively. The alignment of the phantom has been indicated in red. . . .	134
6.1	A schematic representation of the scattering of a proton through a material of thickness, z . The r_{plane} and θ_{plane} parameters represent the distance from entry and the exit angle, projected onto the x or y planes (x and y plane projections are equivalent) [42].	139
6.2	Distributions of the geometric WEPL as a function of position before (6.2a) and after (6.2b) considering the scattering of protons through the balsa phantom.	142
6.3	Distributions of the geometric WEPL as a function of position before (6.3a) and after (6.3b) considering the scattering of protons through the Perspex phantom.	143
6.4	Distributions of the geometric WEPL as a function of position before (6.4a) and after (6.4b) considering the scattering of protons through the Perspex phantom. The phantom is rotated at 90°	143
6.5	1D profiles of the geometric WEPL as a function of position before and after considering the scattering of protons through the balsa phantom. . . .	144
6.6	1D profiles of the geometric WEPL as a function of position before and after considering the scattering of protons through the Perspex phantom. . .	144

6.7	1D profiles of the geometric WEPL as a function of position before and after considering the scattering of protons through the Perspex phantom. The phantom is rotated at 90°.	145
6.8	A schematic diagram showing the scattering parameters for measurement. The proton trajectories are shown in blue and the planes for projection shown in red. r_{plane} is the distance from the position of entry, and θ_{plane} is the angle of scatter, with both parameters projected onto either the x or y plane.	148
6.9	The energy of protons through the simulated system after a 36MeV beam has traversed 1.65mm of silicon (trackers and pixel sensor) and the specified thickness of Perspex. The error bars represent the standard deviation of the proton energy.	150
6.10	A calibration curve relating the thickness of Perspex required to scatter protons according to a Gaussian distribution with standard deviation of θ_{plane}^{rms} using simulated data in both the balsa wood and Perspex phantom set-ups. The red curve is a third order polynomial fit to the data. The green curve shows the square root dependence with Perspex thickness up to 4mm.	151
6.11	The calibration curve relating the thickness of Perspex required to scatter protons according to a Gaussian distribution with standard deviation of θ_{plane}^{rms} for experimental data. This set-up was for imaging the balsa phantom with the system configuration shown in Figure 5.12.	152
6.12	2D distributions of θ_{plane}^{rms} of the balsa phantom for simulated and experimental data.	153
6.13	2D distributions of the sWEPL of the balsa phantom for simulated and experimental data.	153
6.14	1D profiles across the sWEPL distributions in Figure 6.13 across the top half of the balsa phantom containing the Perspex insert.	154

6.15	1D profiles across the sWEPL distributions in Figure 6.13 across the bottom half of the balsa phantom containing the air insert.	154
6.16	A radiograph of the balsa wood phantom obtained experimentally using x-rays. Differing densities within the wood can be seen.	156
6.17	1D profiles across the sWEPL distributions from the top and bottom halves of the balsa wood phantom (same as in Figures 6.14b and 6.15b) alongside an offset geometric WEPL in the balsa wood region. Note that the geometric WEPL data points have been removed at the insert location.	157
6.18	The calibration curve relating the thickness of Perspex required to scatter protons according to a Gaussian distribution with standard deviation of θ_{plane}^{rms} for experimental data. This set-up was for imaging the Perspex phantom with the system configuration shown in Figure 5.20.	159
6.19	2D distributions θ_{plane}^{rms} for 0° and 90° rotations of the Perspex phantom using simulated data.	159
6.20	2D distributions of the sWEPL measured using the θ_{plane}^{rms} parameter for 0° and 90° projections of the Perspex phantom using simulated data.	160
6.21	1D profiles of the sWEPL in Figure 6.20 for 0° and 90° projections of the Perspex phantom using simulated data.	160
6.22	2D distributions θ_{plane}^{rms} for 0° and 90° rotations of the Perspex phantom using experimental data.	161
6.23	2D distributions of the sWEPL measured using the θ_{plane}^{rms} parameter for 0° and 90° projections of the Perspex phantom using experimental data.	161
6.24	1D profiles of the sWEPL in Figure 6.23 for 0° and 90° projections of the Perspex phantom using experimental data.	162
6.25	Axial slices from the experimentally obtained pCT and xCT images of the Perspex phantom.	164
6.26	Reconstructed radiographs of the Perspex phantom from an experimental x-ray CT.	166

6.27 A profile of the pCT and xCT images shown in Figures 6.25a and 6.25b respectively along the central line of the phantom through both inserts. The red line indicates the expected relative values across the profile, with 1 being Perspex, and 0 being air. 166

List of Tables

1.1	Volumes which are defined for the purpose of radiotherapy treatment planning. Their locations are shown in Figure 1.3.	9
3.1	Probability of the number of protons in each cycle at The Christie [24] research room assuming a Poisson distribution.	76

Chapter 1

Introduction to Cancer and Radiotherapy

1.1 Cancer

Cancer Research UK attributes over 25% of deaths in the UK per year to cancer [2]. This makes cancer the single largest contributing cause of death in the UK today. Significant effort is being directed towards finding a cure and improving treatment techniques in order to extend lives. In 2009, an estimated total expenditure on cancer research by partners of the National Cancer Research Institute was £490 million [3]. These UK partners include Cancer Research UK, the Medical Research Council and the Department of Health, amongst many others. In contrast, an estimated £442 million was invested in cancer research in the 2018-2019 financial year by Cancer Research UK alone [4]. This increase in investment and effort towards research has seen the survival rate of cancer double over the last 40 years to 50% [5].

The nature of cancer lies in the abnormal function of cells within the body. Each cell contains DNA (deoxyribonucleic acid) which instructs how these cells divide and behave. Specific sequences within the DNA, called genes, are the instructions for the production

of a specific protein. It is these proteins which are the “building blocks” of cells. If a gene becomes damaged, the instructional code it contains for the production of a protein is incorrect. The protein produced is therefore abnormal and undesirable as it may have an impaired function. In most cases, this should be recognised by the immune system and the cell destroyed by the body. Cases where these abnormalities are not recognised have the opportunity to develop further abnormalities. A cell is deemed to be cancerous once it has attributed to it the specific selection of abnormalities referred to as the “Hallmarks of Cancer” [6].

1.1.1 Hallmarks of Cancer

The hallmarks of cancer, as defined by Douglas Hanahan and Robert Weinberg [6], are a collection of changes which must occur within a cell for it to become cancerous. Figure 1.1 shows the changes required for a cell to become a cancer.

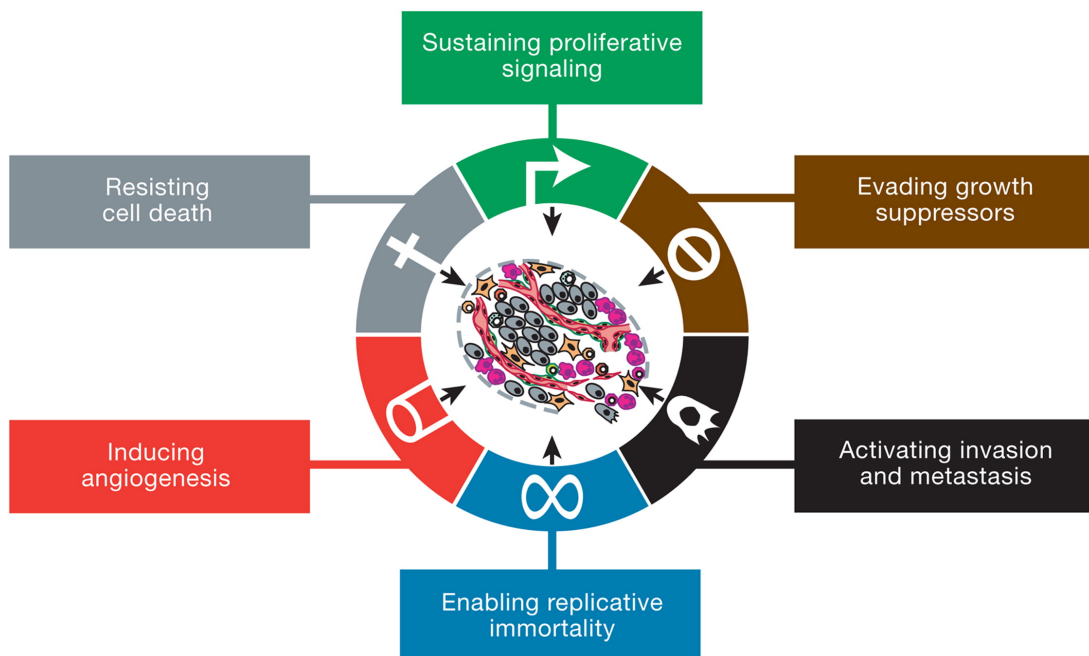


Figure 1.1: The changes required to a cell for it to become a cancer [6].

Two of these changes are that the cells are self sufficient in their growth signals and do

not respond to inhibitory (anti-growth) signals. These changes can be understood to be due to damage in the structure of the control regions of the DNA which regulate the expression of a particular gene.

The third change is that the cells can invade other tissue types and form secondary malignant growths called metastases. A malignant growth is a growth which is able to grow and invade other areas of the body. A benign growth is one which is only able to grow, but not invade. The immune system is designed to recognise and destroy abnormal cells and cells growing in the wrong location in the body. Once a cell is able to avoid the response of the immune system, it remains in the body and can continue growing and invading other areas.

Another change required for a cell to become cancerous is an ability to evade programmed cell death called apoptosis [7]. Cells are required to destroy themselves when forming certain structures in the body such as tubular and hollow structures. They are also required to undergo apoptosis once they approach the end of their life and may begin to malfunction. A cancerous cell, as it is abnormal, should be self deleting. However, its ability to evade such deletion can lead to a potential limitless replicative state, and hence is another characteristic of a cancer cell.

The final hallmark is the cell's ability for sustained angiogenesis [8]. Angiogenesis is the process of forming new blood vessels to supply the cells with blood. This is because as the cancerous cells replicate and form a larger volume, they require their own blood supply. These cells are therefore able to stimulate the growth of blood vessels themselves using genes which are not involved in the maintenance of normal blood vessels for the body.

1.2 Radiotherapy

A malignant tumour in the early stages of development is localised to a given region. In this early stage, surgery can be a successful treatment to completely remove the tumour. As the tumour develops, it metastasises, resulting in further spread throughout the body. A cancer can be difficult to remove entirely with surgery alone once spread. Other treatments such as Chemotherapy and Radiotherapy are often used in combination with surgery to kill the tumour and metastases which have formed.

Radiotherapy is the process of using radiation to destroy cancerous cells and is effective at killing these cells either directly or indirectly. Damage can be caused directly by ionisation (described in more detail in Section 1.3) through either single strand or double strand breaks of the DNA molecule within the nucleus of the cell [9]. Alternatively, the radiation may ionise or excite water molecules contained within the cells which form a chemical species called free radicals. The ionised state of these free radicals can cause subsequent damage to the DNA molecule [10].

This radiation may be delivered internally or externally to the body. An example of internal radiation delivery is Brachytherapy [9] where radioactive sources are implanted inside the body. These sources are typically photon emitters with energies of the order of $<1\text{MeV}$ [9]. Small sources implanted in the tumour allow large local doses to be delivered. The inverse square law gives rise to a high fall off rate of photon density with distance from the source and therefore gives smaller doses to healthy surrounding tissues [9]. Implantation of radioactive sources inside the body can be an invasive technique requiring surgery. This means cancers in sensitive regions such as the brain, spine and organs proximal to critical structures are not treatable with this technique without significant risk. External beam radiotherapy where radiation is delivered externally to the body is often favoured for such cases. Future referrals in this text to radiotherapy will be concerning external beam radiotherapy unless explicitly stated otherwise.

The most common particle used in external beam radiotherapy treatment is the photon. These photons are typically in the form of x-rays and so can be produced on small enough scales to be contained within non-specialist hospitals. Treatments typically use 4-6MV x-rays to treat superficial tumours such as those in the head and neck, and up to 10MV x-rays for deeper tumours such as those in the pelvic region [9]. Other particles are also used for external beam radiotherapy treatments such as electrons, protons, neutrons and carbon nuclei. Treatments using electrons are common in hospitals for treating superficial tumours up to 5cm depth [9]. Their advantage is that they have a high dose fall off rate with depth so can reduce dose delivery to healthy tissues. Protons, neutrons and heavier ions are more difficult to produce and so require specialist facilities. There are advantages to using these particles as opposed to x-rays and these are discussed further in Section 1.5. These techniques however have less supporting clinical evidence for their efficacy due to their shorter period of use in the field of cancer treatment. Good cost effectiveness of these treatments is expected for some cancers located in sensitive regions and paediatrics [11]. The cost effectiveness for treating cancers in patients with a reduced risk of adverse reactions is yet to be statistically conclusive due to the small number of clinical trials and the large cost of the necessary equipment [11].

1.2.1 Absorbed Dose

Absorbed dose is the quantity used in clinical practice to describe the amount of radiation delivered to a patient. Dose is defined as the energy absorbed by a given mass of material and is expressed by the equation

$$Dose[J/kg] = \frac{dE}{dm} \quad , \quad (1.1)$$

where dE is the energy absorbed in a small volume, dV , containing mass, dm . A J/kg is

known as a *gray* (Gy). The unit of Gy is typically used in a clinical environment when describing the dose delivered during a radiotherapy treatment [9].

1.2.2 Therapeutic Ratio

Cancerous cells often demonstrate an impaired ability to repair DNA compared with healthy cells [12]. This characteristic is obtained during a healthy cell's progression to a cancerous cell as it would have otherwise repaired or destroyed itself when becoming abnormal. Cancerous cells consequently have an increased probability of death compared with healthy cells for the same amount of damage from radiation. It is therefore advantageous to maximise the dose being delivered to the tumour in order to inflict as much damage as possible. The probability of cell death in a tumour is described as the Tumour Control Probability (TCP) [9].

The problem with increasing the amount of dose being delivered is that healthy cells are also damaged by the radiation. This unnecessary complication and death of healthy cells is described as the Normal Tissue Complication Probability (NTCP) [9]. The additional damage to healthy cells can cause defects in the DNA and consequent performance of the cell. In some circumstances, the damage caused to the DNA of healthy cells could cause a second cancer. The goal is to obtain the best possible ratio between the TCP and NTCP for an optimal outcome. This ratio is referred to as the therapeutic ratio (TR). A schematic representation of the trend of a TCP and NTCP curve is demonstrated in Figure 1.2.

The curves shown in Figure 1.2 are not well defined and have various proposed empirical models to describe them. Their typical representation is of the form of sigmoid curves. It can be seen that a small increase in dose, represented by the red arrow, results in a large increase in the NTCP represented by the green arrow. For the same increase

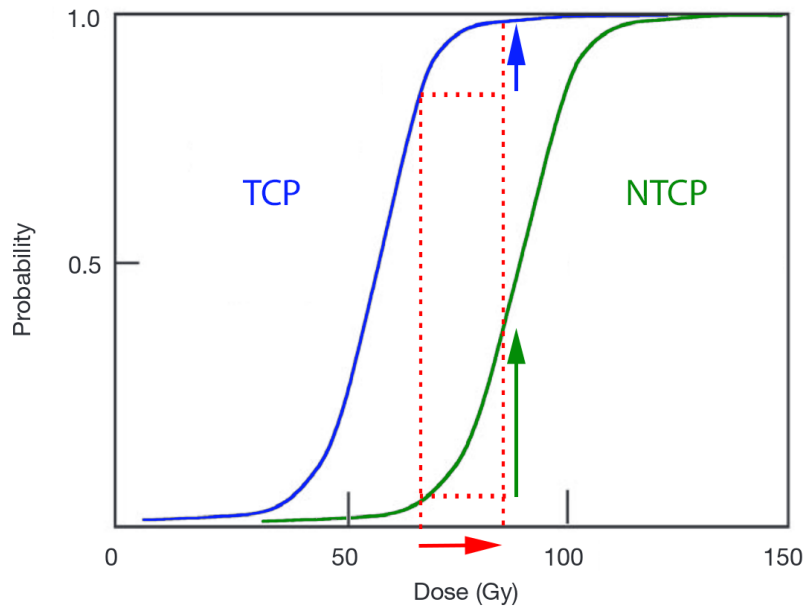


Figure 1.2: Example sigmoid curves representing the Tumour Control Probability (TCP) and the Normal Tissue Complication Probability (NTCP) [13].

in dose, the improvement to the TCP is not so large. This is represented by the blue arrow.

A larger separation of the curves may be achieved by changing the way the radiotherapy is delivered to the tumour. For example, a treatment where the delivered radiation is more conformed to the tumour shape, could result in an increase in the dose where normal tissue complications become more likely (NTCP curve moves to a higher dose). This change is a result of the reduced dose to healthy tissue which surrounds the tumour. The increased separation of the curves means that for the same increase in dose demonstrated by the red arrow, the large increase observed in the NTCP would be reduced, but the TCP improvement would remain the same.

1.2.3 Fractionation and Non-Uniform Doses

Treatments of a given dose are often split into fractions over a period of days to take advantage of healthy cells' resistance to radiation damage [13]. For example, one $2Gy$ fraction every day for 20 days giving a total dose of $40Gy$. This allows time for the

healthy cells to repair themselves before being administered with further radiation. A cancerous cell with its impaired repair ability would recover less during the time between fractions.

A tumour becomes larger as it develops and is more likely to contain regions of cells which have been deprived of oxygen (hypoxic) [9]. These hypoxic cells are more resistant to lethal radiation damage than those with a normal oxygen supply [9]. This is because the free radicals which are produced from the incident radiation cause damage to the DNA. In the presence of oxygen, this DNA damage can become fixed and irreparable. Alternative mechanisms are able to repair the damage when less oxygen is present [9], and so results in an increased resistance to the radiation. The increased resistance means an increased dose is required to eradicate them. The increased dose, and the larger field sizes required for the treatment, results in an increased morbidity of the surrounding healthy tissue.

1.2.4 Volume Definitions

Specific regions are defined and used for treatment planning to ensure optimal coverage of a tumour and to minimise dose to healthy tissue. These volumes are defined in Table 1.1 and shown in Figure 1.3.

The definition of these volumes helps to ensure effective coverage of the tumour when planning a treatment. This planning requires an understanding of how the particle delivered during treatment interacts within the tissues of the patient. Treatment planning software is used by specialist planning staff, working with the radiation oncologists to optimise incoming beam shapes and directions to achieve a conformal dose while avoiding organs at risk.

Table 1.1: Volumes which are defined for the purpose of radiotherapy treatment planning. Their locations are shown in Figure 1.3.

Volume	Definition
Gross tumour volume (GTV)	The visible extent of the tumour growth.
Clinical target volume (CTV)	A volume which contains the GTV and additional microscopic diseased cells.
Planning target volume (PTV)	An expanded region which contains the CTV and additional allowances for positional and geometric uncertainties.
Treatment volume	The volume specified by the radiation oncologist which receives 100% of the dose required to achieve the aims of the treatment.
Organs at risk (OAR)	Volumes of normal tissue which are sensitive to radiation. The position of these tissues influences the treatment plan.

1.3 Photon Interactions with Matter

The exponential falloff of the beam intensity, which has an initial intensity, I_0 , can be expressed by the equation

$$I(z) = I_0 e^{-z\mu} \quad , \quad (1.2)$$

where $I(z)$ is the intensity of the photon beam at a distance z through a material with linear attenuation coefficient μ . The linear attenuation coefficient is expressed as

$$\mu = n_A \sigma_T \quad , \quad (1.3)$$

where n_A is the number of atoms per unit mass and σ_T is the total cross section, describing the interaction probability, of all interaction mechanisms. The dominant

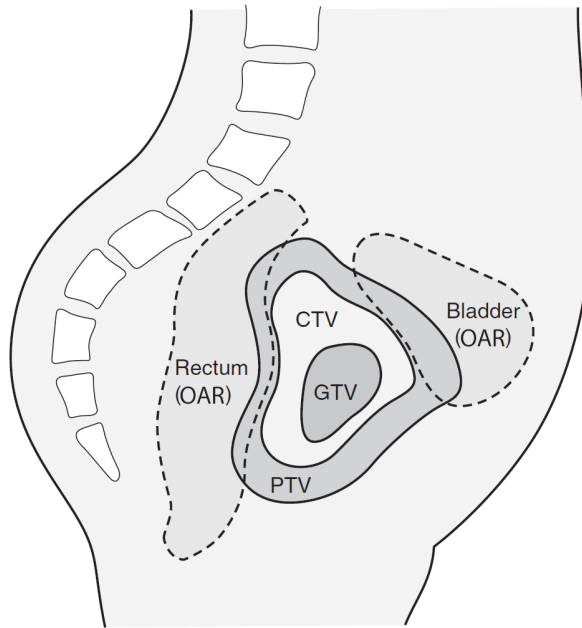


Figure 1.3: A diagram representing a prostate tumour treatment plan with GTV, CTV, PTV and OAR volumes [9].

interactions at treatment energies are Coherent Scattering, Photoelectric Effect, Compton Scattering and Pair Production [9]. The interaction dominance is discussed in more detail in Section 1.3.5.

1.3.1 Coherent Scattering

This interaction mechanism as shown in Figure 1.4 describes a low energy photon interacting with orbital electrons. The photon scatters at a small angle and retains its original energy through the interaction [14]. This mechanism therefore has little impact in radiotherapy treatment in terms of dose delivery.

1.3.2 Photoelectric Effect

The photoelectric effect can occur when an incoming photon has an energy larger than the binding energy of an electron. The photon interacts with the atom which

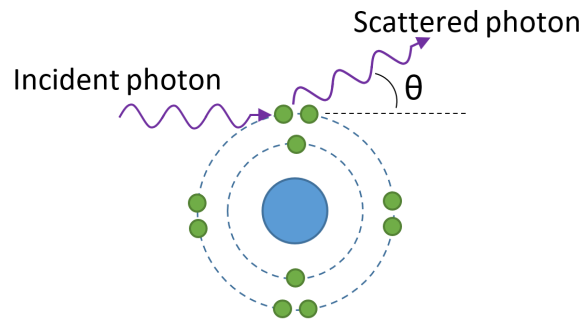


Figure 1.4: The coherent scattering process where an incident photon is scattered at a small angle with little to no energy change.

subsequently ejects an electron. The electron's kinetic energy is the difference between the energy of the interacting photon and binding energy. Once the electron is ejected, an electron from a higher shell transitions to the inner shell "hole". This transition is typically accompanied by the emission of a characteristic photon with an energy equal to the difference between the binding energies of the two shells. These photon energies are characteristic of the element. This process is shown in Figure 1.5.

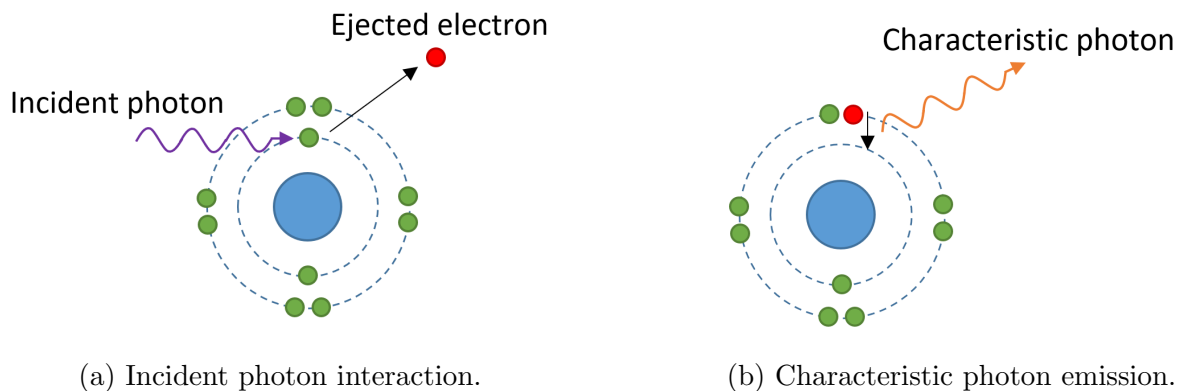


Figure 1.5: The photoelectric interaction of a photon with an atom. Nuclei are represented in blue and electrons in green.

The transition of an electron between shells may be accompanied by the emission of a second electron from the same atom instead of the emission of a characteristic photon. This process is called the Auger effect, and the emitted electron is called an Auger electron [15].

The photoelectric cross section, σ_f , describing the probability of a photon interacting through the photoelectric mechanism [14], follows the relation

$$\sigma_f \propto \frac{Z^n}{E^{3.5}} \quad , \quad (1.4)$$

where E is the energy of the photon and Z is the atomic number of the atom. The exponent, n , varies between 4 and 5 over the energy range of interest [14]. The probability of this interaction occurring therefore decreases rapidly for photons with higher energy.

1.3.3 Compton Scattering

Compton scattering is the most important interaction mechanism for photon radiotherapy. The photon energy must be much larger than the binding energy of the electrons for this mechanism to occur. The electrons then appear “free” to the photons. Energy is transferred as the photon scatters off an electron and results in both particles scattering in directions which conserve energy and momentum. This mechanism is shown in Figure 1.6.

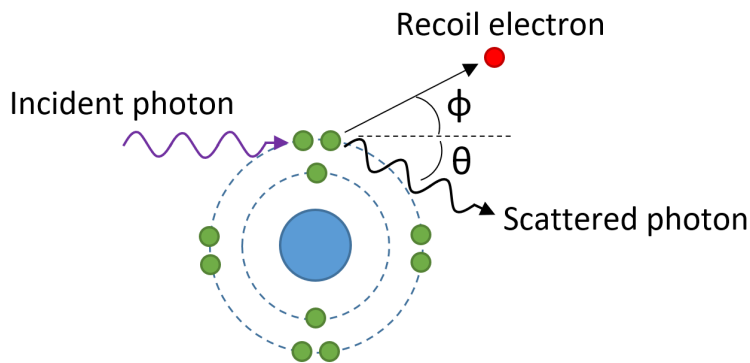


Figure 1.6: The Compton interaction of an incident photon with an electron.

The outgoing photon after interacting with an electron is scattered at an angle θ to the incident vector. The electron is similarly scattered at an angle ϕ to the same vector.

The energy transferred from the photon to the electron during this process results in an increase of the photon wavelength according to the equation

$$\Delta\lambda = \lambda' - \lambda = \frac{h}{m_e c}(1 - \cos \theta) \quad , \quad (1.5)$$

where λ and λ' are the incident and outgoing photon wavelengths respectively, m_e is the rest mass of the electron, h is Plank's constant and c is the speed of light.

The cross section for Compton scattering increases with the electron density of the material [14]. The electron density, which is proportional to Z/A , remains approximately constant for all elements (excluding Hydrogen). This constant relationship means that the cross section for Compton scattering only depends on the physical density of the material, and not the atomic number [9].

The conservation of momentum means that the electrons from a treatment beam predominantly scatter in the direction of the incident beam. These electrons then deposit dose over their relatively short range from where they are first produced. This results in a dose build up region as the beam enters the patient. This is discussed in more detail in Section 1.3.6.

1.3.4 Pair Production

Pair production is the process of a photon passing in the vicinity of a nucleus and producing an electron and a positron. The presence of the nucleus in this interaction is important to conserve momentum. The total combined kinetic energy of the electron and positron is the difference between the energy of the incident photon and twice the mass of the electron. The threshold above which this process can occur is therefore 1.022MeV - twice that of the electron rest mass. This interaction is shown in Figure 1.7.

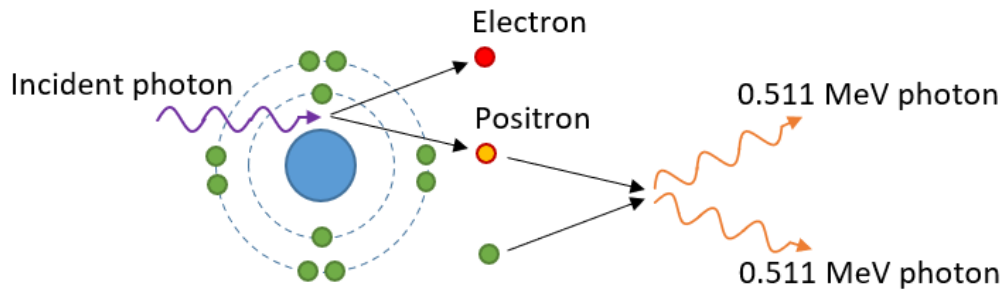


Figure 1.7: The process of pair production where an incident photon interacts with a nucleus to create an electron and a positron.

The generated electron and positron deposit their kinetic energy as they undergo further interactions within the medium. This can include the liberation of further electrons if of a sufficiently high energy. The positron quickly annihilates with an electron and releases two photons of 0.511MeV. These newly produced photons then typically deposit their energy through the dominant Compton and photoelectric interactions at this lower energy.

1.3.5 Interaction Mechanism Dominance

The contribution to dose from each mechanism varies as a function of the photon energy. The dominance of each interaction mechanism therefore differs depending on whether the photons are at imaging or treatment energy. Figure 1.8 shows the regions of dominance for each mechanism as a function of photon energy and atomic number of the material.

Figure 1.9 shows the relative distribution of photons as a function of energy, for a 100kV beam used for imaging, and a 6MV beam used for treatment. These photon beams are produced by accelerating electrons using an electric potential onto a target material, such as tungsten in the case of Figure 1.9 [9]. The interaction of these electrons with the target produces bremsstrahlung radiation and the resulting continuum in the Figures. The sharp peaks in Figure 1.9a are the photons which are released as electrons transition

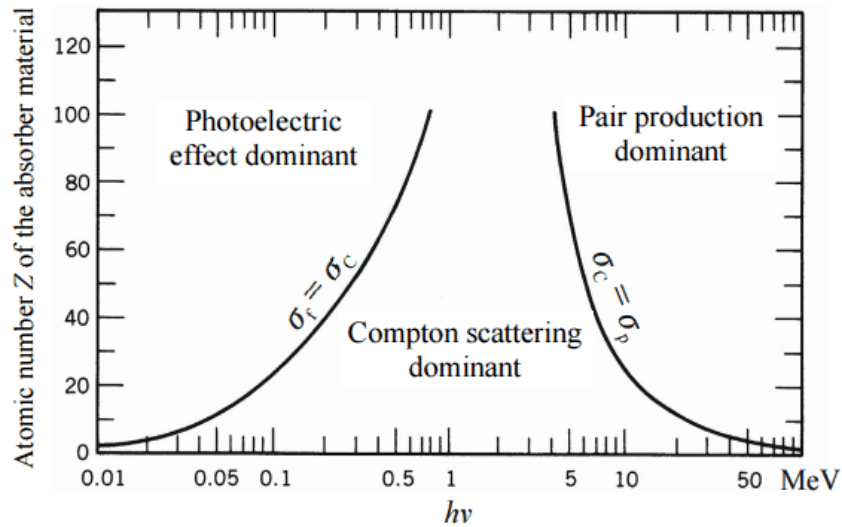


Figure 1.8: The dominant photon interaction mechanisms for differing energy and atomic number of the material traversed [16]. σ_f , σ_C and σ_p are the photoelectric effect, Compton and pair production cross sections which represent the probability of each interaction occurring.

between shells of ionised atoms in the target. These peaks are therefore characteristic of the target material as each material has distinct energy levels. They are not clear in Figure 1.9b because of the increased dominance of photons at higher energies.

The high proportion of low energy photons in the 100kV beam, compared with the 6MV beam, means that the photoelectric interaction will be more dominant during imaging in comparison to treatment. Compton scattering then becomes more dominant at treatment energies.

1.3.6 Photon Dose Distribution

The photon dose distribution as a function of depth in a patient is shown in Figure 1.10. This distribution shows that the tissue both in front and behind the target volume receives a dose of radiation due to its exponential decrease in intensity. It is detrimental for the patient to have these regions receiving dose as additional damage to healthy tissue is caused. It is one of the main disadvantages to photon radiotherapy but advanced

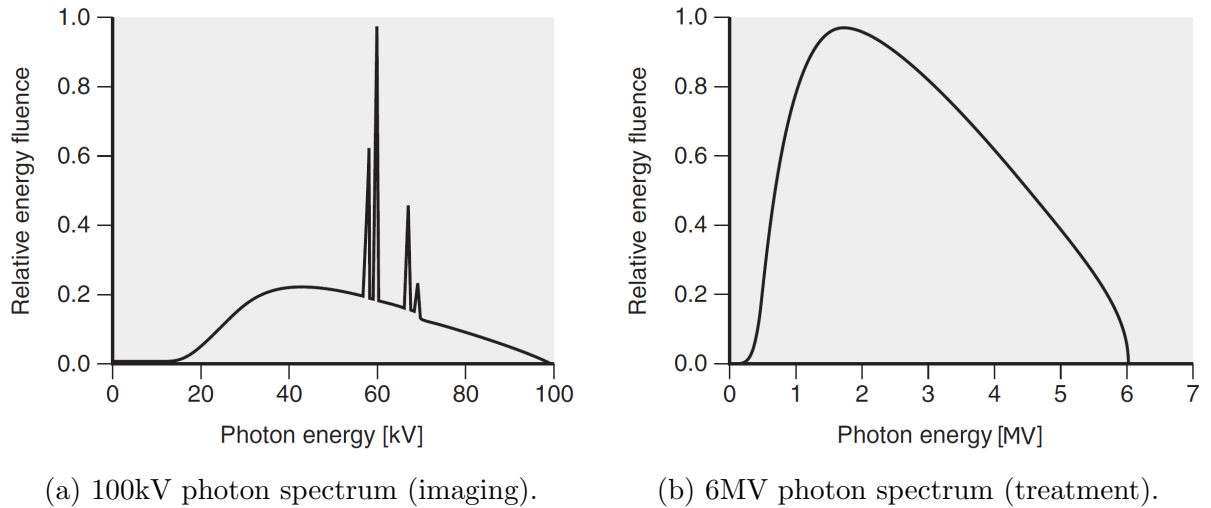


Figure 1.9: The energy spectra of photons for a 100kV beam used for imaging, and a 6MV beam used for treatment [9].

techniques have been developed to mitigate this problem as much as possible. These techniques are discussed in more detail in Section 1.4.

The region between zero depth and the maximum point of the curve is referred to as the dose buildup region. This region is present as secondary electrons are generated due to the Compton interaction. These secondary electrons deposit energy along their path into the material causing the dose to increase. At the point of maximum dose, the number of secondary electrons depositing dose to the medium saturates. This is typically at a depth of approximately 1cm for a 3MeV photon (average photon energy in a 10MV photon beam) [9]. The dose deposited within the medium is then dominated by the number of photons, and consequently decreases with the intensity as they are attenuated, in accordance with Equation 1.2. The comparably small dose at the surface of the material is referred to as the skin sparing effect [9]. This effect is beneficial for a patient as it reduces the level of side effects on the skin surface from a treatment [17].

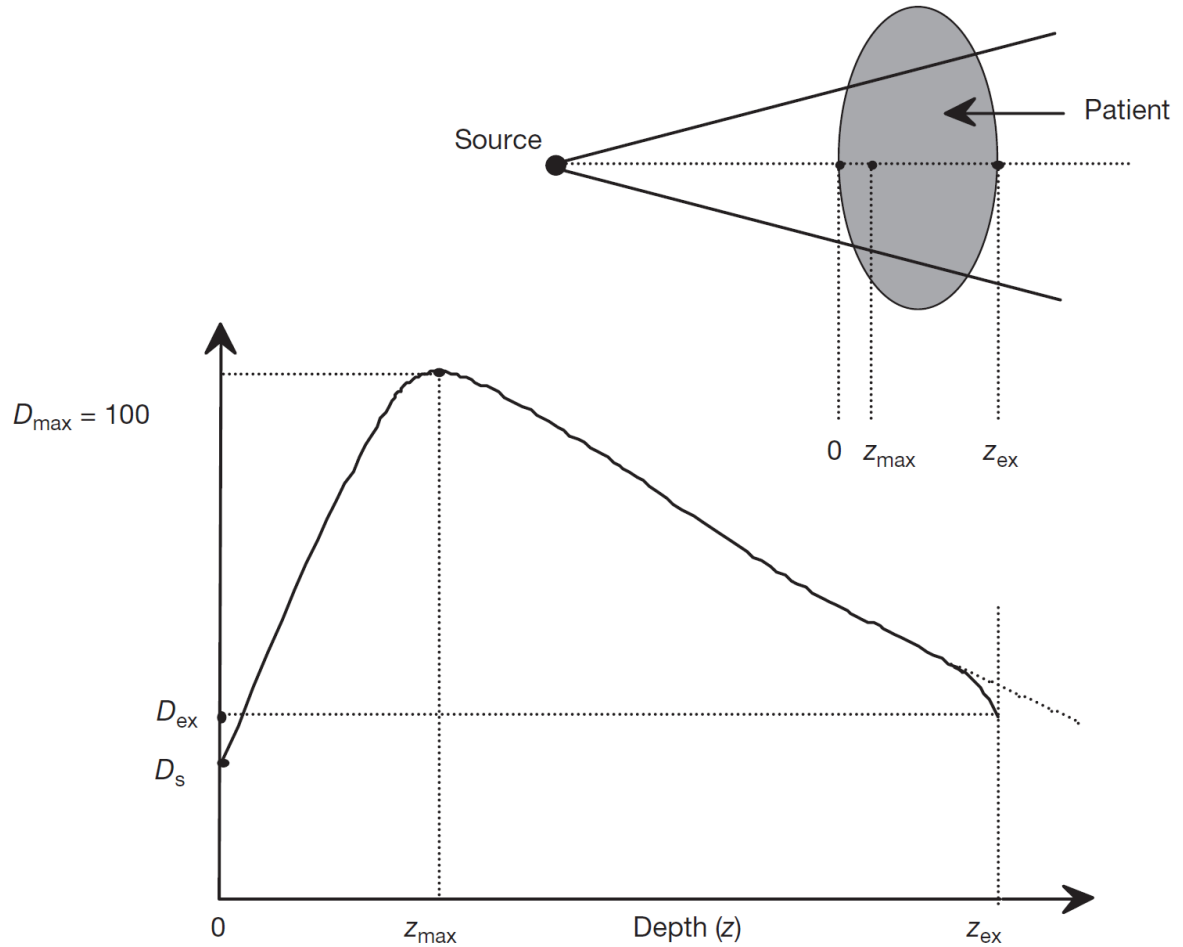


Figure 1.10: The relationship between the dose of a photon beam and the depth through a patient. The region from 0 to z_{max} shows the dose buildup region and ends at the point of maximum dose, D_{max} (normalised to 100). D_s and D_{ex} are the entry and exit doses to the patient respectively [13].

1.4 Photon Therapy Techniques

1.4.1 3DCRT

The photon interactions giving an exponential fall off in dose as a function of depth results in an inevitable dose being delivered to healthy areas of the body. 3D Conformal Photon Radiotherapy (3DCRT) is the technique of delivering beams of photons from multiple angles which conform to the planning target volume [9]. A map of the dose delivered to a patient for a given treatment region using uniform beams at fixed angles is shown in Figure 1.11a. The treatment volume which requires a sufficient dose is shown

by the white line. For this treatment there are two incident beam directions; one entering the patient from the bottom of the image and the second from the right of the image. It can be seen that there is excess dose in the regions before and after the tumour as highlighted in green. The buildup region can also be seen within these green regions. This is particularly disadvantageous in this treatment case as this higher dose is delivered close to the spinal cord for the beam entering from the bottom of the image. The spinal cord being a critical structure (OAR) means that dose to it should be minimised [18].

The region receiving a higher dose can be seen as the red square where the two beams intersect. The treatment volume which requires the treatment dose being approximately circular means that the tissue in the corners of the red square receives a significant and unrequired dose. Receiving such a high and unnecessary dose could be severely detrimental to the patient.

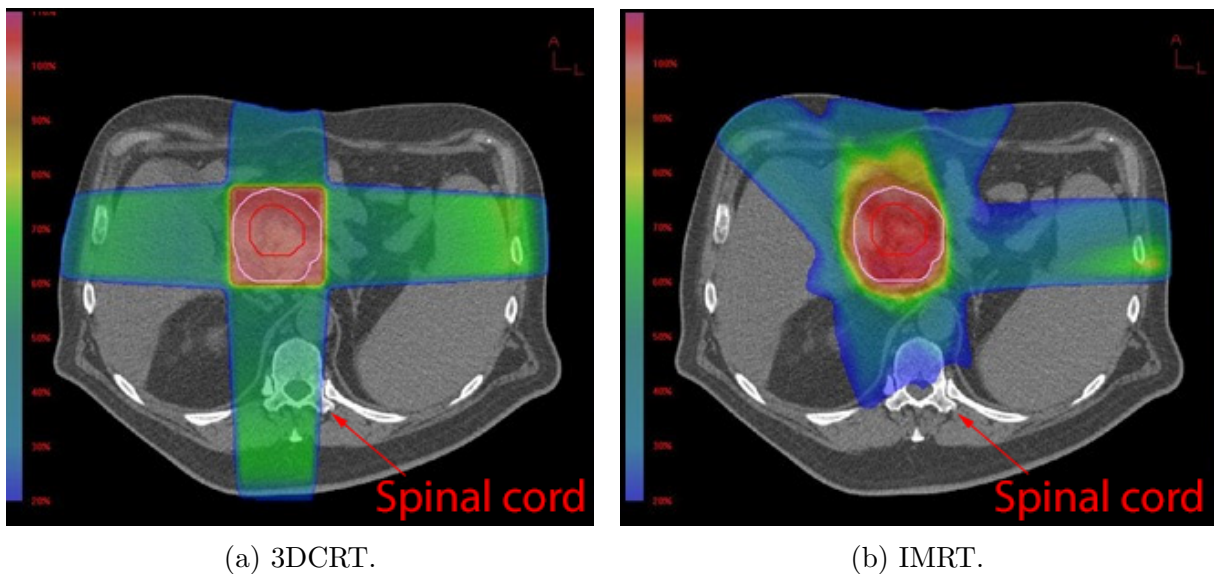


Figure 1.11: Dose maps of 3DCRT and IMRT treatment plans for a given tumour volume [19].

1.4.2 IMRT

Intensity Modulated Radiotherapy (IMRT) is the use of non-uniform photon beams from multiple angles to give a uniform dose to the tumour volume. The use of non-uniform beams allows the high dose region to conform more to the tumour volume. Dose to the surrounding healthy tissue is therefore reduced to minimise the NTCP. Non-uniform beams also allow for critical structures to be better avoided or only being partially irradiated [20].

Figure 1.11b shows the dose distribution from an IMRT treatment for the same tumour volume in Figure 1.11a. The high dose region highlighted in red is more conformal to the tumour volume. This means the tissue in the corners of the high dose square region for the plan with uniform beams receives a reduced dose. The volume of healthy tissue being irradiated using IMRT may increase compared with a uniform beam treatment from fixed angles. However, the reduction in the dose delivered per unit volume can help to reduce the NTCP.

1.4.3 IGRT

Image Guided Radiotherapy (IGRT) is another technique used to improve photon therapy treatments. IGRT is the process of taking a 3D image of the patient just before delivering a treatment fraction. The position of the patient as well as the tumour and critical structure positions can therefore be determined. Appropriate positional corrections may then be made before delivering the fraction. This technique ensures that the high dose region is being delivered in the correct location. It is otherwise possible that a tumour may not be fully irradiated and killed as it may receive too little dose. The high dose intended for the tumour would also be delivered to otherwise healthy tissue and could cause further complications.

The method of delivering the total dose in fractions over a period of days is well established practice. This prolonged period leads to the potential of anatomical changes within the patient such as losing or gaining weight. The process of using image guidance therefore helps to identify if a re-plan of the treatment would be advantageous to ensure effective targeting of the tumour.

1.4.4 VMAT

Volumetric Modulated Arc Therapy (VMAT) is another advanced technique of delivering an external beam of photons. In this case, photons are delivered continually as the beam nozzle moves around the patient. This differs from the previously described IMRT delivery technique which used fixed angles. The shape and intensity of the beam is continually varied which achieves an even more conformal dose to the tumour volume. Again, this method increases the volume of healthy tissue being irradiated, but reduces the dose per unit volume and NTCP. The time taken to deliver a treatment fraction is also reduced which reduces the likelihood of the patient moving during the treatment. The number of patients able to be treated in a given amount of time is also increased which is advantageous to both patients and hospitals.

1.5 Proton Therapy

Proton therapy is becoming a more widely used form of radiotherapy for the treatment of cancer. As of June 2020, 92 proton therapy facilities were in operation across the world [21] and a further 34 under construction [22]. The UK has been delivering proton therapy at The Clatterbridge Cancer Centre since 1989 to treat rare cancers of the eye [23]. Until recently, patients in the UK deemed to require proton therapy to optimise their outcome for any other cancer were sent abroad in order to be treated. The UK

National Health Service (NHS) has now committed to the construction of two new proton therapy facilities meaning that these patients may be treated without leaving the UK. The Christie Proton Therapy Centre in Manchester [24] has started treating patients and University College London Hospital (UCLH) Proton Therapy Centre [25] is undergoing commissioning. These clinical facilities deliver protons at energies up to approximately 245MeV, which can traverse a depth of approximately 38.5cm in water [26].

Protons offer various advantages when compared with photons for treating cancer providing the treatment is delivered correctly. These advantages are due to the difference in the way the protons interact with the tissues in the patient. The proton interaction mechanisms and how they lead to a potential improvement in radiotherapy treatment are outlined in the following sections.

1.5.1 Proton Interaction with Matter

Protons predominantly interact as they traverse a material through Coulomb interactions with charged particles. This interaction causes ionisation and excitation of atoms. Figure 1.12 shows the important interactions of protons with matter when considering proton therapy.

1.5.1.1 Inelastic Coulomb Interaction

Figure 1.12a shows an inelastic Coulomb interaction of a proton with an atom. The proton interacts with an electron in a shell giving it enough energy to be ejected from the atom. This results in an ionised atom, a free electron, and the incident proton with less energy than it had before the interaction. It is through this interaction that the incident protons primarily deposit their energy in the material. This interaction is also the cause of the variation in range of the protons through the material, called range straggling [28].

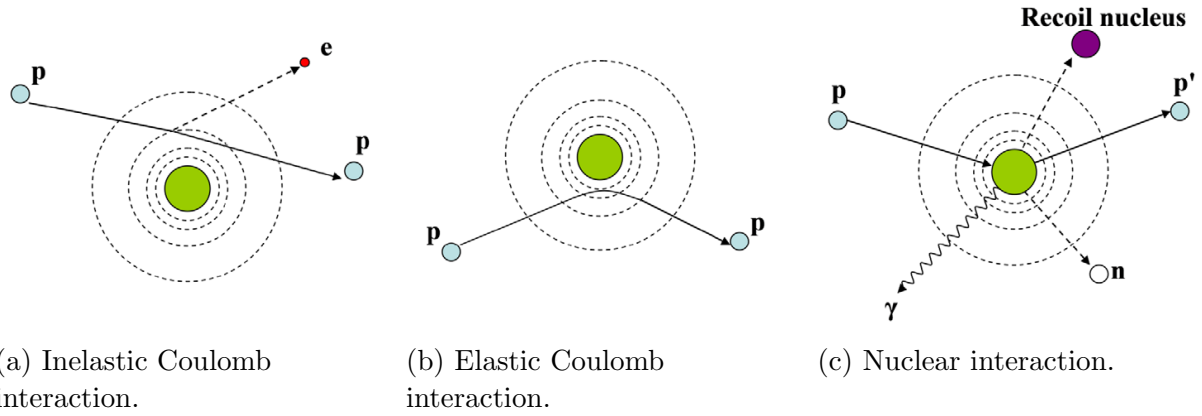


Figure 1.12: The dominant interaction mechanisms of protons with matter in proton therapy [27].

1.5.1.2 Elastic Coulomb Interaction

Figure 1.12b shows an elastic Coulomb interaction of a proton with an atom. The proton interacts with the nucleus of the atom and can be deflected by a large angle. The nucleus recoils, absorbing some of the proton energy in order to conserve momentum. The atom is left in an excited state. It is predominantly through this interaction that the lateral scatter of the protons originates, as the direction of incident protons is significantly affected. These interactions are less frequent than the inelastic Coulomb interactions because of the small size of the nucleus in comparison to the electron cloud [29], but have a more significant effect on the direction of the protons [27].

1.5.1.3 Nuclear Interaction

Figure 1.12c shows the infrequent nuclear interaction which occurs, but has an important effect on a proton treatment. The proton is absorbed by the nucleus of the atom, which subsequently decays; releasing protons, neutrons, or heavier ions. The nucleus recoils conserving momentum. Though infrequent, this interaction affects the primary fluence of the beam. This fluence is the number of protons passing through a given area per second.

A proton treatment is planned in order to give a specific dose to the tumour to destroy it. This required dose may not be met if too many protons are absorbed and removed from the beam through nuclear interactions. This effect must therefore be taken into account when planning a treatment to ensure the required dose reaches the tumour [28].

1.5.2 Stopping Power

It is critical to know how protons are expected to deposit their energy as they traverse a patient when planning a proton therapy treatment. The quantity required for this is the stopping power, S_p . This is the energy loss of a particle per unit length and can be represented by the equation

$$S_p = \frac{dE}{dz} \quad , \quad (1.6)$$

where dE is the energy loss of an incident beam over a distance dz . Stopping power can also be represented empirically by the Bethe-Bloch formula [30] as

$$-\frac{dE}{dz} = Kq^2 \frac{Z}{A} \frac{1}{\beta^2} \left[\frac{1}{2} \ln \frac{2m_e c^2 \beta^2 \gamma^2 W_{max}}{I^2} - \beta^2 - \frac{\delta(\beta\gamma)}{2} \right] \quad , \quad (1.7)$$

where K is a constant given by $4\pi N_A r_e^2 m_e c^2$. N_A is Avogadro's number, r_e is the classical radius of the electron, m_e is the mass of the electron, c is the speed of light, q is the charge number of the incident particle, Z is the atomic number of the absorbing material, A is the atomic mass of the absorber, β and γ have their usual meanings in relativistic kinematics, W_{max} is the maximum energy transfer in a single collision, I is the mean excitation energy of the material and $\delta(\beta\gamma)$ is a density correction originating from ionization energy loss.

The strong Z/A dependence, and the dependence on I , highlights the importance of knowing the properties of the material being traversed by the protons in order to plan an effective treatment.

1.5.3 Proton Dose Distribution - The Bragg Peak

The energy loss of a proton as described by Equation 1.7 gives rise to the characteristic shape of the proton dose distribution. This distribution is significantly different to that shown in Figure 1.10 and is the reason for the various advantages that proton therapy offers. The dose distribution as a function of depth due to the proton interaction mechanisms described in Section 1.5.1 is shown in Figure 1.13.

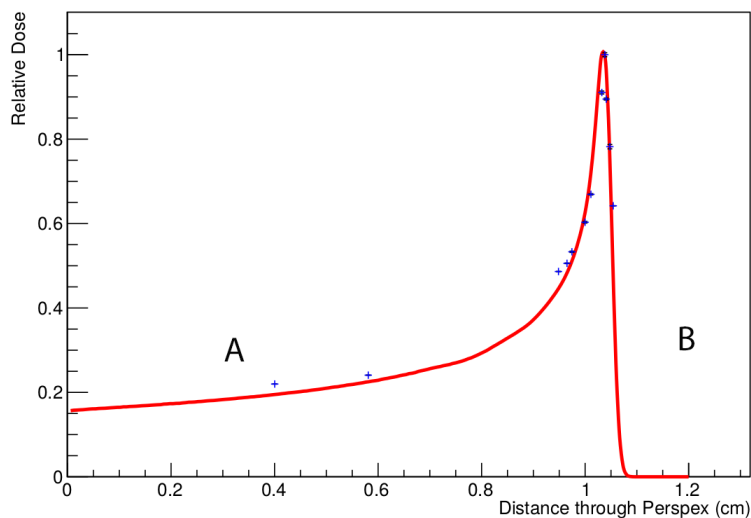


Figure 1.13: Relative dose as a function of depth for a 36MeV proton beam through Perspex. The red curve is the dose determined from Geant4 simulation. The blue points are measurements made on the Birmingham beamline.

Region A on the curve shows a low relative dose compared with photons. The dose remains approximately constant along the protons path until it approaches the end of its range. Interactions become more frequent as the proton slows which causes a fast increase in dose and the characteristic Bragg peak as they stop. This well defined range

gives rise to Region B where there is no dose delivered beyond the peak of the dose distribution [27]. This is unlike photons which continue to deliver dose beyond the peak of their dose distribution as shown in Figure 1.10.

The dose distribution in Figure 1.13 has been produced using simulation in the Geant4 software [31]. The result of a 36MeV proton beam incident on Perspex in simulation is shown by the red curve. Experimental data was collected on the University of Birmingham MC40 cyclotron to determine the beam energy (nominally 36MeV) by mapping the Bragg peak. This data was collected by measuring the dose to a Markus chamber [32] after the beam had passed through various thicknesses of Perspex. This experimental data, shown by the blue points on Figure 1.13, was therefore used to validate the result from simulation.

1.5.4 Proton Range

The mean range of protons through a material is defined as the depth at which the incident fluence of protons reduces by half [27]. This range within a material is not a single value for all protons due to the statistical fluctuations involved in their interactions. Protons deposit energy with statistical fluctuations which broadens the distribution of proton energies within the beam. This broadening is called energy straggling. The variation of proton energy therefore causes variations in the proton range around a mean value. This is called range straggling. It is this statistical nature that causes the broadening of the Bragg peak. The range straggling, which is defined as the standard deviation of a Gaussian fit to the range distribution, is approximately 1.1% of the proton range [33]. This is equivalent to 2.85mm for a 200MeV proton beam in water [33].

Figure 1.14 demonstrates how the fluence changes as a function of depth through water. Fluence is initially most strongly influenced by nuclear interactions within the medium.

The dominating effect of the reduction in fluence is absorption within the medium once the protons have deposited most of their energy.

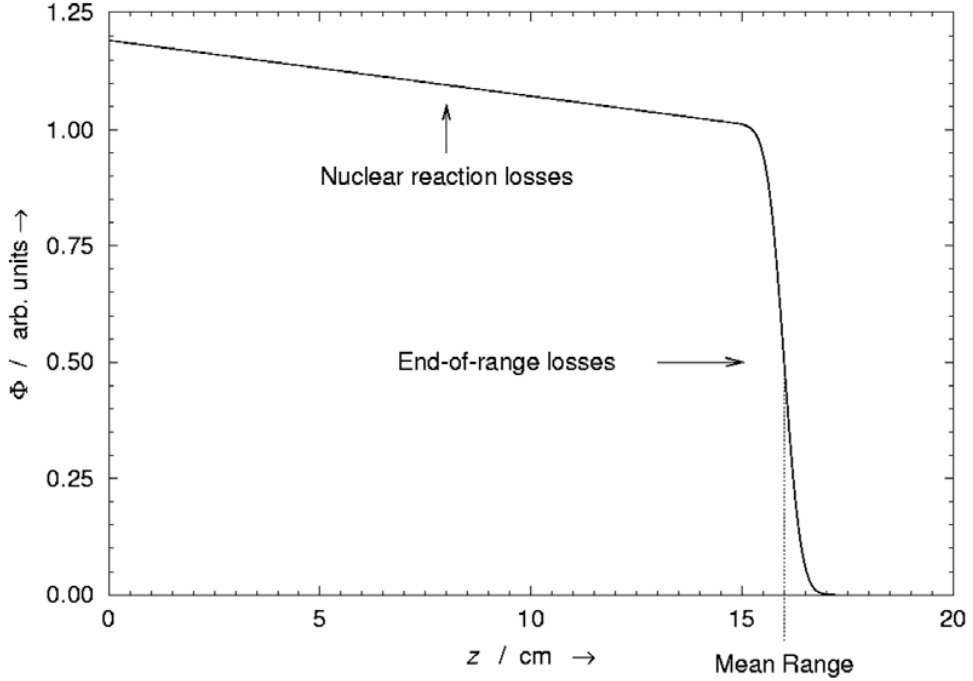


Figure 1.14: The fluence of a proton beam through water which has been normalised to the fluence near the end of range [27]. Fluence is initially affected most strongly by nuclear interactions. Absorption of protons within the medium dominates once the protons have deposited most of their energy.

The range $R(E)$ of protons through a medium can be described in relation to the stopping power according to the equation

$$R(E) = \int_0^E \left(\frac{dE'}{dz} \right)^{-1} dE' , \quad (1.8)$$

where E is the proton beam energy. This integral is of the Bethe-Bloch formula and is not trivial to solve. One approximation is to use the 1st term of the Taylor series, and is referred to as the Bragg-Kleeman rule [34]. The Bragg-Kleeman rule can also be used to

describe the range of protons within a medium and is given by the expression

$$R(E) = \alpha E^p \quad , \quad (1.9)$$

where α and p are parameters which can be derived experimentally and relate to the material and particle properties [35].

1.5.5 Linear Energy Transfer

Linear Energy Transfer (LET) describes the density of energy deposition from an ionising particle and is defined in units of $\text{keV}\mu\text{m}^{-1}$. The effect of a higher LET is that more damage is caused over a given distance of particle travel. Lower LET radiation is therefore less likely to cause a double strand break in the DNA of a cell than one with higher LET [9].

The use of fractionation in radiotherapy treatments is motivated by the ability of healthy cells to repair single strand breaks to DNA. Double strand breaks to the DNA cannot be repaired and lead to cell death. Protons at the end of their range have a higher LET than photons due to their higher ionising potential. This means there are a greater number of interactions within a cell and therefore has a higher probability of causing a double strand break which leads to cell death. It is therefore possible to achieve the same amount of biological damage to a tumour with a reduced dose compared with photons. A representation of the concept of LET is shown in Figure 1.15.

1.5.6 The Advantage of Proton Therapy

The well defined range as well as the large ratio between the dose at the Bragg peak and Region A in Figure 1.13 means that effective targeting of the protons can achieve

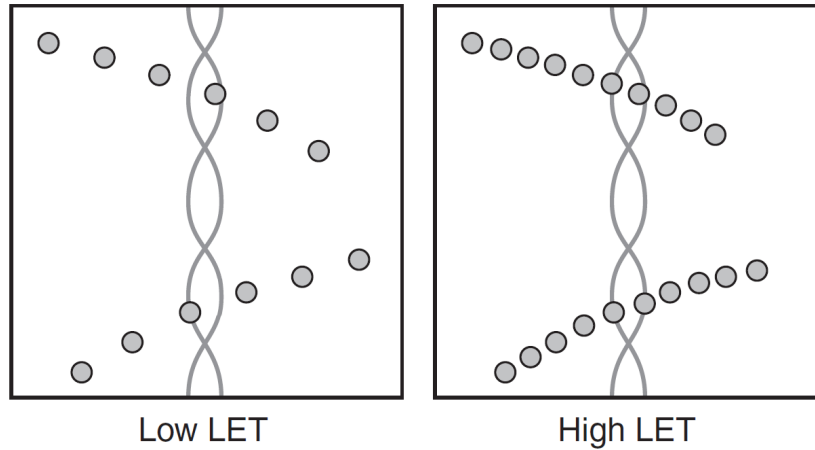


Figure 1.15: A comparison of Linear Energy Transfer (LET) between low LET (photons) and high LET (protons at the end of their range) particles [9].

significantly reduced dose to healthy tissue. The Bragg peak, if targeted directly inside a tumour, delivers high dose relative to the dose delivered along the entry path of the proton. The proton then having stopped within the tumour means that no dose is delivered to the tissue behind the planning target volume. This is demonstrated in the proton dose map in Figure 1.16 for the same treatment region previously described for photons in Figure 1.11b.

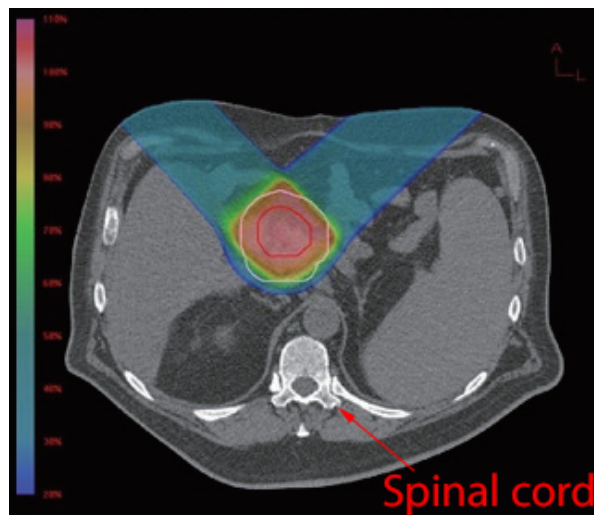


Figure 1.16: Dose map of the same region shown in Figure 1.11b with a proton treatment [19].

It can be seen that there are two beams entering the patient from the top of the image.

These beams show low and approximately constant dose as the protons enter the patient. There is high dose where the beams cross and protons stop inside the tumour volume. Below the treatment region there is no dose. This leads to a complete sparing of the spinal cord, and a much reduced overall total energy deposition within the patient, which is advantageous.

The reduction of dose delivered to healthy tissue means cancers in the head and neck as well as cancers in paediatric patients have the largest benefit from proton treatments. Critical structures in the head and neck may be better avoided by taking advantage of the finite range of protons. The lower dose build up region of protons compared with photons may alternatively be taken advantage of if critical structures cannot be totally avoided. The main benefit for paediatric patients is the general reduction in dose delivered to healthy tissue. This is because these patients have increased cell turnover due to their growth and development, and more years of life in which the long-term effects of treatment will become apparent, so any damage to the DNA has an increased potential to cause problems [36].

The increased value of the LET for protons at the end of their range makes them more effective at causing double strand breaks in DNA. This increased density of damage results in an increased effectiveness of a given dose of radiation when compared with photons. This increased effectiveness, referred to as Relative Biological Effectiveness (RBE), means that it may be possible to reduce the dose required to obtain the same TCP. The reduced dose to healthy tissue reduces the NTCP and consequently causes an improvement of the therapeutic ratio.

1.5.7 Heavy Ion Therapy

Heavier ions such as helium and carbon are also used for radiotherapy treatments and offer some advantages over proton therapy. One of these advantages is that the Relative Biological Effectiveness (RBE) is greater for carbon ions than it is for protons [37]. The relative dose distribution as a function of depth of a 3480MeV carbon beam through water is shown in Figure 1.17.

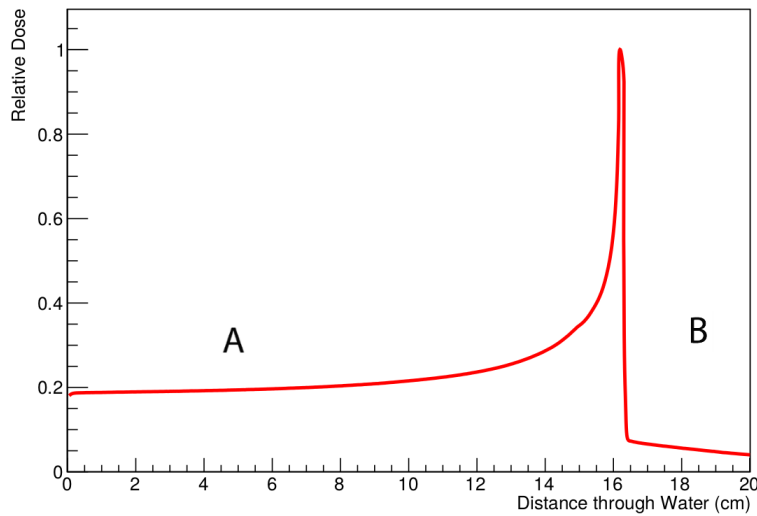


Figure 1.17: Relative dose as a function of depth for a 3480MeV carbon ion beam through water. The dose has been determined using Geant4 simulation and compared with similar results in literature [38].

The depth dose curve shows a similar distribution to protons with the presence of a Bragg peak as described by the Bethe-Bloch formula (Equation 1.7). There is a low dose region compared with the maximum dose as the carbon ions enter the patient labelled as Region A in Figure 1.17. This allows dose to healthy tissue to be minimised. The Bragg peak is also sharper than that of protons and has a faster declining falloff from the point of maximum dose. This allows the potential for more conformed dose distributions to be achieved at the tumour site. The additional mass of the carbon ions means that multiple scattering of the ions has less of an impact on the ions' trajectory. A carbon beam therefore maintains its profile for an

increased distance through the patient which results in more conformal dose distributions.

A treatment using carbon ions also benefits from the higher LET at the end of range. This LET, which has been shown to be larger than that for protons [39], potentially offers the opportunity for a further reduction in dose required for tumour control. However, a disadvantage of using carbon ions for radiotherapy treatment is that they fragment as they undergo nuclear interactions and give rise to the low dose tail labelled as Region B in Figure 1.17. These fragments continue to deposit dose as they travel through the patient beyond the Bragg peak. This makes it more difficult to avoid depositing any dose to critical structures unlike protons which have a distinct end of range.

Another problem with carbon therapy is that it is still relatively new to the field of cancer treatment. An understanding of the carbon-ion RBE has not yet been concluded which introduces additional uncertainties when planning and delivering treatments [40] [37]. Not having a standard RBE model for planning treatments introduces difficulty when comparing clinical statistics between facilities [40]. These uncertainties, along with the small number of clinical trials and difficulty in comparing them, means carbon ions are far from being used routinely for treatment.

Chapter 2

Particle Detection

It is important to consider how particles interact and deposit energy to devise an efficient method for their detection. The Bethe-Bloch formula (Equation 1.7) describes the mean energy loss rate as a charged particle traverses a medium. Integration of this formula for a material thickness, x , then describes the energy lost [41]. The additional consideration of the statistical nature of particle interaction results in a Landau distribution describing the energy loss probability [42] as shown in Figure 2.1.

The interaction mechanisms of protons which contribute to their energy loss have been outlined in Section 1.5.1. The dominant of these mechanisms is the Coulomb interaction process which results in ionisation of atoms. This ionisation can be taken advantage of for the purpose of particle detection. The properties of semiconductors make them an ideal material for this purpose as the energy to liberate an electron within the crystal is low. This is described in more detail in the following sections. Silicon is one such popularly used semiconductor and has been utilised for over 40 years in nuclear, particle and astrophysics detectors [43].

Silicon devices have been chosen for the detection and tracking of charged particles closest to the interaction point for all experiments at the Large Hadron Collider (LHC) at

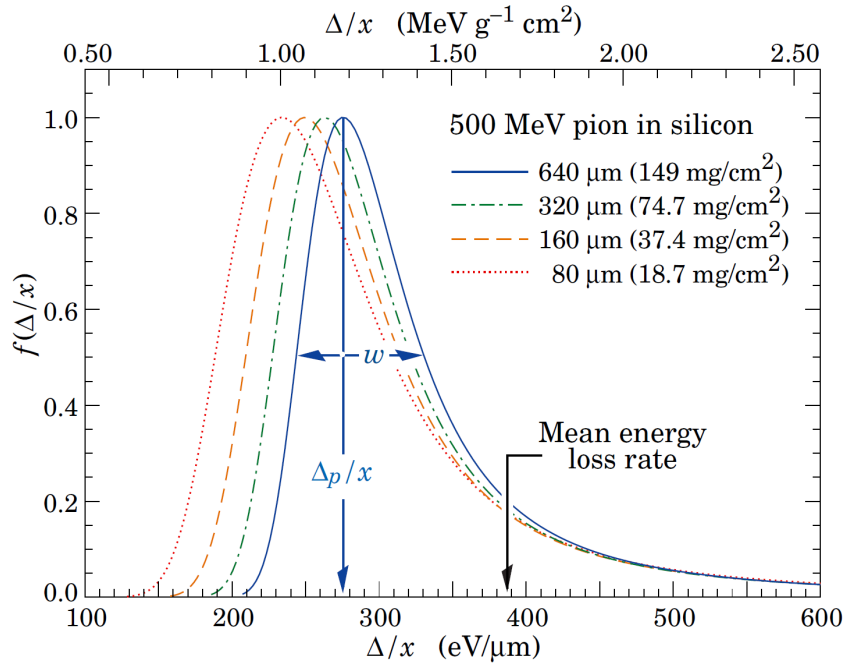


Figure 2.1: The normalised probability distribution describing energy loss, Δ , per micron of 500MeV pions in silicon. The most probable value is $\frac{\Delta_p}{x}$ and w is the full width at half maximum [42].

CERN. They continue to be of key importance as demonstrated by their selection for use in the High Luminosity LHC (HL-LHC) upgrade of the ATLAS detector [44] [45]. The high density of particles and large doses in this close proximity to the interaction point requires fine granularity and high radiation tolerance of the devices. These properties are similarly required for the application of such devices in the field of proton therapy. Clinical practicability requires devices to be sufficiently radiation hard to survive years of use on a clinical system. Fast readout and fine granularity are also required due to the high rate and density of protons in a clinical beam. It is for this reason that silicon devices have been examined for the purpose of these studies.

2.1 Semiconductors

2.1.1 Energy Band Theory

Only two electrons with opposite spin may occupy a single energy level of an atom in accordance with the Pauli exclusion principle [46]. For example, an atom of lithium contains three electrons, and has a shell configuration of $1s^2 2s^1$. The $1s$ level is occupied by two electrons with opposing spin, and the $2s$ level has a single electron. This shell configuration is the same for all isolated lithium atoms. Figure 2.2 shows a schematic representation of the energy levels and potential well around a single lithium atom.

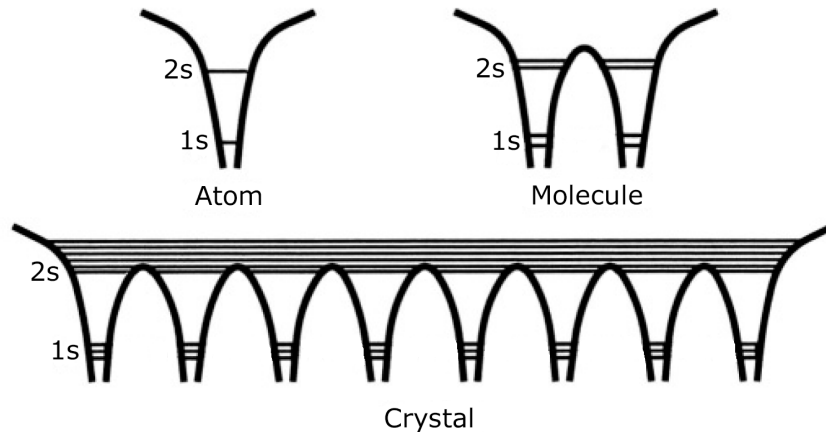


Figure 2.2: A schematic diagram of the energy levels in an atom, hypothetical molecule, and a crystal structure for lithium [46].

Extending this to the theoretical case of a molecule of lithium, and the case of a crystal containing N atoms, means a solution is required to maintain each electron in a different energy state. These configurations are also shown schematically in Figure 2.2. This is solved by further segmenting each energy level within a crystal of N atoms into N sub-levels with discrete energies [46]. The difference in energy between sub-levels is immeasurably small in comparison to the few eV difference between levels [46]. These energy sub-levels are sufficiently close that they can be considered as no longer discrete; instead forming a continuous band of permitted energy levels throughout the crystal.

The potential wells which are formed by the nuclei restrict the most tightly bound electrons so that they remain in the immediate vicinity of the nuclei. However, Figure 2.2 illustrates that the close packing of atoms results in a reduction of the potential barrier between them. The number of electrons in the outermost occupied energy level of an atom defines the valence, and these electrons often form covalent bonds [46]. Depending on the band structure in a given solid, it is also these electrons that can have enough energy to overcome the potential barrier between atoms and move freely throughout the crystal [14].

2.1.2 Conductors, Semiconductors and Insulators

The properties of conductors, semiconductors and insulators can be defined by the relation of their energy bands to the Fermi level. The Fermi level is defined as the maximum energy an electron may have in a material at a temperature of 0K [46]. In the case of a conductor, the highest occupied energy band is not filled at 0K, and the Fermi level is inside this band. This means that electrons only need an almost infinitesimal energy to change state within the band to move freely throughout the material. These materials therefore have good conductivity at room temperature.

The Fermi level, in the case of semiconductors and insulators, exists between the valence and conduction bands. Their valence band at 0K is filled, and the energy band above it (conduction band) is empty. This means that there is a minimum energy required for an electron to change state and move freely throughout the material. This energy is equal to the energy difference between the top of the valence band and the bottom of the conduction band, called the band gap [46]. For an insulator such as SiO_2 , the band gap is of the order of 9eV [47], which results in poor conductivity at room temperature. A semiconductor has a smaller band gap, typically less than 2eV [46], which means that thermal energy and excitation from visible light at room temperature can cause electrons

to transition from the valence band into the conduction band [46]. A vacancy, referred to as a “hole”, is left behind in the valence band if an electron moves from the valence band to the conduction band. These holes act like positive charge carriers. The separation of these bands for conductors, semiconductors and insulators is shown schematically in Figure 2.3.

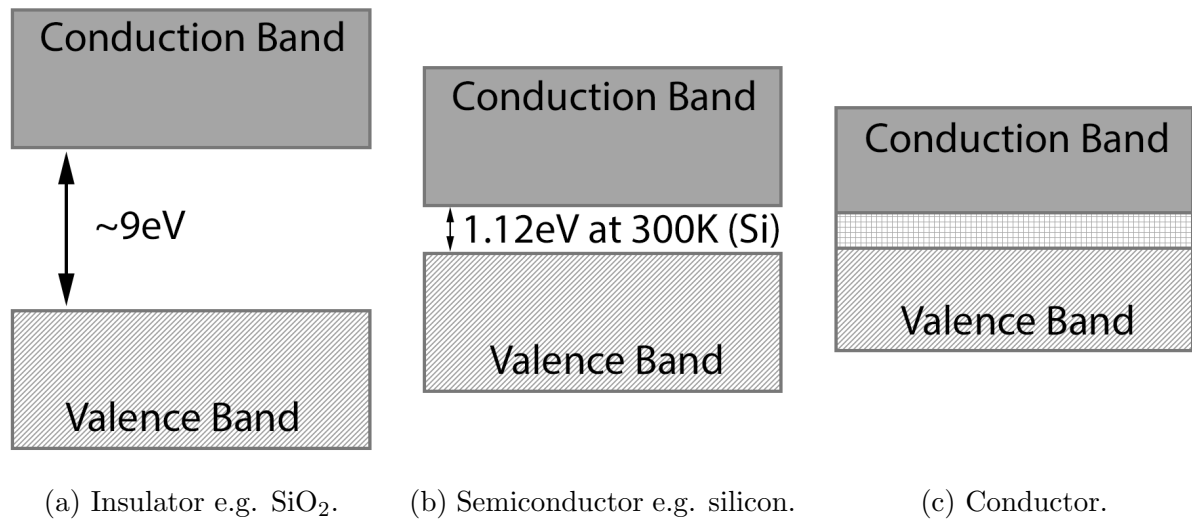


Figure 2.3: A simplified representation of the band gap separation between the valence and conduction bands for an insulator, semiconductor and conductor.

The band gap is 1.12eV for silicon at 300K [48]. For a traversing charged particle, on average 3.62eV is lost for every electron-hole pair produced within the silicon. The difference between this and the band gap is the amount of energy which is absorbed by the material through various mechanisms such as causing vibrations in the lattice structure [46]. It is this small energy required to create an electron-hole pair that makes silicon an ideal material for charged particle detection.

2.1.3 Doping

The silicon atom, with an atomic number of 14, contains 2, 8, and 4 electrons in its 1st, 2nd and 3rd shells respectively. Silicon atoms together form a crystal structure where each electron in the outermost shell contributes to a covalent bond to a neighbouring

silicon atom. This results in all silicon atoms in the bulk of the material containing a full outer shell of electrons. A crystal containing pure silicon (intrinsic) at low temperature therefore has very poor conductivity as there are no free electrons. The resulting structure is a diamond lattice with each silicon atom having 4 covalent bonds to its neighbours. A schematic representation of the arrangement of electrons in this crystal structure is illustrated in Figure 2.4a.

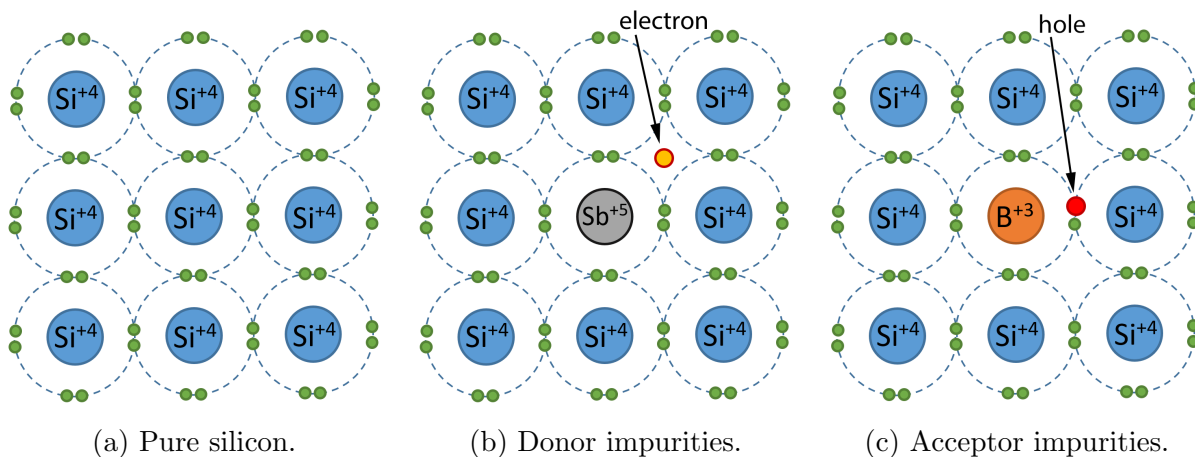


Figure 2.4: A schematic representation of the diamond lattice structure of pure silicon and silicon with impurities. Each atom forms 4 covalent bonds to its neighbours.

A near 100% silicon purity can be produced in the silicon industry [46] but some impurities are always present. The doping of additional impurities can be used to change the electrical properties of the silicon by adding or removing electrons. These impurities are referred to as donor impurities if they increase the number of electrons in the lattice. Conversely, acceptor impurities reduce the number of electrons through the introduction of additional holes.

Donor impurities are typically Group V elements (P, As, Sb) [48] which means they have 5 electrons in their outermost shell. The effect of adding arsenic to the electron arrangement is shown schematically in Figure 2.4b. 4 of the 5 electrons in the outermost shell of arsenic form covalent bonds with neighbouring silicon atoms. A semiconductor containing donor impurities is called n-type after the increased number of nearly free

negative charge carriers.

Acceptor impurities are typically Group III elements (B, Al, Ga, In) [48] and contain 3 electrons in their outer most shell. These impurities therefore only form 3 covalent bonds with neighbouring silicon atoms. The position of the fourth covalent bond (if it was pure silicon) now contains a single electron and a hole. Acceptor impurities therefore also contribute to increasing the conductivity of a silicon crystal. Figure 2.4c depicts a boron impurity in a silicon crystal. A semiconductor containing acceptor impurities is called p-type after the increased number of positive charge carriers (holes) free to move through the lattice at room temperature.

The addition of donor or acceptor impurities to the silicon introduces additional energy states within the otherwise forbidden energy band-gap. These energy states exist close to the conduction band or valence band for donor impurities or acceptor impurities respectively. Only small excitation energies are required in order to liberate electrons or holes from these additional energy states. Consequently, there is a much higher charge carrier concentration at a given temperature compared to intrinsic silicon. Figure 2.5 shows a representation of these additional energy states within the band gap due to impurities.

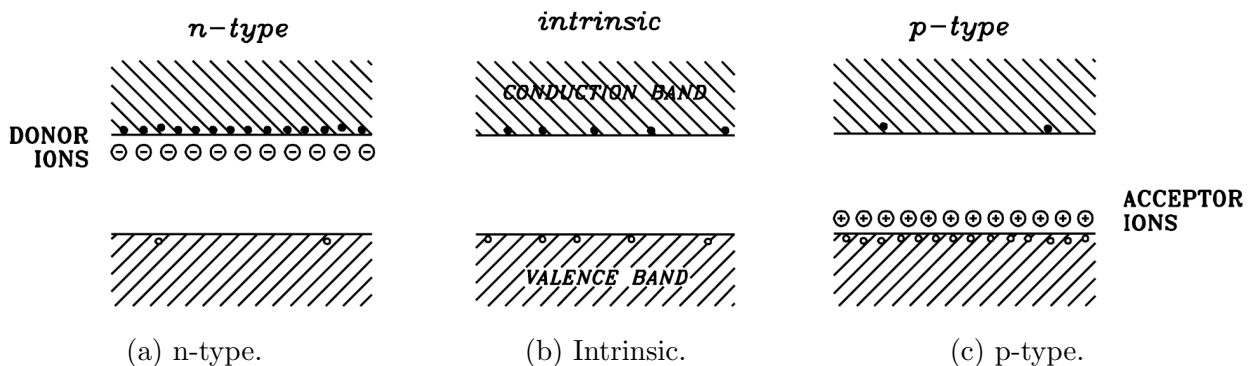


Figure 2.5: A schematic representation of the band gap of n-type, intrinsic and p-type semiconductors [41]. Excitation from an energy state within the forbidden region results in an electron and a fixed positive ion, or a hole and a fixed negative ion.

2.1.4 Charge Carrier Migration

At room temperature, the additional charge carriers added to the semiconductor through the doping of impurities act as free particles. These charge carriers therefore undergo diffusion in the presence of a concentration gradient. The current produced from such movement is called the diffusion current. The flux of charge carriers, \vec{F} , if a gradient exists in their density is given by

$$\vec{F} = -D\vec{\nabla}n \quad , \quad (2.1)$$

where D is the diffusion coefficient and n is the charge carrier concentration [46]. The diffusion current density, \vec{J}_d , can then be defined as

$$\vec{J}_d = -qD\vec{\nabla}n \quad , \quad (2.2)$$

where q is the charge of the carrier [46].

The application of an external electric field, \vec{E} , exerts a force on the free charge carriers and causes them to drift. This is called the drift current. The drift current density, \vec{J}_D , can then be defined as

$$\vec{J}_D = q\mu\vec{E}n \quad , \quad (2.3)$$

where μ is the drift mobility of the charge carrier [46].

The combination of both charge migration mechanisms therefore gives a total charge

carrier current density of [46]

$$\vec{J} = \vec{J}_D + \vec{J}_a = q\mu\vec{E}n - qD\vec{\nabla}n \quad . \quad (2.4)$$

2.1.5 A p-n Junction

The combination of p-type and n-type semiconductors at a boundary has advantageous properties which enable it to be used for electronics and particle detection. This boundary between the two types of semiconductor is called a p-n junction and shows diode characteristics where current flows predominantly in one direction with an applied voltage [41]. A schematic representation of a p-n junction is shown in Figure 2.6.

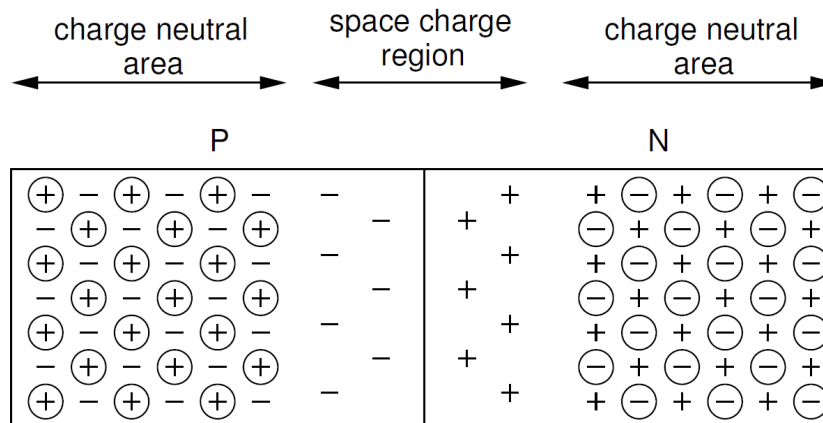


Figure 2.6: A p-n junction in equilibrium [44]. Mobile charge carriers are indicated with circles and combine within the depletion region. The remaining immobile ions set up an opposing electric field which limits further combination.

The presence of the boundary between the two types of silicon creates a steep gradient in the charge carrier density. The mobile charge carriers consequently undergo diffusion and combine in the region surrounding the boundary. This region of combined charge carriers is called the depletion region. In the ideal case it can be considered that all dopants are ionised within the depletion region. The extent of the depletion region is given by the

equation

$$x_p N_A = x_n N_D \quad , \quad (2.5)$$

where N_A is the number density of negative immobile ions on the p-side and N_D is the number density of positive immobile ions on the n-side. $-x_p$ and x_n are the depletion depths on the p-side and n-side respectively [46]. A representation of the distribution of charges at a boundary is shown in Figure 2.7a.

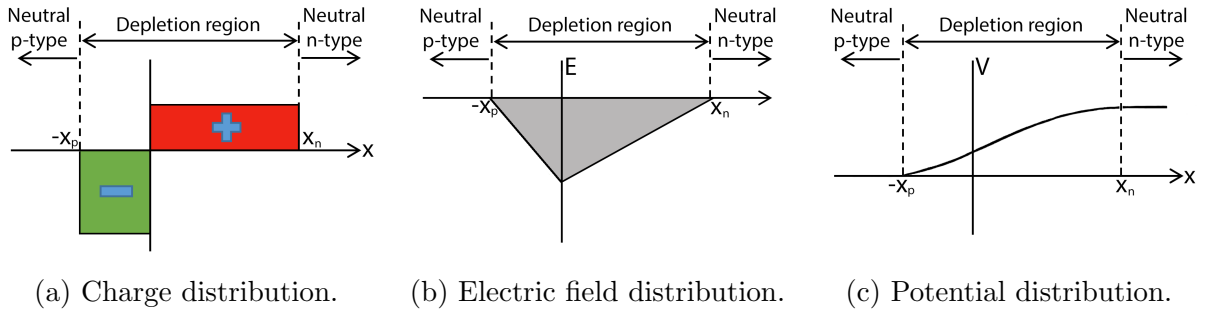


Figure 2.7: The distribution of charge, electric field and potential at a boundary between a p-type and n-type semiconductor.

The distribution of electric field and potential can be determined through Poisson's equation

$$\nabla^2 V = -\frac{\rho}{\epsilon_r \epsilon_0} \quad , \quad (2.6)$$

and the relation between the electric field induced by a potential according to

$$E = -\nabla V \quad , \quad (2.7)$$

where V is the potential, E is the electric field strength, ρ is the charge density, ϵ_r is the relative permittivity of the medium and ϵ_0 is the permittivity of free space. Substitution

of Equation 2.7 into Equation 2.6 gives an expression for the electric field strength in the depletion region. This can be solved through integration which yields a linear relation with distance from the boundary according to

$$E(x) = \begin{cases} \frac{-eN_A}{\epsilon_r\epsilon_0}(x + x_p) & \text{for } -x_p \leq x < 0 \\ \frac{eN_D}{\epsilon_r\epsilon_0}(x - x_n) & \text{for } 0 \leq x < x_n \end{cases} .$$

This relationship is shown in the Figure 2.7b between the boundary limits $-x_p$ and x_n which describe the extent of the depletion region.

The distribution of the potential across the depletion region can similarly be determined through further integration of the electric field relationships derived, yielding

$$V(x) = \begin{cases} \frac{eN_A}{2\epsilon_r\epsilon_0}(x + x_p)^2 & \text{for } -x_p \leq x < 0 \\ V(0) - \frac{eN_D}{\epsilon_r\epsilon_0}\left(\frac{x}{2} - x_n\right)x & \text{for } 0 \leq x < x_n \end{cases} .$$

$V(0)$ in the expression is the potential at $x=0$. This relationship of the potential describes a quadratic relationship with distance from the boundary which is shown in Figure 2.7c. The electric field which is formed from these immobile ions opposes any further diffusion current with a drift current. There is no net current once this equilibrium is established [46].

The extent of the depletion region can be varied by applying a voltage across the boundary. This can be either of the form of a forward or a reverse bias voltage. A positive voltage

is applied to the p-type silicon and a negative voltage to the n-type for a forward biased configuration. The positive bias voltage on the p-type silicon sets up an electric field which acts in the opposite direction to the field set up by the immobile ions. This results in an additional contribution to the drift current towards the n-type silicon and reduces the width of the depletion region [46] and allows large currents to flow through the device.

Alternatively, the depletion region may be extended by applying a reverse bias voltage across the boundary. This is where a negative voltage is applied to the p-type silicon and a positive voltage to the n-type through contacts on either side of the semiconductor. This external field contributes a drift current towards the p-type silicon and so results in an extension of the depletion region and very little current flow through the device. The extension of the depletion region across the entire bulk of the semiconductor is possible by applying a sufficient bias voltage providing the doping concentrations are very low. It is favourable to extend the depletion region for the detection of charged particles as electron-hole pairs generated when a particle traverses the semiconductor separate in the field. The separating charges which move in the field created by the applied potential result in a current signal being induced in the circuit connected to the external contacts [46].

2.2 Silicon Strip Sensors

A silicon strip sensor is an example of a device technology which offers the capability of individual proton tracking for proton CT. A schematic representation of an n-in-p silicon strip sensor is shown in Figure 2.8.

An n-in-p silicon strip sensor is made by implanting strips of heavily doped n-type silicon into a near intrinsic p-type substrate. p-in-n silicon strip detectors may also be produced

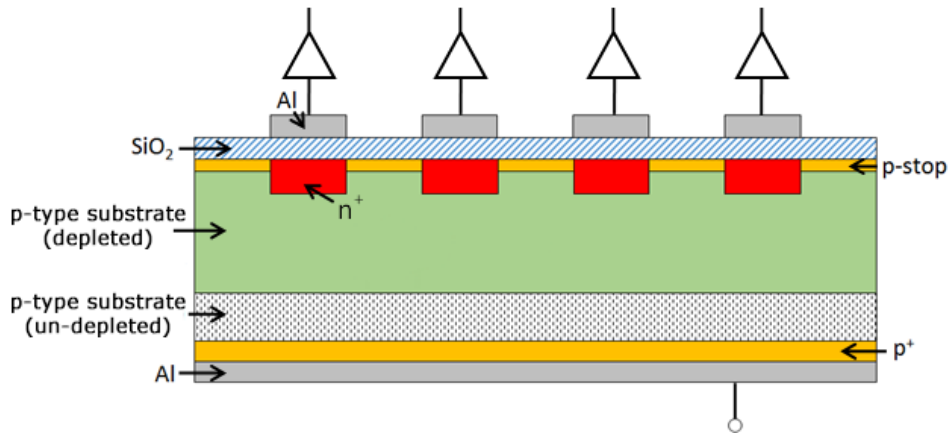


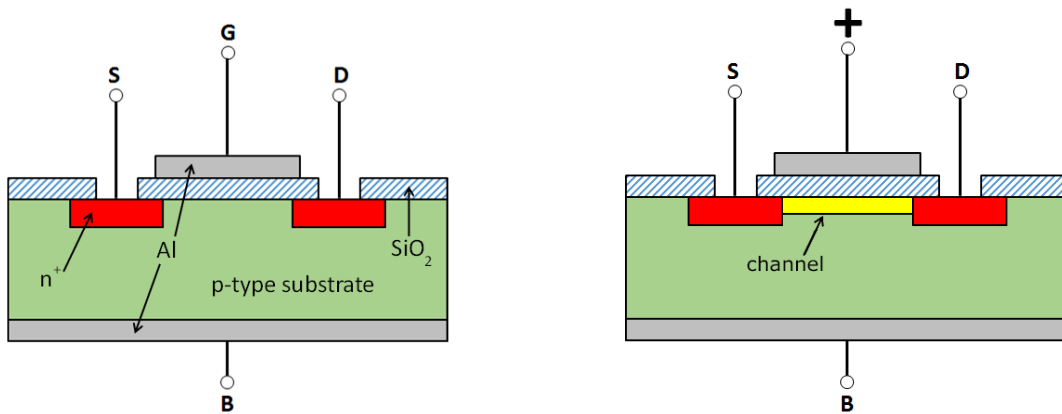
Figure 2.8: A schematic diagram of a silicon strip sensor under a reverse bias voltage with incomplete depletion.

where heavily doped p-type silicon strips are implanted into an n-type substrate. The focus of this work was on n-in-p silicon sensors as they offer improved tolerance to radiation damage compared with p-in-n sensors [49] [50]. A p-n junction is present at the boundary between the silicon types which forms a depletion region. The silicon strips are capacitively coupled to aluminium strips through a silicon oxide layer. These aluminium strips are then connected to readout electronics. Heavily doped p-type silicon is implanted on the back plane of the substrate (in the case of an n-in-p sensor) and has an electrical connection with an aluminium contact. A reverse bias voltage is then set up between the silicon strips (through polysilicon resistors) and the back plane [51]. This reverse bias voltage extends the depletion region from each strip through the substrate until the ideal is reached of full depletion.

Electron-hole pairs are created along the path of the proton passing through the silicon. These electrons and holes then drift under the influence of the electric field set up from the reverse bias voltage. Full depletion ensures the electrons drift under the influence of the electric field through the entire thickness of silicon. This drift induces a charge on the channel which is then processed by the attached electronics. The processing of the signal is discussed in more detail in Section 2.4.

2.3 MOSFET

A Metal-Oxide Semiconductor Field-Effect Transistor (MOSFET) is a three-terminal device which is fundamental in the construction of digital logic structures. The structure of a MOSFET relies on the characteristics of the p-n junction. Figure 2.9 shows a schematic diagram of an n-type MOSFET (NMOS).



(a) No gate voltage.

(b) Gate voltage above threshold voltage.

Figure 2.9: The behaviour of an ideal MOSFET with different voltages on the gate [52].

An NMOS is constructed from a p-type substrate with n-type implants. Two implants referred to as the source, S, and the drain, D, are located in the substrate. Separating these terminals is a gate, G, which is typically insulated from the substrate by a layer of silicon oxide (SiO₂). The contact on the bottom of the substrate is called the body, B. PMOS can also be fabricated where p-type implants are implanted in an n-type substrate.

The application of a positive voltage on the gate with respect to the base causes the minority carriers (electrons) in the p-type substrate to be attracted towards the gate. The insulating layer of silicon dioxide restricts the electrons from passing into the contact. The electrons instead collect below the gate and form a channel which permits charge to flow between the source and the drain. The channel now acts as n-type silicon and is referred to as inverted. This concept is shown schematically in Figure 2.9b with the

channel depicted as the yellow region.

In practice, the applied voltage on the gate must be above a certain threshold voltage to allow charge to flow between the source and the drain. However, a small number of energetic electrons may flow between the source and the drain even if the voltage on the gate is smaller than the threshold voltage. This is called sub-threshold current.

Digital logic structures may be manufactured using circuits of PMOS and NMOS, which act as switches. This technology is called Complimentary Metal-Oxide Semiconductor (CMOS). Another important application of transistors is their use in analogue electronics for the manufacture of amplifier circuits. This utilises the effect that a small change in the gate voltage can allow a rapid variation in the source to drain current, consequently amplifying the signal seen in subsequent circuitry.

2.4 Signal Processing

Each channel of a silicon sensor requires electronics to process the signal before reading out. A schematic representation of basic signal processing for a single channel is shown in Figure 2.10.

The preamplifier exists to amplify the signal produced within the channel by the detected particle. This can be of the form of a current integrator which integrates the current generated within the channel. This signal is then passed to a pulse shaper to shape the signal. A simple pulse shaper is a CR-RC shaper, which consists of a differentiator and an integrator. The differentiator causes the signal to decay giving it a corresponding decay time, τ_d , and the integrator similarly creates a rising edge to the signal with a rise time, τ_i . The resultant signal is then passed to an analogue to digital converter (ADC).

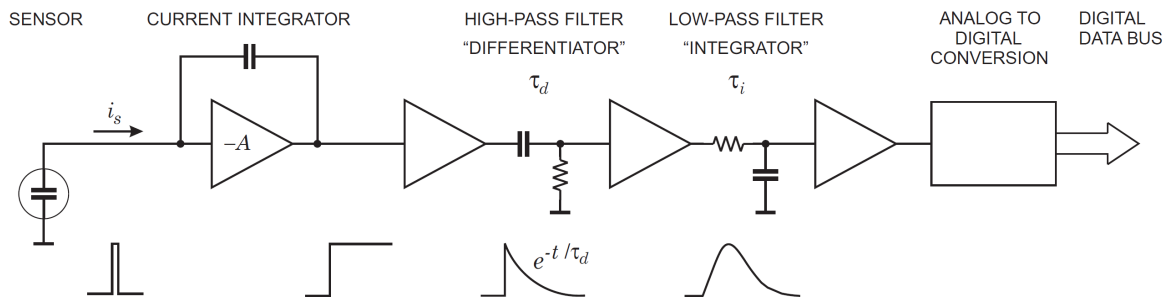


Figure 2.10: A schematic diagram of signal processing by electronics from a single channel of a detector. A signal is generated in a channel which gets integrated by a preamplifier, shaped by a pulse shaper (giving the signal a decay and rise time of τ_d and τ_i respectively) and digitised for readout [53].

It is important to ensure the pulse is decayed by the differentiator to a background level before another signal is generated in the channel. Signals corresponding to two different interactions may otherwise superimpose and give the ADC an incorrect signal size to process, called pile-up. This concept is demonstrated in Figure 2.11. The expected frequency of signals from the sensor therefore specifies the maximum pulse width required to avoid pile-up. Optimisation of the differentiator and integrator (also called the high-pass and low-pass filters) time constants then help with the reduction in low and high frequency noise respectively [41]. Optimisation of the signal to noise ratio is achieved by selecting time constants which maximise the signal and reduce the noise whilst allowing for the required data rate [53].

A simple ADC contains a bank of comparators with varying thresholds. The signal passing through the ADC will trigger those comparators which have a threshold lower than the signal size. The corresponding combination of comparators which are triggered gives a digitised form of the signal size. The resolution of this digitised value depends on the number of comparators and difference between their threshold values. This digitised value can then be sent for readout.

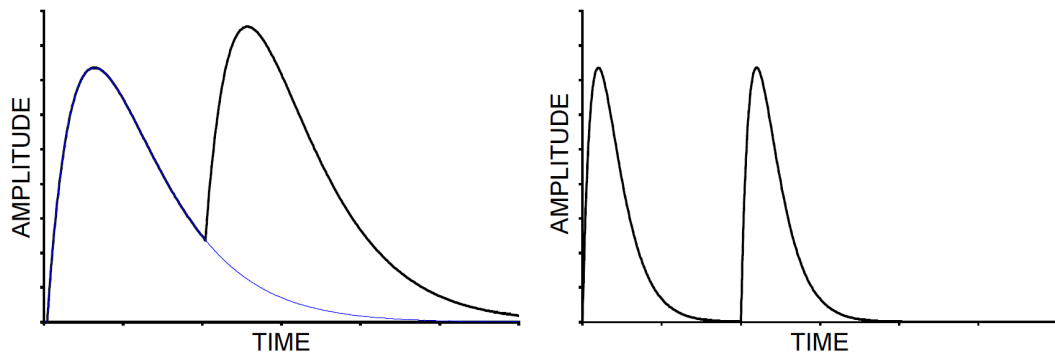


Figure 2.11: A schematic representation of the superposition of signals which have not decayed sufficiently (left) and those which have (right) for accurate signal size analysis. [53].

It is important to ensure that the time the comparators sample the signal distribution is optimal to ensure maximum efficiency of detection. For example, incorrect timing could result in sampling of the distribution like that shown in Figure 2.11 within the tail. Sampling within the tail could result in a signal being below the threshold required to register a hit, even if the true signal exceeded the threshold at its peak.

2.4.1 Readout Architectures

Readout can proceed in binary, digital, or analogue form. Binary readout outputs either a binary 1 or 0 depending on whether the signal processed was above a single threshold or not, respectively. Binary readout does not give any information about the size of the signal processed. This readout architecture makes it useful for particle detection where only a position resolution comparable to the electrode pitch of the device is required.

Both digital and analogue readout architectures provide additional information corresponding to the processed signal. Analogue readout outputs a pulse with a similar shape to a single pulse shown in Figure 2.11. Digital readout alternatively outputs a signal which is quantised in discrete steps. This step size is determined by the number of comparators within the ADC and their maximum/minimum thresholds. The analogue or

digital architecture can be used for energy measurement as well as improve the positional accuracy when tracking. This is because the signal size is related to the energy of the particle, and the distribution of the signal (e.g. if the signal is shared between two neighbouring strips) can be used to further constrain the particle position.

2.5 Ambiguities

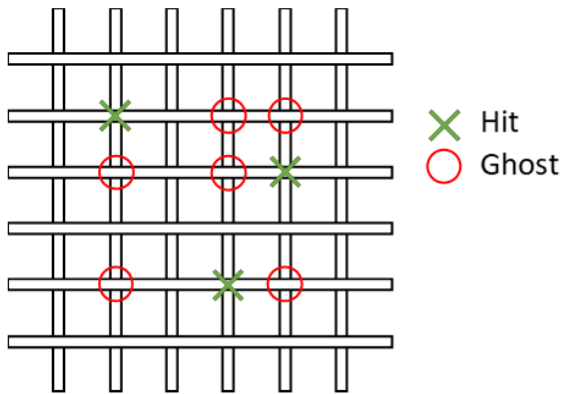
A single strip, which registers a hit on a silicon strip sensor with binary readout, allows reconstruction of a one dimensional coordinate equal to the position of the centre of the strip. The difference between the true proton position and the reconstructed position, for randomly aligned proton tracks, results in a Gaussian distribution [53]. Binary readout (no signal size information) and a negligible contribution to the current from diffusion, in comparison to drift, gives a standard deviation, σ , for this distribution of

$$\sigma^2 = \frac{1}{p} \int_{-\frac{p}{2}}^{\frac{p}{2}} x^2 dx = \frac{p^2}{12} \quad , \quad (2.8)$$

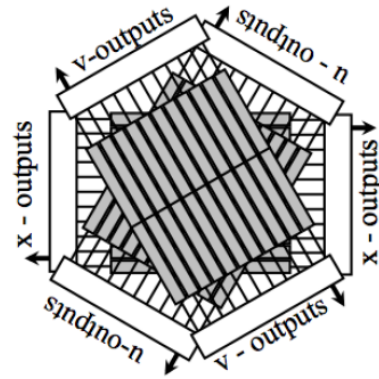
where x is the position of the particle across the strip, and the spacing between the strips is the strip pitch, p . Typical strip pitches are of the order of $100\mu\text{m}$ [54].

The use of multiple silicon strip layers, typically two or three, allows for a two dimensional coordinate to be determined of the traversing particle. It is this technique which underlies charged particle tracking with silicon strip sensors. Two silicon layers placed at 90° with respect to each other is one way to obtain an x-y position for a single proton. A schematic representation of this set-up is shown in Figure 2.12a. A 2D coordinate is determined by reconstructing the position where two intersecting orthogonal strips record a hit.

Difficulties arise when using two layers at 90° if there is more than one proton passing



(a) x-y configuration of strips showing ghost hits.



(b) x-u-v configuration of strips [55].

Figure 2.12: Schematic representation of the problem with x-y configuration due to ghost hits and the alternative x-u-v configuration adopted for tracking to reduce ambiguities.

through the detector when the detector is read out. Reconstruction of the possible points of intersection of all hit strips in the two layers results in n^2 possible positions for n protons passing through the two layers of strips. A ghost hit refers to a possible reconstructed position which was not a true hit position. This therefore means $n^2 - n$ of these n^2 hits are ghost hits.

One method to limit the number of ghost hits, utilised by the PRaVDA consortium [54], is to use an additional strip layer forming an x-u-v configuration. A schematic representation of this configuration is shown in Figure 2.12b. Each layer is rotated at 120° with respect to the previous layer. Multiple protons passing through the system using such a configuration are found to result in a reduced number of possible crossing positions, and therefore ghost hits, when a signal is detected in all three layers. The capability of the tracking system was therefore improved by being able to correctly reconstruct proton positions with more than one proton per readout, providing there was sufficient spacial separation between the protons.

2.6 Silicon Pixel Sensors

Silicon pixel sensors are an alternative technology which can be used for particle detection [43]. The main motivation for pixels for the purpose of proton CT is the problem with ambiguities in the hit location of particles as described in Section 2.5. At least 2 layers of silicon strips are required to get a 2D coordinate position which may still result in ghost locations being measured. Pixels on the other hand are segmented in both x and y dimensions within a single piece of silicon giving an unambiguous 2D hit coordinate. An implanted collection electrode is present in each pixel and read out through attached electronics specific to that channel.

One method of connecting the electronics to the collection electrodes for individual pixels is to fabricate the electronics in a separate, but similarly segmented, wafer of silicon to the collection electrodes [51]. The two silicon wafers are then connected using a bump bonding process, where each collection electrode is connected to its electronics through a solder bump bond [43]. This process still results in 2 layers of silicon (each approximately between $100\mu\text{m}$ and $300\mu\text{m}$ thick [51] [53]) in the proton path for a 2D coordinate, but may still offer a reduction in silicon thickness in comparison to an x-u-v configuration. This reduction in thickness is important for reducing the amount of scatter which occurs as particles traverse the silicon. The impact of scattering is discussed in detail in Chapter 6.

Monolithic Active Pixel Sensor (MAPS) technology is an alternative type of pixel technology in which the electronics of each pixel is built into the same silicon as the collection electrode. MAPS technology therefore has the advantage of 2D coordinate measurement with only a single layer of silicon. This is particularly advantageous for proton CT (discussed in Chapter 3) as scattering from anywhere within the system results in a degradation of the final image (discussion and results in Chapter 6). A MAPS device has the potential advantage of a reduced cost through the use of commercial CMOS

application processing [43], since expensive and difficult high density interconnection processing such as bump-bonding are not required [43]. A schematic representation of a MAPS is shown in Figure 2.13.

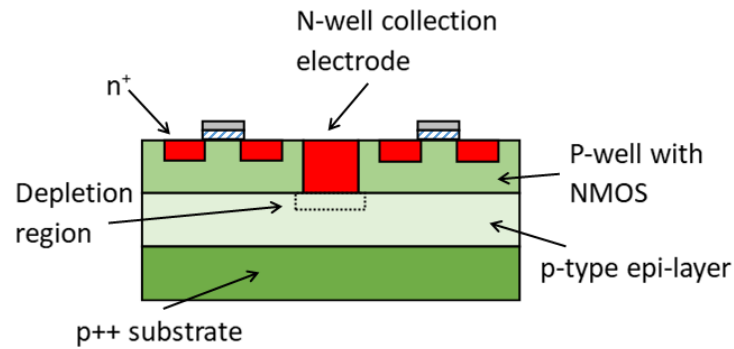


Figure 2.13: A schematic representation of the simplest MAPS design with only NMOS transistors. Additional well structures can be added to achieve full CMOS capability.

Figure 2.13 shows an N-well collection electrode within a lightly doped p-type epitaxial layer. P-wells are implanted into the epitaxial layer to contain the NMOS used in the electronics. These MOSFETs must be implanted within a P-well to isolate the n-type source and drain terminals from the collection electrode. Charge from any signal generated within the epitaxial layer would otherwise also be collected at these terminals.

A small depletion region forms around the N-well and extends into the epitaxial layer. The small depletion region means that any signal generated within the epitaxial layer must diffuse towards the collection electrode to be detected. This results in a slower signal collection compared to biased strip sensors. Relying on diffusion for charge collection also makes the MAPS less radiation tolerant. This is because incident radiation causes displacement damage leading to defect clusters, which can trap slow moving charge carriers within the silicon. This damage to the silicon is primarily caused when an incident particle dislodges a silicon atom from its lattice site; forming a Frenkel pair of the vacancy in the lattice and the interstitial atom [49]. These Frenkel pairs are then free

to migrate through the crystal until they combine with impurities or defects and form stable defect clusters [43]. These defect clusters can trap charge carriers which results in a reduced overall signal [49].

2.6.1 Pixel Readout Architecture

One example of a simple readout architecture of a MAPS is the “rolling shutter”. This architecture contains a diode, reset transistor, a source follower transistor and a row select transistor. The diode is the p-n junction from the collection electrode and the epitaxial layer of the pixel. The circuit diagram of the structure is shown in Figure 2.14.

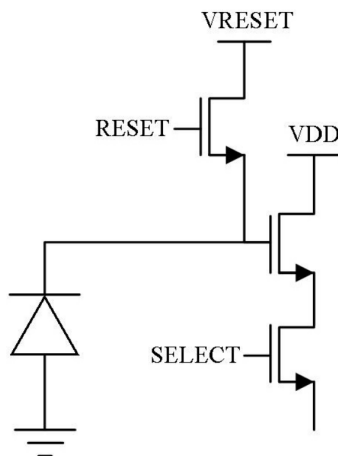


Figure 2.14: A circuit diagram showing the structure of the 3T readout architecture for a silicon pixel device [56].

Variations of the rolling shutter readout exist [57]. For one variation [57], the first row of pixels is selected for reset and immediate readout. This gives a measurement of the baseline signal of each pixel in that row. This process is repeated for all rows in the pixel matrix, with each pixel adding the baseline signal to a column bus contained in each column of pixels. The row select, once cycled over all rows, returns to the first row to read out the signal induced during the integration time (time to cycle through all rows of the pixel matrix). This signal is similarly passed to the column bus and repeated for

all rows. The difference between the signal from the second cycle and the baseline signal from the first cycle is the signal induced in that pixel from interacting particles during the integration time. In this way the signal from the sensor can be read out row by row, looping repeatedly through the entire pixel matrix to read out subsequent time frames.

Chapter 3

Proton Computed Tomography

3.1 Motivation for Proton Computed Tomography

A 3D map of the stopping power of the tissues within a patient is required to plan a proton therapy treatment. Currently the accepted technique of determining proton stopping power is to first perform an x-ray CT. Photons are projected through the patient from a series of angles. A detector placed on the far side of the patient then detects the number of photons as a function of spatial position. This gives a 2D map of the absorption of photons through the patient for each angular projection. Appropriate reconstruction software then uses these 2D absorption maps to produce a 3D map of the tissues within the patient. This 3D map is typically segmented into $1\text{mm} \times 1\text{mm} \times 1\text{mm}$ volumes called voxels. The reconstruction software assigns each voxel with a measure of Hounsfield Units (HU) as described by the equation

$$HU = 1000 \frac{\mu - \mu_{water}}{\mu_{water} - \mu_{air}} , \quad (3.1)$$

where μ is the average linear attenuation coefficient in the medium, μ_{water} is the linear attenuation coefficient for water and μ_{air} is the linear attenuation coefficient for air. Hounsfield units are the standard unit used for an x-ray CT image as it describes the

attenuation of x-rays.

A calibration curve is used to convert the HU to proton stopping powers. This calibration curve associates a measure of HU to an electron density using a series of known materials. The Relative Stopping Power (RSP) is defined by

$$RSP = \frac{S_p^m}{S_p^w} , \quad (3.2)$$

where S_p^m is the stopping power of the material and S_p^w is the stopping power of water. The relation between stopping power and Hounsfield units has been experimentally tested and the uncertainty stated as 3.5% of the proton range within the traversed medium [58]. It has been found that the relative stopping power of lower density materials follows a near linear relation with electron density [59]. Difficulties arise for higher density materials such as bone due to the differing dependence of HU and stopping power on the atomic number Z and atomic mass A for photons and protons.

Accurate stopping power determination is not only important for initial treatment planning, but also for optimisation during treatment. Unlike set-up and range uncertainties, anatomical changes are not typically accounted for when planning proton treatments [60]. These anatomical changes to a patient between treatment fractions can have a severe negative impact on the delivered treatment by affecting the position of the Bragg peak [61]. Inaccurate positioning of the high dose region causes insufficient dose to the tumour and unnecessary dose to healthy tissue [61]. Having the means to accurately measure the stopping power when the patient is on the couch and ready for treatment delivery allows for in situ optimisation of the treatment. Current proton therapy centres typically use cone beam CT (using x-rays) for patient position monitoring during treatment. The use of cone beam CT in adaptive planning for Intensity Modulated Proton Therapy (IMPT) however appears to be beyond the capability of these

systems [62]. Proton CT, which could offer accurate proton stopping power determination and negate the need for an additional imaging system on the gantry (through the use of the already present proton beam used for treatment), offers a far more attractive solution.

3.2 Stoichiometric Calibration

A calibration curve can be measured at each clinical facility based on measurements of a selection of tissue equivalent materials with well defined properties. These properties include the density and the elemental composition. Usable samples typically have altered chemical compositions from their real counterparts which typically does not cause problems for a dosimetry perspective as this is more focused on the density of the material. The change in the chemical composition however affects the electron density within the medium and consequently how protons interact. Uncertainties therefore arise in values of the calibration curve due to the tissue substitute properties differing from those of the true tissue it resembles.

It is possible to reduce such uncertainties by performing a calibration using the stoichiometric method. This method can be summarised as

1. perform an x-ray CT of tissue substitutes with well known densities and chemical composition
2. determination of parameters specific to the accelerator using the measurements of tissue substitutes
3. calculation of theoretical CT numbers and RSP based on literature stated densities and chemical compositions of human tissues
4. applying a linear regression fit to the calculated values to produce a calibration curve

The calibration curve produced from such a method was found to be less sensitive to the tissue equivalent materials and has therefore become the most widely adopted method to perform calibration within proton therapy centres around the world [58].

An example of a calibration curve for the conversion of HU to RSP is shown in Figure 3.1.

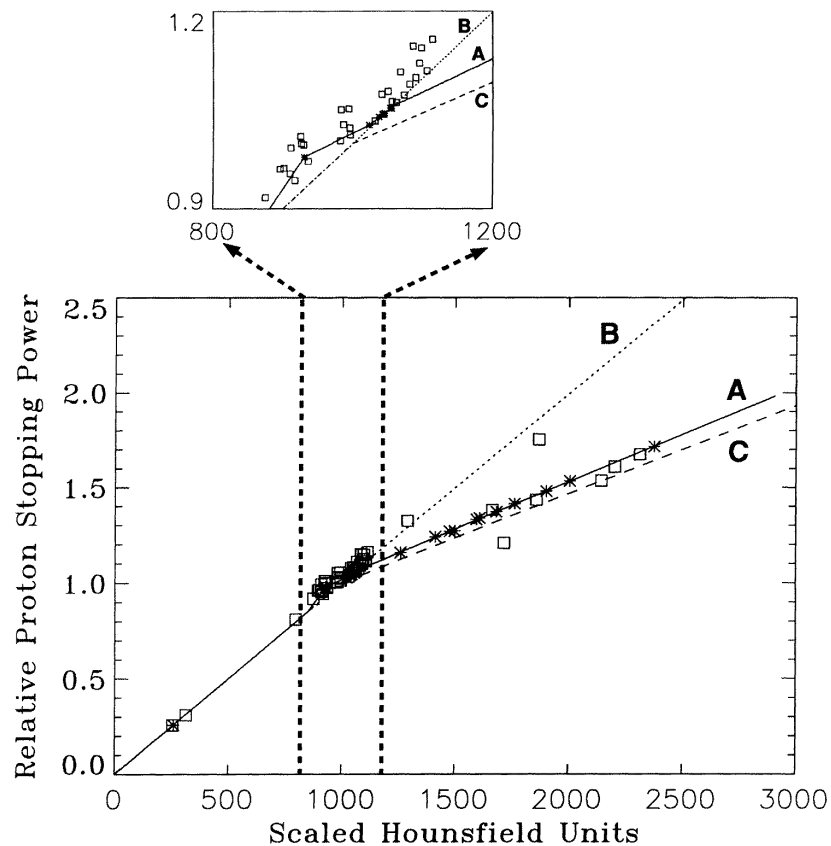


Figure 3.1: A calibration curve for the conversion of HU to RSP. The solid line (A) shows the Stoichiometric calibration method. Lines B and C represent the tissue substitute calibration method for Mylar/Melinelx/PTFE and B110/SB5 materials respectively. The square points are calculations based on tissue substitute materials and the stars represent calculations based on the chemical composition of real tissues [63].

3.3 Proton Stopping Power Uncertainties

The contributing factors to the 3.5% uncertainty on the range of the proton through a medium can be defined as

- A uncertainties associated with the CT image
- B uncertainties in the stoichiometric formulas used to determine theoretical CT numbers
- C uncertainties in the composition of human tissues
- D uncertainties in the mean excitation energies of materials used to calculate RSP
- E uncertainties in dose algorithms not accounting for energy dependence on RSP

The uncertainty associated with the CT image arises from intrinsic uncertainties of the imaging method. Factors such as immobilisation devices and patient couch can cause uncertainties in the image as well as day to day variations of the patient anatomy/position.

The stoichiometric calibration method has been shown to reduce the uncertainties associated with material substitutes not being truly representative of their real tissue counterparts. However, there remain uncertainties associated with the parameterisation of the formula used for this method; consequently impacting the RSP uncertainty.

Stoichiometric calibration uses ICRU standard definitions for tissue compositions. There remain natural fluctuations of body composition amongst the general population and this therefore introduces patient specific uncertainties.

RSP is defined relative to water but there remain uncertainties associated with the measurement of the excitation energy of water [58]. This uncertainty of the mean excitation energy consequently leads to an uncertainty of $\sim 1\%$ to the determined stopping power of a material [58]. A direct measurement of the mean excitation energy of tissue equivalent materials is not possible, and leads to a larger uncertainty of $\sim 1.4\%$ for the calculated stopping power relative to water [58].

The final defined uncertainty relates to some dose algorithms used for treatment not accounting for any variation in the RSP with energy. The RSP does remain approximately constant with energy, but this approximation contributes an additional uncertainty to the calibration [58].

The four last contributing factors to the overall uncertainty described can be completely removed through the use of a proton CT system. There will naturally remain an uncertainty with CT imaging itself. However, these uncertainties associated with the calibration to determine RSP are removed by measuring the RSP directly.

3.4 General pCT System Layout

A schematic representation of a typical proposed pCT system is shown in Figure 3.2. Such a system is based on the projection of protons through a rotating phantom to obtain a 3D image of the internal structure. Prototype systems typically rotate the phantom within the system as opposed to rotating the pCT system itself for simplicity. This replicates the process in a clinical setting where the patient would be stationary and the system rotated around them on a gantry. Tracking detectors are placed in front and behind the phantom to obtain information about the incoming and outgoing trajectories of the protons. These trajectories can be used to find the location of entry and exit on the surface of the phantom. Algorithms are subsequently used to determine the most likely path (MLP) the proton took through the phantom. A Residual Energy Range Detector (RERD) is also required to measure the outgoing proton energy after it has passed through the phantom. The energy deposited within the phantom by the proton is then calculated as the difference between this final measured energy and the incident energy of the proton. This assumes the initial proton energy is well defined from the proton accelerator.

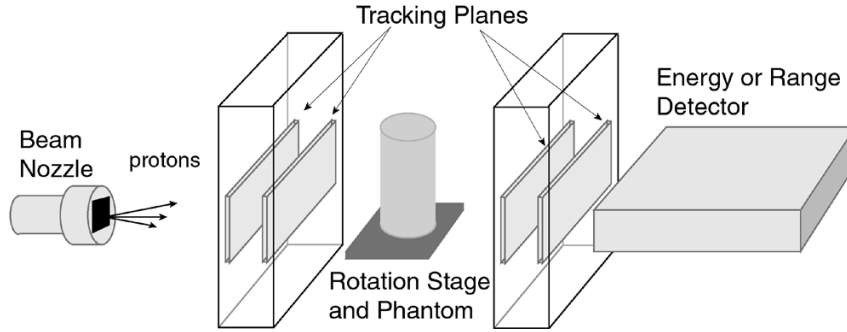


Figure 3.2: A schematic representation of a pCT system comprising tracking planes and a Residual Energy Range Detector used to image a phantom [64].

Multiple technologies exist for the construction of a pCT system and a number of groups have developed prototypes [64] [65] [66] [67] [68] [69]. Examples of technologies used for the tracking detectors include crossed scintillating fibres (from a collaboration between Northern Illinois University, Fermi National Accelerator Laboratory and the University of Delhi) [67] and silicon strip sensors (from the pCT and PRIMA collaborations) [65] [69] [70]. Prototypes also include technologies such as scintillators (from Loma Linda University) [65] and NaI detectors (from Niigata University) [66] for the RERD. The main focus of this work is using and adapting the system developed by the PRaVDA consortium [54] so other systems are not described in detail.

3.5 Water Equivalent Path Length

The Water Equivalent Path Length (WEPL), W , is the equivalent distance through water which the proton travelled through a material, and is given by

$$W = \int_L RSP(z) dz \quad , \quad (3.3)$$

where $RSP(z)$ is the relative stopping power at the distance z along the path of L , as defined in Equation 3.2.

The total WEPL of the proton, W_T , can be represented as the sum of its range through individual parts of the pCT system. This sum can be broken down as

$$W_T = W_t + W_p + W_r \quad , \quad (3.4)$$

where W_t is the WEPL through the trackers, W_p is the WEPL through the phantom, and W_r is the WEPL through the RERD.

The Bragg-Kleeman rule, as defined in Equation 1.9, relates the proton range, R , with the proton energy, E . It is this relation which can be used to determine W_r if measuring the energy in the RERD. A single scintillator used as a calorimeter is an example of measuring energy of the proton directly. This method however has the difficulty of a poorer energy resolution when little energy is deposited within the calorimeter. This technique is further discussed in Section 3.5.1.1. An alternative method is to measure the residual range of the proton by having many thin layers interspaced with absorber material to degrade the proton energy. The final layer in which the proton stops then allows the WEPL through the RERD to be determined, and subsequently the WEPL through the phantom. This technique is further discussed in Section 3.5.1.2.

3.5.1 WEPL Uncertainty

There is an intrinsic limit of 1.1% uncertainty on the residual range due to the limits of range straggling [64]. The requirements of an energy measurement and direct proton range measurement RERD to achieve this theoretical limit on the resolution are discussed here.

3.5.1.1 Energy Measuring RERD

The proton range up to the RERD which includes both W_t and W_p has an uncertainty, $\sigma_{t,p}$, of [33]

$$\sigma_{t,p} \approx 0.011(W_t + W_p) \quad . \quad (3.5)$$

The uncertainty in the RERD, σ_r , relates to the Bragg-Kleeman relationship given in Equation 1.9 according to [33]

$$\sigma_r \approx pW_r\delta E \quad , \quad (3.6)$$

where p is an experimentally derived parameter [35] and δE is the energy resolution of the calorimeter given by [33]

$$\delta E = \frac{\sigma_E}{E} \quad , \quad (3.7)$$

and σ_E is the uncertainty (standard deviation) on the energy measurement. The uncertainty on the total WEPL of the proton, σ_T , is therefore the quadrature relation between Equations 3.5 and 3.6 [33]

$$\sigma_T \approx \sqrt{(0.011(W_t + W_p))^2 + (pW_r\delta E)^2} \quad . \quad (3.8)$$

A calorimeter which measures the energy of the proton therefore requires an energy resolution of <1% to achieve the limit on the uncertainty caused by range straggling [33]. This limit is reached by making the contribution to σ_T from the RERD negligible. Developing such a system capable of measuring individual protons with sufficient resolution is difficult given the readout rates required to operate at clinical facilities.

3.5.1.2 Range Measuring RERD

The alternative approach of measuring the proton range directly in the RERD has a contribution from the intrinsic uncertainty on the total WEPL, σ_T , given by

$$\sigma_T \approx 0.011W_T \quad . \quad (3.9)$$

N layers in the RERD gives an uncertainty on the measured RERD WEPL of

$$\sigma_r = \frac{r_n}{\sqrt{12}} \quad , \quad (3.10)$$

where r_n is the thickness of the n th layer. The origin of Equation 3.10 is described in more detail in Section 2.5 for the similar application of position resolution of a silicon strip detector. Equations 3.9 and 3.10 therefore give a total uncertainty on the WEPL of

$$\sigma_T \approx \sqrt{(0.011W_T)^2 + \left(\frac{r_n}{\sqrt{12}}\right)^2} \quad . \quad (3.11)$$

A RERD which measures the range of the proton consequently requires between 60 and 100 layers for clinical $\sim 200\text{MeV}$ energy protons in order to achieve the range straggling limit [33]. This is based on the working principle of either plastic scintillating detectors for both energy degradation and detection, or Perspex interspaced with silicon detectors for energy degradation and detection respectively. The RERD is required to degrade the maximum clinical proton energy to detect all protons, which equates to approximately 38.5cm of water for a 245MeV beam [26]. This therefore becomes difficult to achieve for a clinically relevant system due to the size and complexity of such a device.

3.6 PRaVDA

The Proton Radiotherapy Verification and Dosimetry Applications (PRaVDA) consortium is a team of particle physicists, medical physicists and electronic engineers funded by the Wellcome Trust [71]. The goal of this project was to develop a system for the monitoring of the energy, fluence and distribution of a proton beam as well as to perform proton Computed Tomography (pCT). The successes of the PRaVDA system lay the foundations for the further work conducted in the studies to be described in the following chapters. This section describes the PRaVDA system shown in Figure 3.3.

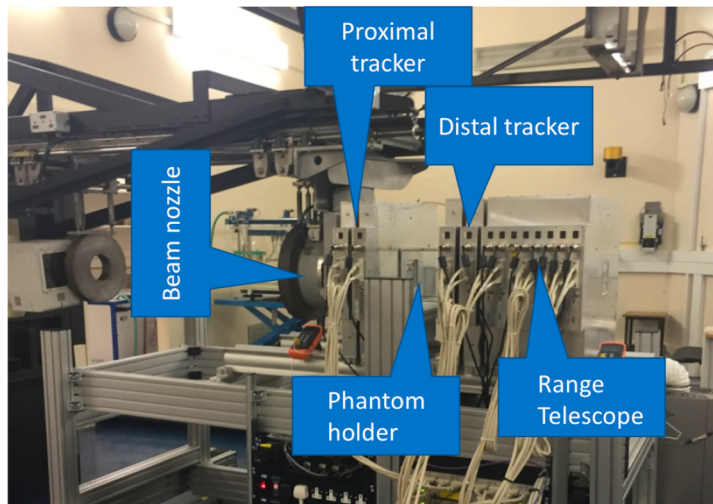


Figure 3.3: The PRaVDA system showing proximal and distal trackers, phantom, and the Range Telescope [68].

3.6.1 Tracking Detectors

The tracking detectors used for the PRaVDA project are based on silicon strip technology. Each tracker unit is constructed of three n-in-p (for greater radiation hardness) silicon strip layers rotated at 120° with respect to the last. Each layer has a $93\text{mm} \times 96\text{mm}$ active area of silicon with a thickness of $150\mu\text{m}$ and a strip pitch of $90.8\mu\text{m}$ [54].

The 10cm strips themselves are split in the centre and read out from both sides. The

layers were designed with strip halves in order to increase the number of protons which could be detected per readout cycle. For example, in a single readout cycle, if two protons were to hit a single 10cm strip at a distance of 6cm apart, only a single proton would be measured. For the same scenario, but with 5cm long strips read out from each side, the strip on each strip half would record a hit and therefore count two protons. Figure 3.4 shows a single silicon strip layer and the readout electronics on both sides of the detector.

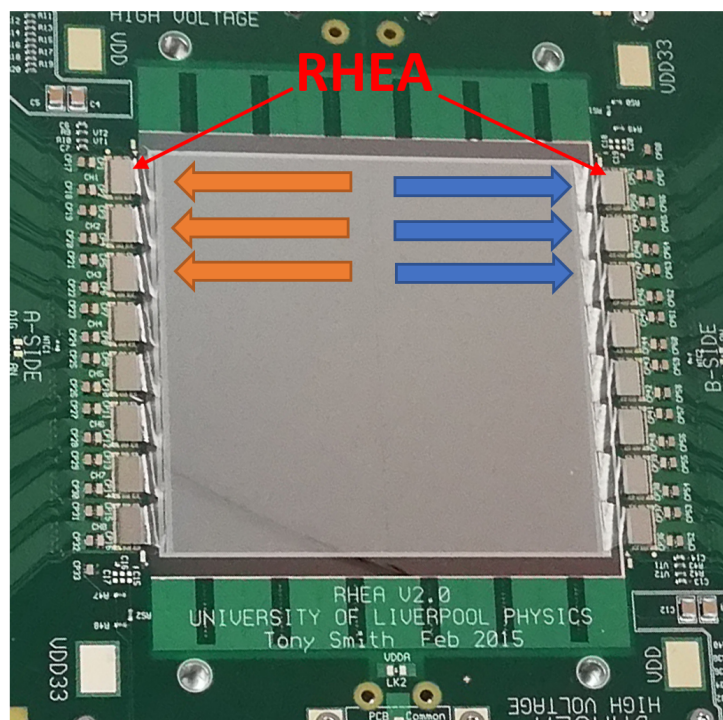
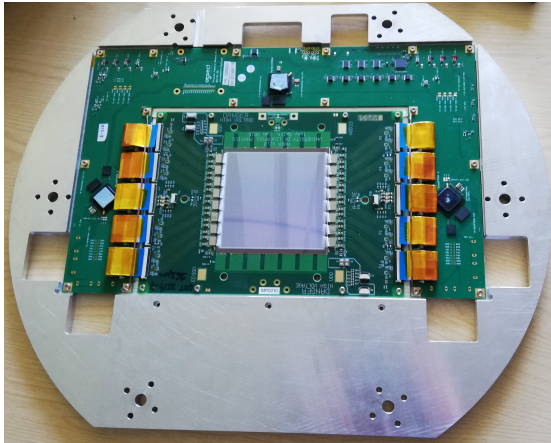


Figure 3.4: A single PRaVDA silicon strip layer showing readout from both sides. Each arrow represents 128 channels read out by an ASIC.

The silicon layers are wire bonded to their associated readout electronics and mounted on 12mm thick aluminium stiffening frames [54]. These stiffening frames were manufactured with holes for the active area of silicon, ensuring no interaction with the beam, and allowed for precise alignment of the layers. Figure 3.5a shows the mounting of a silicon layer on one of these stiffeners. Figure 3.5b shows how three of these layers are rotated with respect to each other within a single tracker unit.



(a) A silicon strip layer mounted on an aluminium stiffener.



(b) Three silicon layers precision aligned at 120° with respect to each other in a tracker unit.

Figure 3.5: Images showing the mounting of silicon strip layers on 12mm thick aluminium stiffeners and inside a tracker unit.

The readout chips were designed for the specific application of the PRaVDA project and are called RHEA (Rapid High-speed Extended ASIC) [54]. RHEA is a binary chip which is connected to 128 strips [54]. The chip reads out at a frequency of 26MHz when operating in pCT mode, and allows for up to 4 strips per chip with signal above threshold to be read out per frame. The readout of the strips is synchronised with the cyclotron clock to ensure that the maximum number of proton tracks are reconstructed through the system. The importance of this synchronisation of the system with the cyclotron is explained in more detail in Section 3.6.3.

Four of these tracking units were used; two placed before and two after the object being imaged. Each tracker unit gives an x-y coordinate. The z coordinate is assumed to be the position of the middle silicon layer. The two sets of two x-y-z positions then allow a proton trajectory to be determined; from which the entry and exit positions on the phantom can be calculated.

3.6.2 Range Telescope

The device used in the PRaVDA project as the RERD was called the Range Telescope [72]. The Range Telescope operated by measuring the residual proton range as outlined in Section 3.5.1.2. The device comprised 22 silicon strip layers each separated by 12mm. These silicon strips were identical to those used in the trackers (discussed in Section 3.6.1) as shown in Figure 3.5a and so reduced the cost of manufacture and simplified the system design. The silicon strips were all oriented along the same axis. The trajectory of the protons determined from the outgoing trackers just before the Range Telescope still allowed the tracks of multi-proton events to be separated, despite having only the single orientation of strips.

A 2mm thick sheet of Perspex was placed in the 12mm space between each silicon strip layer. The Perspex absorbed some of the proton energy in order to increase the water equivalent thickness between each detection layer. The last layer in the Range Telescope where a proton was detected could then be used to identify the residual range of the proton after exiting the phantom. This residual range was determined using an experimentally obtained calibration curve relating the residual proton range to the last traversed layer.

The Range Telescope managed to achieve a WEPL uncertainty of 1.1% which is at the limit due to range straggling [64]. The caveat of this system was that a compensator was used to degrade the energy of protons passing through less dense regions of the phantom. This ensured the protons exiting the phantom were approximately the same energy and could be contained within fewer layers of a range telescope. The recent development towards spot scanning facilities and Intensity Modulated Proton Therapy treatments means that compensators are less practical. Further development is therefore required for a practical clinical system, but this acts positively as a proof of concept.

3.6.3 Phase Sweep

The RHEA chip has an inbuilt dead time during readout throughout which it cannot detect any additional protons. Testing of the PRaVDA system showed that protons may be lost part way through the system if they enter a layer during this dead time. Similarly, protons not detected in the proximal trackers may be detected in the outgoing trackers as the system returns to a live state. This causes the problem of losing track reconstruction efficiency. The clinical consideration of this is an increased dose to the patient for a given resolution of the reconstruction, which is detrimental to patient outcome.

The operation of a cyclotron relies on a clock. This clock causes the polarity of the dees within the cyclotron to switch. Switching ensures a constant acceleration of the protons until they are ejected. This also means that protons are emitted in bunches at this clock frequency, rather than as a continuous beam. The position along a single cycle of this waveform at which the protons are emitted remains approximately constant during operation. Figure 3.6 depicts the cyclotron clocking waveform. The regular position of protons being emitted along this waveform is also represented.

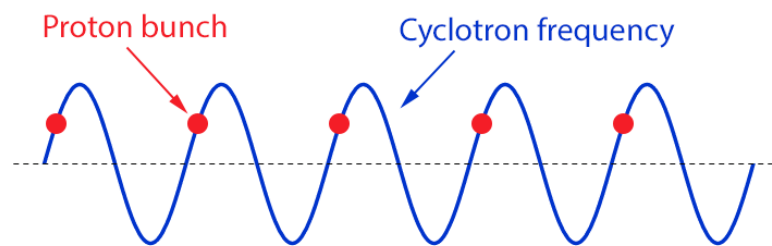


Figure 3.6: A cyclotron clocking waveform showing the regular structure of proton emission.

The speed of proton travel depends on the energy of the proton. It is therefore critical to synchronise the system with the cyclotron clock frequency to ensure a maximum tracking efficiency. This is done by setting a delay between the system reading out

and a particular point on the cyclotron frequency. This delay is called the phase delay. The setting of an appropriate phase delay ensures that the system is reading out when protons are passing through, and the dead time is between proton bunches.

A phase sweep is a test performed in order to find the optimal phase delay between the system readout and the cyclotron clock frequency. The phase delay is varied in regular increments from 0° to 360° with no material in the phantom position. The system is read out, and the tracks are reconstructed for each phase delay setting. The tracking efficiency is then defined as the ratio of protons successfully tracked through the system and the number of reconstructed hits in the first tracker unit. Protons which pass through the system and additional material such as a patient move slower. Hence, the optimal phase delay setting is chosen as a phase delay shortly after the tracking efficiency reaches its maximum. This is because there is more time for the slower moving protons to pass through the system during its live time before it enters its dead time. An example of the relationship between the phase delay and the track reconstruction efficiency is shown in Figure 3.7.

3.6.4 Data Readout

The data from the PRaVDA system is read out at a regular 26MHz to match the frequency of the Birmingham MC40 cyclotron. Charge is deposited in a strip (or shared by neighbouring strips) in each silicon layer when a proton passes through. The RHEA chip processes the generated charge in each strip (128 strips per RHEA) and discriminates whether it was above a set threshold. This threshold is variable and the low noise of the strips ensures near 100% efficiency of detection is possible. The strip number is sent for readout if the charge was above this threshold.

A different timestamp is assigned to every cyclotron clock cycle as RHEA reads out.

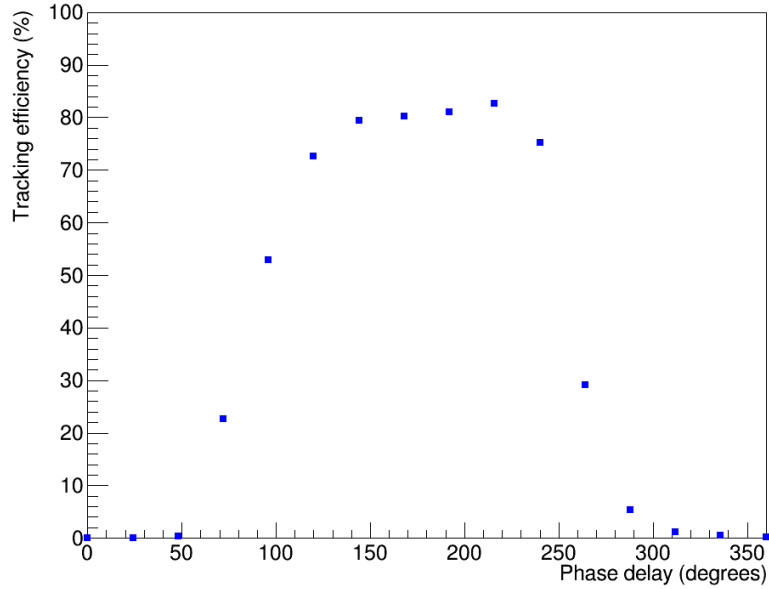


Figure 3.7: Phase sweep relation between the phase delay and track reconstruction efficiency of the system.

Up to 4 strip numbers are read out per silicon layer for each timestamp in a regular format. This format is processed by a series of multiplexers which synchronise all strip layers together throughout the system. The final multiplexer outputs a binary file with corresponding strip numbers, segmented by timestamp.

3.6.5 Track Reconstruction

The binary file outputted from the PRaVDA system is then processed using the Routine for Synchronisation, Event building, Tracking and Alignment (ROSETA) algorithm. This algorithm calculates the position of proton “hits” in each of the four tracker units, and combines the hits to form “tracks” through the system. The algorithm can be segmented into the following steps.

1. Build 2 layer strip crossing points, called “crosshairs”.

The coordinates of all strip crossing points from each 2 layer combination (x-u,

$x-v$, $u-v$) in a tracker are calculated for a given timestamp. This is repeated for all trackers.

2. Build “virtual pixels”.

3 crosshairs, one from each of the 2 layer combinations, form a virtual pixel. The crosshairs act as the corners of the virtual pixel which has a triangular shape. Every possible combination of 3 crosshairs is considered if more than one proton passes through the tracker in a given timestamp. Only the smallest in area of these virtual pixels are considered for the following step. The coordinate of the centre of each virtual pixel is then calculated and corresponds to the (x,y) position of the hit. Figure 3.8a shows a schematic representation of the reconstructed proton hit positions by considering all possible combinations of intersecting strips, and minimising the virtual pixel size.

3. Combine virtual pixels to form a “track”.

The virtual pixels reconstructed in Tracker 1 act as “seeds” for the tracking. The displacement in (x,y) between the virtual pixels in Tracker 2 are compared with one of the seeds in Tracker 1. The virtual pixel from Tracker 2 with minimal separation from the seed pixel is assigned to originate from the same proton. This process is then repeated, using the assigned virtual pixel in Tracker 2, to identify the corresponding virtual pixel in Tracker 3. This process is then similarly repeated from Tracker 3 to Tracker 4. The virtual pixels which are assigned together now form a track. If more than one proton passed through the system in a given frame, each seed is considered in turn with the remaining unassigned virtual pixels. Figure 3.8b shows schematically how this track reconstruction converges on complete tracks. The red dotted lines represent the consideration of the (x,y) separation between virtual pixels in neighbouring trackers.

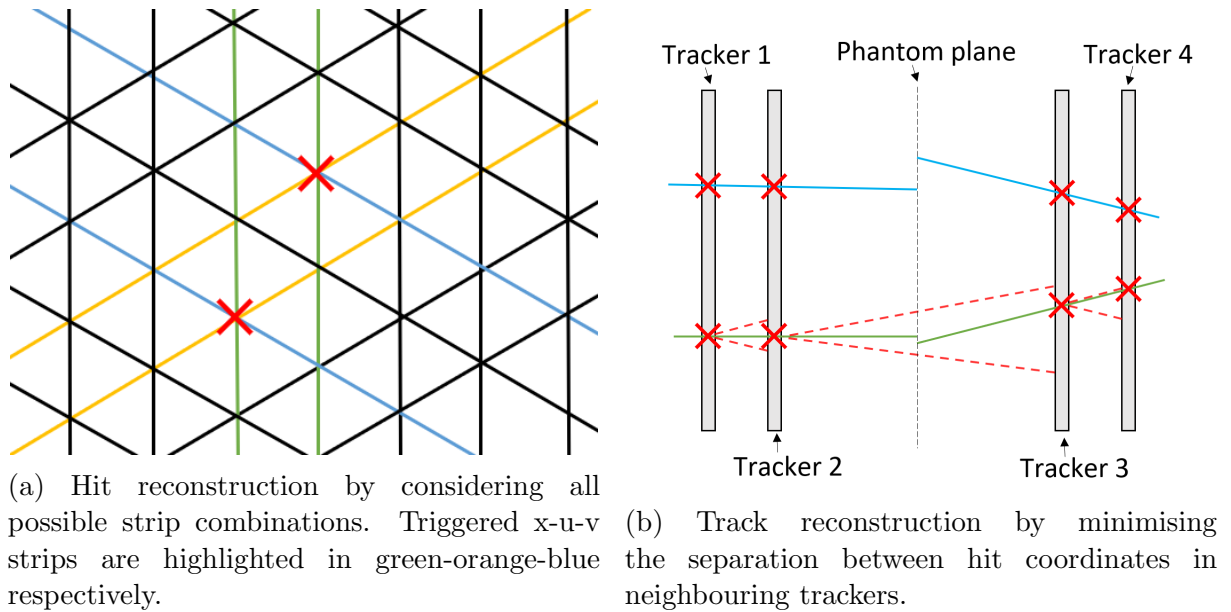


Figure 3.8: Diagrams representing the reconstruction of proton hits in a tracker and complete tracks through the PRaVDA trackers.

3.6.6 Super Simulation (SuSi)

The PRaVDA Super Simulation (SuSi) is a Geant4 [31] based Monte Carlo model of the PRaVDA system. Geant4 uses object oriented programming in C++ to model the passage of particles through matter. The framework allows for geometry handling, particle tracking, detector response, run management, and model visualisation. Geant4 has been used for simulation in high energy, nuclear, and accelerator physics, as well as in medical and space sciences. The development of SuSi using this framework therefore provided a powerful tool for the examination of detector concepts and the confirmation of experimental results.

SuSi has been developed to be a flexible model which includes macro based control of chosen beamline (Birmingham MC40 Cyclotron [73] or iThemba Labs [74]), detector systems, and phantoms. The layout of the system can therefore be easily manipulated and additional geometries added to the framework where required.

Geant4 allows for the selection of specific physics lists which describe the modelling

processes and interaction cross-sections. These physics lists are best selected based on the application area of the simulation model. Hadronic interactions are rare (occurring at a rate of $\sim 1\%$ per gcm^{-2} [28]) at the energy range relevant for proton therapy ($\sim 200\text{MeV}$ [26]). Their interactions contribute predominantly to the reduction in fluence of the beam and dose delivery within the phantom [28]. These interactions are therefore not critical for the purpose of proton tracking in proton CT. A specific physics list describing hadronic interactions was therefore not used in order to reduce computation times. Electromagnetic interactions were described using the `G4EmStandardPhysicsoption3` physics list which has been shown to be in good agreement with reference data [75] and recommended for medical applications [76]. Particle decays are described by the `G4DecayPhysics` and `G4RadioactiveDecayPhysics` physics lists.

A charge transport model was incorporated into SuSi for accurate modelling of charge transport and sharing across neighbouring strips. This model determined the number of charge carriers which would be produced in the silicon based on the total energy deposition of a traversing particle. The drift of these charge carriers within the silicon is then calculated to determine their contribution to the signal on each electrode. A strip is registered as being hit if the number of charge carriers (equivalent to the signal induced in the electronics connected to the strip if considering the physical system) is above a variable threshold (set within the simulation). The completeness of this charge sharing model allows for the accurate examination of the impact of changes to the system in terms of the reconstruction of 2D hit coordinates from multiple strip layers.

3.7 OPTIma

3.7.1 Overview

The Optimising Proton Therapy through Imaging (OPTIma) project includes academics and medical experts from the University of Birmingham, University of Manchester, University of Lincoln, The Christie NHS Foundation Trust and University Hospitals Birmingham. The main goal of the project is to build upon the work conducted throughout the PRaVDA project to develop a more clinically practical system able to perform proton Computed Tomography (pCT). This system would be able to perform in an environment with a scanning pencil beam treatment mode such as that at the new NHS facilities [24] [25].

3.7.2 Design Challenges

There are a series of challenges in designing such a device capable of performing in a clinical environment. One of the main difficulties of developing this system is the operational proton currents of the Varian machine at The Christie hospital. The operational frequency of the cyclotron is 72 MHz and can deliver a current to a minimum of 10pA on the research beam line where OPTIma will operate. This gives an average of 0.87 protons per clock cycle. This current is lower than the clinical system delivers to the treatment rooms, however, it is more suitable for individual proton tracking.

A Poisson distribution for the number of protons per cycle at the end of the research beam line is assumed and can be described by the relation

$$P(x; \lambda) = \frac{e^{-\lambda} \lambda^x}{x!} \text{ for } x = 0, 1, 2, \dots \text{ ,} \quad (3.12)$$

where x is the number of successes in a given trial and λ is the mean number of successes. $\lambda = 0.87$ for the case of 10pA at 72MHz. Such a distribution means that there will be some cycles which do not contain any protons, whilst others contain more than the ideal of 1. 1 proton per cycle is ideal as this means there are no ambiguous proton hit positions when using a silicon strip tracker. It is therefore important that the designed system should be able to perform with more than one proton in each cycle. The probabilities for the number of protons in each cycle assuming this Poisson distribution in Equation 3.12 is shown in Table 3.1.

Table 3.1: Probability of the number of protons in each cycle at The Christie [24] research room assuming a Poisson distribution.

$P(x = 0; \lambda = 0.87)$	0.419
$P(x = 1; \lambda = 0.87)$	0.364
$P(x = 2; \lambda = 0.87)$	0.159
$P(x = 3; \lambda = 0.87)$	0.046
$P(x \geq 4; \lambda = 0.87)$	0.012

Designing a system with adequate data rate capabilities to measure more than one proton before it is read out is difficult considering the high spatial density and rate of events in a clinical spot scanned beam.

The difficulty for the silicon strip trackers is the high spatial density of protons when there is more than one proton in a frame, as clinical spot scanned beams typically have a standard deviation for their profile in the range of 3-6mm [26]. The track reconstruction algorithm, described in Section 3.6.5, utilises the separation of events to identify the hits which originate from the same proton through the system. Multiple protons over a smaller area makes tracking in this manner more challenging, as the closest hit in the neighbouring tracker is not necessarily from the same proton. This inaccuracy in the tracking would then lead to increased uncertainties when performing full 3D reconstruction of a phantom. The impact of variations in the design of the strip sensors on the achievable resolution of the reconstructed proton position is discussed in detail in

Chapter 4.

The RERD faces similar challenges as for technology which can achieve the required readout rate and granularity. A range measuring RERD, which may provide the required granularity for individual proton tracking, requires many layers. Expectation for the number of layers is around 60 to 100 [33] in order to approach the limit due to range straggling (described in more detail in Section 3.5.1.2). Such a device is considered to be too large to be practical for mounting on a rotating gantry, based on the PRaVDA Range Telescope (described in Section 3.6.2). An energy measuring RERD faces the difficulty of separating individual protons in a frame, while still achieving a sufficient energy resolution. The work performed as described in the following chapters is an examination into a much more compact system in order to address this issue.

Chapter 4

Optimal Parameters for a Silicon Strip Tracker used for Proton Computed Tomography

4.1 Introduction

3D reconstruction in pCT requires that the trajectory of the protons as they enter and exit a patient are measured accurately. A proposed development to the PRaVDA system, discussed in Chapter 5, attempts to optimise the system for clinical practicality by replacing the Range Telescope with a single silicon pixel detector. This technique, called the Hybrid approach, does not require individual protons to be resolved. However, it does rely heavily on the ability of the trackers to be able to measure individual protons and reconstruct tracks at near 100% efficiency.

Chapter 6 proceeds in emphasising the value of the structural information of the phantom contained solely in the scattering. Incorporation of this information to enhance the final reconstructed image seems logical, and it is therefore critical to ensure the trackers of a pCT device perform optimally. Even more stringent requirements for the trackers

may be required if one were to consider a tracking only device, whether for full 3D reconstruction, or for the purpose of producing 2D radiographs.

The high proton current and development of clinical facilities towards spot scanning are pushing the limits of what tracking technologies used to date can accommodate. The x-u-v configured PRAVDA tracker [54], with its $90.8\mu\text{m}$ strip pitch and $150\mu\text{m}$ thickness, is at its limit of operation at such facilities. These limitations are discussed in the following sections.

This chapter describes the investigations made to optimise a tracking device capable of performing proton CT at The Christie Proton Therapy Centre in Manchester [24]. The main focus of these investigations was on optimising the strip pitch and silicon thickness of an x-u-v configured silicon strip tracker, based on the success of the PRAVDA device. The position resolution of a single silicon strip tracker, as well as the tracking resolution requiring two tracker units to project protons to a plane, were the parameters used to achieve this optimisation. These investigations were performed during the design phase of the OPTIma project [77] in order to propose a suitable device for this application.

These investigations to motivate the design of the OPTIma trackers were performed over the entire operational energy range of The Christie. The separation of the trackers was matched to that of the Hybrid system and scattering experiments to maintain the relevance of this work to these studies as well as to OPTIma's design.

A detailed discussion of the scattering theory is given in Chapter 6 to best accompany the results. The scattering theory, specifically in Section 6.2, may assist with understanding the verification of the resolution results to be described in this chapter.

4.2 Simulation Set-up

Figure 4.1 shows the set-up used in this simulation. Simulations, using SuSi (introduced in Section 3.6.6), were run with no phantom in place to model the set-up as a best case scenario which had minimal scatter. This meant that any tracker parameters insufficient for delivering a suitable performance in this best case scenario, would not be able to suitably perform in experiments with the additional scattering arising from the increased separation and large phantom (i.e. a head phantom).

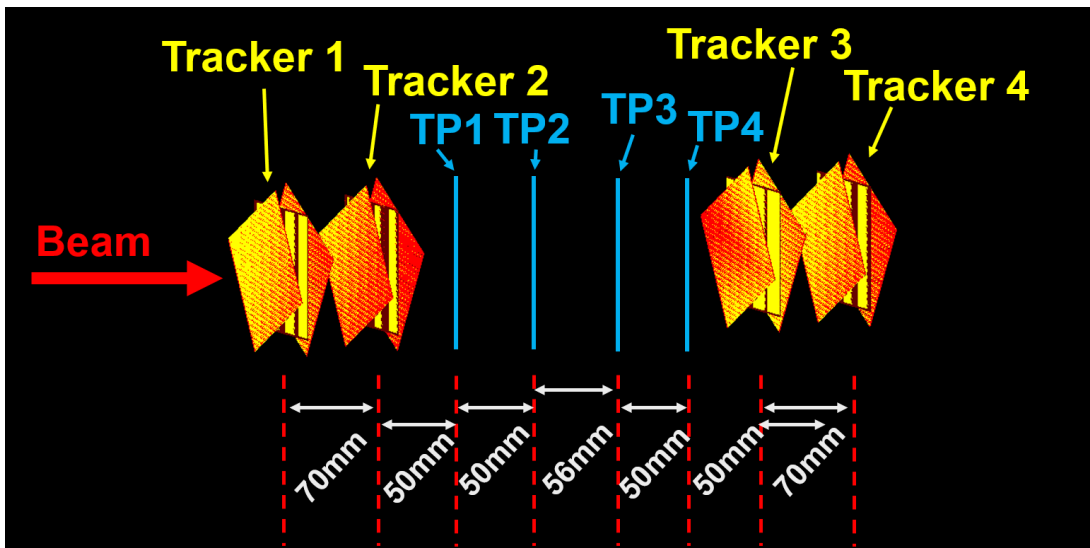


Figure 4.1: The simulation set-up used for the studies to optimise strip pitch and silicon thickness. TP refers to the Truth Planes.

A uniform, 5cm diameter, mono-energetic beam of protons, ranging from 36MeV to 245MeV in 1MeV steps was simulated. This covered the entire workable range at The Christie (75-245MeV) [24], and also went down to the 36MeV of the Birmingham MC40 cyclotron. Separation of the tracker units (each consisting of three sensors) was set to the minimum of 70mm of the physical PRAVDA devices.

Truth planes, which measured the true position of protons in the simulation, were placed 50mm and 100mm behind Tracker 2, and 50mm and 100mm in front of Tracker 3. These planes were positioned in order to evaluate the difference between the

reconstructed proton position at the plane and its true position. The reconstructed proton hit positions were calculated using the ROSETA algorithm previously outlined in Section 3.6.5. An in depth discussion of the simulation model is described in Chapter 5.

4.3 Analysis Method

The aim of this analysis was to aid in the determination of a suitable silicon strip pitch and thickness in order to design a tracker with sufficient accuracy in reconstruction to perform pCT by OPTIma. The parameters considered for the optimisation were the position and tracking resolutions. The position resolution defines the accuracy of a single tracker unit in reconstructing a proton hit coordinate through the central silicon layer (u-layer). The tracking resolution similarly defines the accuracy of a reconstructed position of a proton by projecting a track using two tracker units onto a plane. The tracking resolution is specifically important as protons are required to be projected onto the phantom for 3D reconstruction. The tracking resolution is also critical if considering the Hybrid approach, as track projection onto the pixel plane is required for proton counting and averaging. Poor tracking resolution in a Hybrid approach would therefore result in a poor entry/exit position on the phantom, and also a poor WEPL measurement.

Simulation of the trackers was conducted with $50\mu\text{m}$, $90.8\mu\text{m}$ and $200\mu\text{m}$ silicon pitch; each at a sensor thickness of $100\mu\text{m}$ and $150\mu\text{m}$. The tracker was maintained with an x-u-v configuration due to the requirement of being able to perform with a high proton current at The Christie. This configuration had been proven to better reconstruct multiple protons with minimal ambiguities [54]. The simulated data was then run through the ROSETA reconstruction software to reconstruct hit positions for all protons in each tracker unit.

The simulation was designed to output the true proton hit position as it traversed each tracker unit and through the specified truth planes. This allowed for the comparison between the reconstructed proton positions and the true hit position as outputted from the simulation. The difference between the true and reconstructed proton position in the x and y dimensions (plane perpendicular to the beam direction), $\Delta(x, y)$, was determined and plotted in histograms such that

$$\Delta(x, y) = R(x, y) - T(x, y) \quad , \quad (4.1)$$

where $R(x, y)$ and $T(x, y)$ are the reconstructed and true hit positions respectively. Figure 4.2 shows the relation between the reconstructed and true proton positions on a plane.

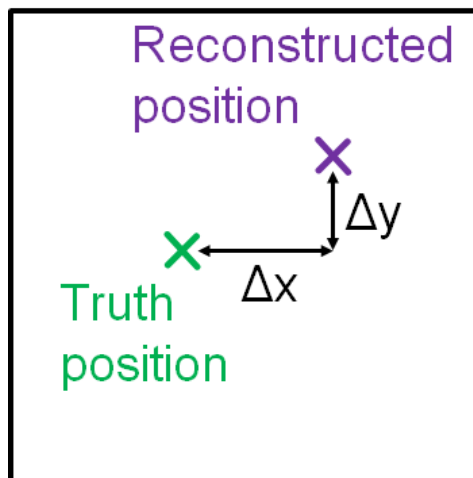
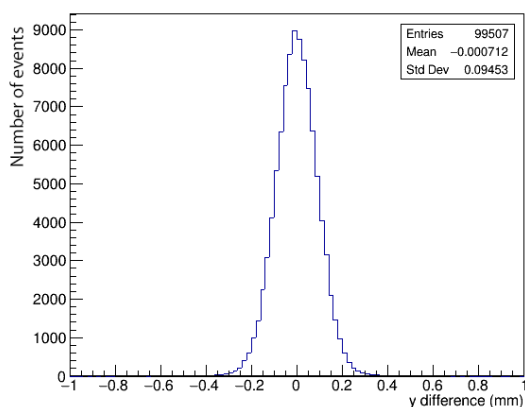


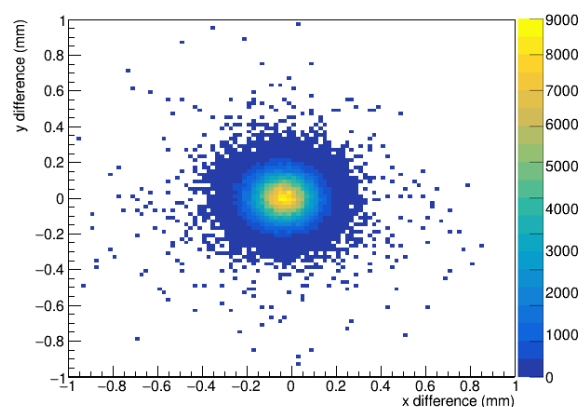
Figure 4.2: A schematic representation of the separation between the reconstructed and true proton positions through a plane.

The parameters, Δx and Δy , when plotted in histograms, allow the determination of a resolution from the standard deviation. The reconstructed position within a single tracker unit was outputted from the ROSETA algorithm and could be compared with the true proton position in the u-plane from the simulation. The standard deviation of this distribution gave a measure of the position resolution. The reconstructed hit positions in

Trackers 1 and 2 were then used to project a track to Truth Planes 1 and 2. Similarly, reconstructed positions in Trackers 3 and 4 were used to back project tracks to Truth Planes 3 and 4. The standard deviation of the separation between the projected proton position and the true position gives a measure of the tracking resolution. Figures 4.3a and 4.3b show the 1D distribution of Δy and the 2D distribution of $\Delta(x, y)$ respectively as an example of the procedure.



(a) Δy .



(b) $\Delta(x, y)$.

Figure 4.3: 1D and 2D distributions of the difference between the reconstructed and true position of a proton on a plane. Reconstruction at a tracker’s u-plane gives the position resolution, and reconstruction at a truth plane after track projection gives the tracking resolution.

4.4 Results

The results for all strip pitch and silicon thickness configurations can be summarised on a single plot for a given plane. Emphasis was placed on the most extreme cases, which were the position resolutions of Trackers 1 and 4, and the tracking resolutions of Truth Planes 2 and 3. Tracker 1 included protons which had undergone minimal scatter, and therefore gave the best achievable position resolution in this configuration. Tracker 4 was the furthest tracker from where the beam was produced, and so included more scatter, therefore giving a worsened position resolution. Similarly, the Truth Planes furthest from

the measured proton positions in the trackers would have the largest uncertainty after track projection. Truth Planes 2 and 3 were therefore used for the main consideration of suitable parameters, as Truth Plane 2 was furthest from Trackers 1 and 2, and Truth Plane 3 was furthest from Trackers 3 and 4. Truth Planes 1 and 4 were also considered closely for verification of the results.

The position resolution as a function of energy for Trackers 1 and 4 are shown in Figures 4.4 and 4.5 respectively. The tracking resolution as a function of energy for projected tracks to Truth Planes 1, 2, 3 and 4 are shown in Figures 4.6, 4.7, 4.8 and 4.9 respectively.

4.5 Discussion

4.5.1 Position Resolution

The achievable position resolution in Tracker 1, shown in Figure 4.4, for all proton energies, appears to be worse for the $200\mu\text{m}$ pitch in both $100\mu\text{m}$ and $150\mu\text{m}$ thicknesses in comparison to the smaller pitches. The position resolution improves when moving from $200\mu\text{m}$ to $90.8\mu\text{m}$ pitch, which was used in the PRaVDA trackers. A further, but less significant improvement is seen by moving to a $50\mu\text{m}$ pitch.

The results of the position resolution when considering Tracker 4, in Figure 4.5, differ more significantly. There is a general worsening of the position resolution in comparison to Tracker 1, especially at lower energies, because of the additional scatter occurring to the protons as they travel through the system. At higher energies, where the protons scatter less, the resultant position resolutions converge on the same values as they do for Tracker 1.

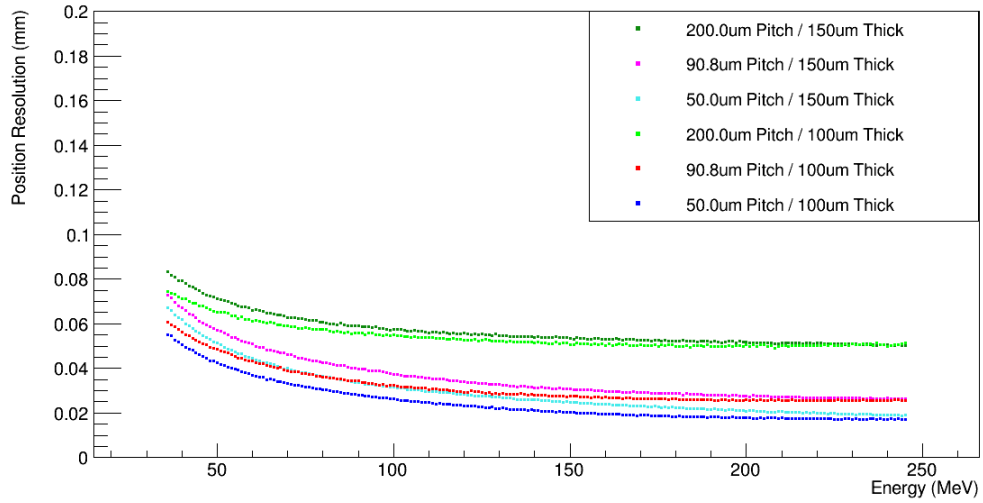


Figure 4.4: The position resolution as a function of incident proton energy for protons reconstructed in Tracker 1.

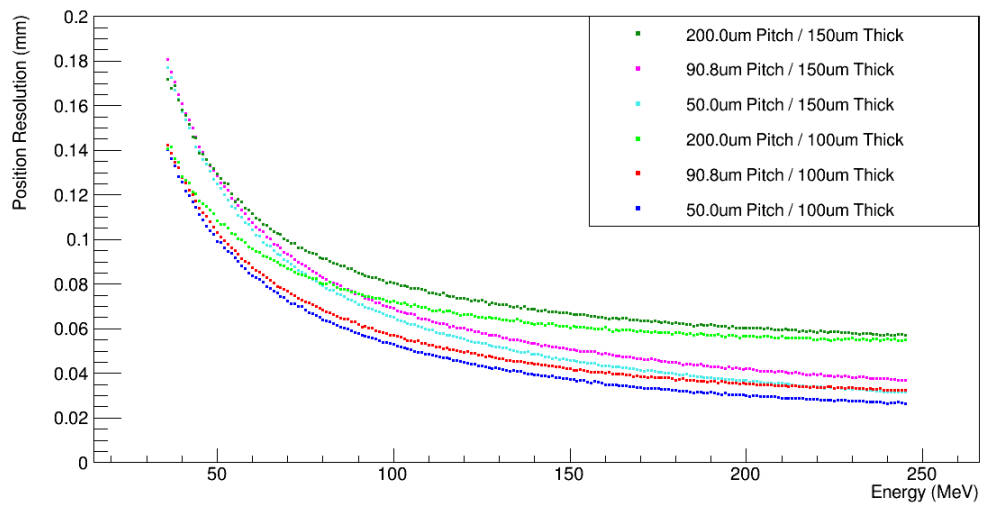


Figure 4.5: The position resolution as a function of incident proton energy for protons reconstructed in Tracker 4.

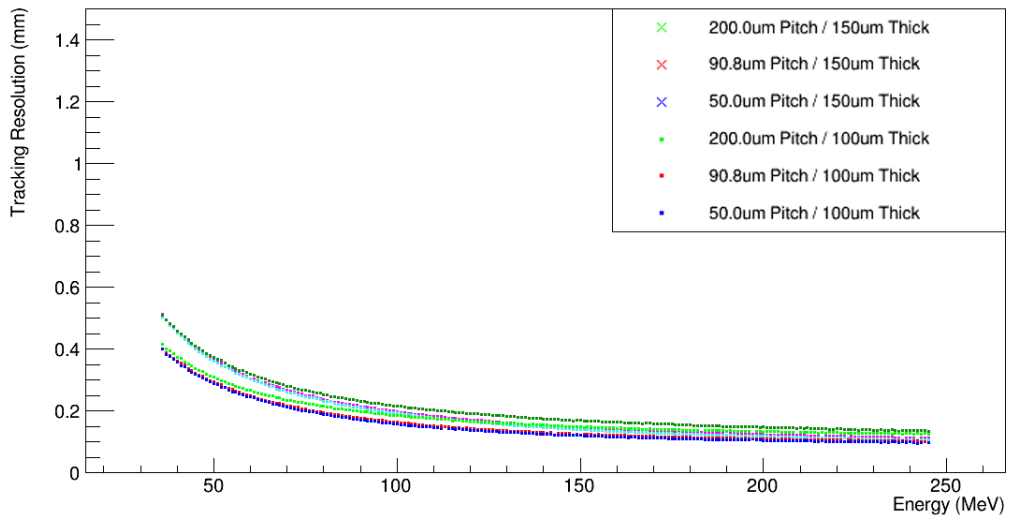


Figure 4.6: The tracking resolution as a function of incident proton energy for protons projected to Truth Plane 1 using reconstructed hit positions in Trackers 1 and 2.

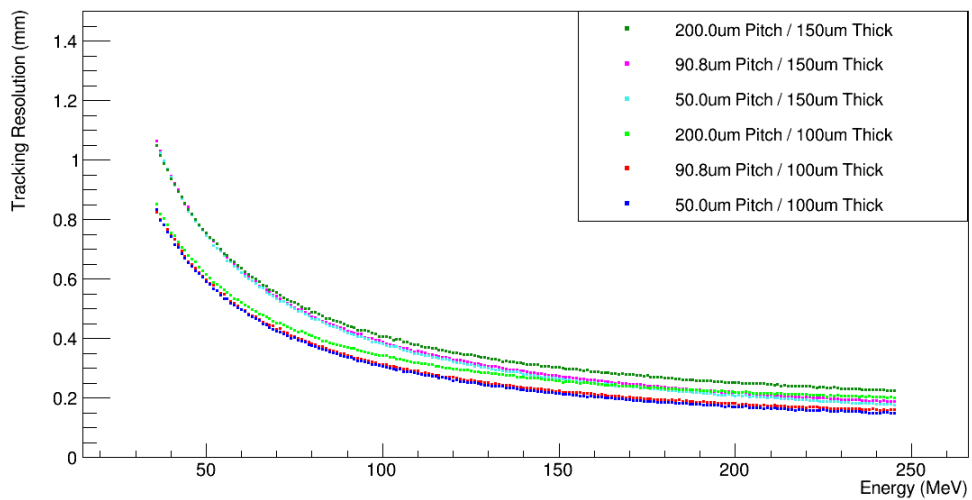


Figure 4.7: The tracking resolution as a function of incident proton energy for protons projected to Truth Plane 2 using reconstructed hit positions in Trackers 1 and 2.

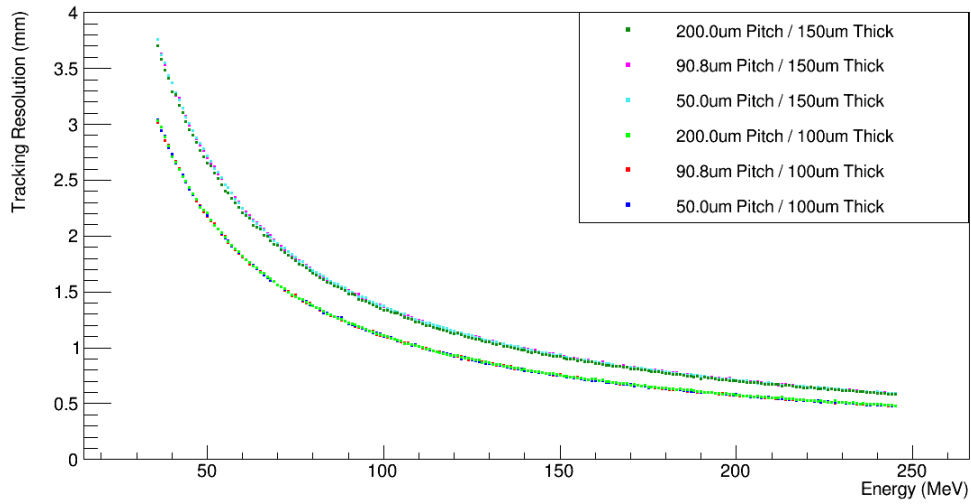


Figure 4.8: The tracking resolution as a function of incident proton energy for protons projected to Truth Plane 3 using reconstructed hit positions in Trackers 3 and 4. Note that the y-axis range differs from Figures 4.6 and 4.7 for clarity of the results.

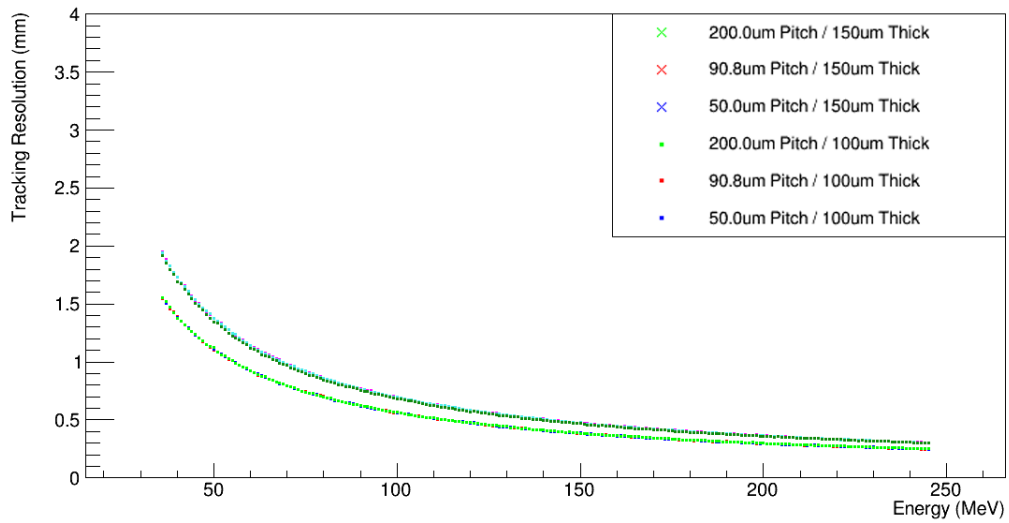


Figure 4.9: The tracking resolution as a function of incident proton energy for protons projected to Truth Plane 4 using reconstructed hit positions in Trackers 3 and 4. Note that the y-axis range differs from Figures 4.6 and 4.7 for clarity of the results.

The convergence of the position resolutions at higher proton energies is because the trackers are tending to their theoretical optimal values. The optimal resolution for a single layer of silicon strips with binary readout is $\frac{p}{\sqrt{12}}$, as described in Equation 2.8, where p is the strip pitch. This means the position resolutions, when considering a single layer of strips (e.g. segmented in the x-axis), should converge on $14.4\mu\text{m}$, $26.2\mu\text{m}$, and $57.7\mu\text{m}$, for $50\mu\text{m}$, $90.8\mu\text{m}$, and $200\mu\text{m}$ strip pitches respectively. These optimal values are only approached as the amount of scatter reduces with the higher proton energies. The convergence to these values is confirmation of the behaviour of the position resolution results at higher proton energies.

Most notably, at lower proton energies, the position resolution in Tracker 4 does not appear to differ between pitches. The main improvement at these energies is achieved by reducing the silicon thickness from $150\mu\text{m}$ to $100\mu\text{m}$. This convergence of the position resolutions towards the same values, irrespective of strip pitch, is due to the scattering, internal geometry of the tracker units, and the reconstruction algorithm. Each silicon strip layer is separated by 12mm within a tracker, meaning a distance of 24mm is present between the x and v (first and last) planes. A proton which enters at an angle of 0.5° to the tracker therefore travels $200\mu\text{m}$ laterally over this 24mm distance. Scatter which occurs at proton energies of 36MeV would cause the protons to approach angles such as this while traversing the system. Detailed discussion of the impact of this scattering is given in Chapter 6, and typical standard deviations of the plane projected scattering angle are shown in Figure 6.10. The reconstruction algorithm, described in Section 3.6.5, relies on the formation of “virtual” pixels to reconstruct a coordinate. These virtual pixels increase in size with an increase in the lateral displacement of the proton between layers within a tracker. Protons which traverse the tracker at 0.5° or more therefore have no improvement to the virtual pixel size, as a consequence of the lateral displacement, irrespective of the strip pitch.

The uncertainty on the reconstructed position at the central u-plane of a tracker is influenced by the amount of scatter occurring in the preceding x-plane. Increased scattering caused by additional silicon is therefore going to worsen the uncertainty on the reconstructed position. The correlation between these uncertainties can be understood by considering the arc length of a circle, which follows the relation

$$\delta x = z \delta \theta \quad , \quad (4.2)$$

where δx is the uncertainty on the arc length, z is the radius of the arc, and $\delta \theta$ is the uncertainty on the angle. The uncertainty on the plane projected scattering angle has a square root dependence on the traversed material thickness (described in detail in Section 6.2). The ratio of the uncertainties on the proton position after traversing the first layer of a tracker unit between the case of $150\mu\text{m}$ thickness and $100\mu\text{m}$ thickness silicon is then given by

$$\frac{\delta x_{150}}{\delta x_{100}} = \frac{z \delta \theta_{150}}{z \delta \theta_{100}} = \frac{\sqrt{150}}{\sqrt{100}} = 1.225 \quad . \quad (4.3)$$

z is the same for both cases as it is based on the geometry of the tracker. This 1.225 factor between the position resolution from $150\mu\text{m}$ thickness compared with $100\mu\text{m}$ thickness can be seen in both Figures 4.4 and 4.5, which confirms the behaviour at low energy, and that the scatter in the silicon is dominating the uncertainty.

4.5.2 Tracking Resolution

The tracking resolution is fundamentally affected by the uncertainty in the measured position of the protons at the trackers. The scattering occurring at lower proton energies, which negated any improvement through reduction in pitch (seen in Figure 4.5), is also

observed in the tracking resolution at Truth Plane 2. The energy range over which there is little improvement by reducing the pitch, is extended further than that observed in Figure 4.5. At the highest energies, there is minimal improvement (approximately $50\mu\text{m}$) in the tracking resolution by reducing the pitch.

Truth Plane 3 is the plane with the largest uncertainty because it is affected by the reconstructed positions in Trackers 3 and 4, where protons have undergone the largest amount of scatter. The y-axis in Figure 4.8 has therefore been extended in comparison to Figure 4.7 to include all the data. It can be seen from Figure 4.8 that there appears to be no improvement in the tracking resolution at Truth Plane 3 by reducing the pitch. The increased pitch of $200\mu\text{m}$, in comparison to the $90.8\mu\text{m}$ of the PRaVDA trackers, still appears to be at no detriment to the achievable tracking resolution. The only improvement to the tracking resolution, across the entire energy range, appears to be from the reduction in thickness of silicon from $150\mu\text{m}$ to $100\mu\text{m}$.

The behaviour of the results for the tracking resolution is additionally verified through a further consideration of Equation 4.2. The ratio between the uncertainties at Truth Plane 2 and Truth Plane 1 (and similarly Truth Plane 3 and Truth Plane 4) is given by

$$\frac{\delta x_{TP2}}{\delta x_{TP1}} = \frac{100 \delta\theta}{50 \delta\theta} = 2 \quad , \quad (4.4)$$

where $\delta\theta$ is the same for both Truth Planes, as it is measured at the position of the trackers. This factor of 2 between the values observed in Figures 4.7 and 4.6 (and similarly Figures 4.8 and 4.9) is evident, giving additional confirmation of the behaviour of the results. This result also highlights the importance of minimising the distance of the projection, so the trackers should be positioned as close to the phantom as possible for the most accurate results.

4.6 Conclusions

Investigations using simulation were performed to examine the impact on the achievable position and tracking resolutions of x-u-v configured silicon strip trackers for pCT. These studies were critical during the design stage of the OPTIma project to guide the design of a suitably performing tracker to be used on the research beamline at The Christie proton facility.

The studies showed that improvements were possible in the achievable position resolution over a large proportion of the energy range by reducing the strip pitch. A reduction in the silicon thickness also led to an improvement in the position resolution, most significantly in the lower energy range where scattering within the silicon becomes more prominent.

The tracking resolution is important for the projection of the reconstructed proton positions in the trackers onto the phantom when performing pCT. It was found that a reduction in pitch of the distal trackers (Trackers 3 and 4) showed no improvement at either $150\mu\text{m}$ or $100\mu\text{m}$ thickness. The proximal trackers (Trackers 1 and 2), at higher energy, showed a small improvement by reducing pitch, but of little significance.

The main and consistent improvement appeared to be in the reduction in thickness of silicon from $150\mu\text{m}$ (used in PRaVDA) to $100\mu\text{m}$. This improvement was confirmed to be a result of the reduction in scatter caused by the reduction in silicon traversed by the protons. The improvement was most apparent at lower energy, where the rate of interaction is highest. However, although testing would likely be performed on the Birmingham MC40 cyclotron, OPTIma's design focus was for a clinical facility, which operates at high energy. The improvement in the tracking resolution by moving from $150\mu\text{m}$ to $100\mu\text{m}$ thickness is less significant in this regime, even after further energy degradation within a patient. The higher proton energy also means that less charge would be deposited in the silicon over a given thickness, in accordance with the

Bethe-Bloch formula (Equation 1.7). Reducing the silicon thickness, in combination with the reduced stopping power at higher proton energy, means less charge generation in the silicon. This means there would be increasingly stringent requirements on the electronics having low noise and sufficient charge collection efficiency to operate effectively.

Other impacting factors relating to the practical operation of the OPTIma device also required consideration for the tracker design in addition to these results. A reduction in strip pitch from the $90.8\mu\text{m}$ of PRaVDA to $50\mu\text{m}$ may offer a small improvement in resolution. However, it also almost doubles the amount of data requiring processing by the electronics due to the increased number of channels. This becomes of particular concern when operating at a clinical facility which uses high currents (discussed in more detail in Section 3.7.2). This increased data rate originating from the higher current was the motivation for examining the potential for an increased strip pitch to $200\mu\text{m}$ in comparison to PRaVDA's $90.8\mu\text{m}$. The practicality of faster data processing, with only a small worsening of tracking resolution in the proximal trackers, meant the $200\mu\text{m}$ pitch was a favourable option.

Cost minimisation was an additional consideration for the OPTIma project, and for the outlook towards clinical practicality, as a minimal cost is required in order for such a system to be adopted for routine use. A reduction in silicon thickness increases the manufacturing costs of the silicon. This cost impact, with the limited improvement in the tracking resolution by moving from $150\mu\text{m}$ to $100\mu\text{m}$ thickness, did not seem sufficient to motivate the change.

The final silicon strip parameters of choice for the design of OPTIma were $200\mu\text{m}$ pitch and $150\mu\text{m}$ thickness.

Chapter 5

Investigation of a Novel Hybrid System for Proton Computed Tomography

5.1 Introduction

The motivation for developing a proton CT system is for it to improve the clinical outcome of a proton therapy treatment. These improvements can include reduced complications for a patient, increased life expectancy, or a higher probability of completely eradicating the tumour. Such a system must be suitable for a clinical setting to achieve these goals.

The system developed by the PRaVDA consortium used a Range Telescope for the measurement of the residual energy of the protons. The device was developed for the iThemba labs beam which ran clinically at 191MeV. This Range Telescope, shown in Figure 3.3, was very large and heavy, as it comprised 22 silicon tracking layers, Perspex absorbers, associated readout electronics and structural supports. The clinical energy range of the protons at The Christie hospital in Manchester is 75-245MeV. For such energies, provisional studies performed by the OPTIma group suggest a Range Telescope

would have to have approximately 60-80 silicon layers in order to measure every proton over the complete range of energies. Given that the PRaVDA Range Telescope was on the bounds of clinical usefulness due to its size and weight - a much larger one would be unrealistic for clinical use.

The success and suitability of the silicon strip trackers used in PRaVDA for reconstructing the proton paths retain their clinical relevance. An alternative method for measuring the residual energy of the protons after passing through the patient requires development. Investigation into a proposed solution is outlined in this Chapter. The solution involves replacing the entire Range Telescope with a single layer silicon pixel detector. The combined use of silicon strip and silicon pixel technology for the pCT system is the source of its “Hybrid Approach” name.

The pixel devices used in this investigation outputted a digitised measure of the analogue signal (outlined in Section 2.4) generated in each pixel by the interacting protons. This signal is in units of Digital Number (DN), but does not directly measure the energy of the interacting proton in the detector. The relation of this signal to the incident proton energy can be derived from the Bragg-Kleeman rule. Rearranging Equation 1.9 for the energy, E , as a function of distance through the material, z , gives the relation

$$E(z) = \alpha^{-\frac{1}{p}}(R_0 - z)^{\frac{1}{p}} \quad , \quad (5.1)$$

where R_0 is the protons’ maximum range through the material [34], and α and p are experimentally determined parameters [34]. The stopping power can then be determined by differentiating this relation giving [34]

$$-\frac{dE}{dz} = p^{-1}\alpha^{-\frac{1}{p}}(R_0 - z)^{\frac{1}{p}-1} \quad . \quad (5.2)$$

This relation defines the stopping power of the material after the proton has traversed a given thickness of the material, z . This material thickness, in terms of a Water Equivalent Path Length (WEPL) of each voxel within the phantom, is the parameter of interest for pCT.

The stopping power, and equivalently signal, S , from the detector can then be related to the proton energy when it reaches the detector through the combination of Equations 5.1 and 5.2 giving

$$-\frac{dE}{dz} \propto S \propto \frac{E(z)}{p(R_0 - z)} . \quad (5.3)$$

The Hybrid approach uses the signal from the pixel sensor as a measure of the WEPL of the path the proton took through the phantom. A calibration curve which relates these parameters according to Equation 5.2 is used for this measurement. Suitable data for this curve is obtained for each specific system configuration using a series of Perspex sheets with different thicknesses to vary the signal in the pixel sensor.

The stochastic nature of energy loss within the silicon means that determination of the WEPL from the signal generated by an individual proton is not accurate. An averaging technique was therefore adopted which resolves this issue by using the increased statistics from many protons to measure of the signal more accurately. The averaging would also account for the difference in the WEPL of protons traversing a given pixel from different paths through the phantom. This technique is described further in the following sections. The use of an averaging technique meant that silicon MAPS technology was suitable, despite not being able to distinguish between individual protons due to limitations in the readout rate. The use of MAPS meant that the detector would be very thin, having limited impact on energy degradation/scattering, and be clinically practical.

This proposed system was simulated using Geant4 and investigated experimentally in two differing configurations. Both of these configurations are outlined and the difference in their procedure/analysis discussed.

5.2 System Set-up

Initial investigations began with the study of the proposed solution using simulation. A flexible Geant4 simulation model called PRAVDA's Super Simulation (SuSi) was developed during the work on PRAVDA. This model has been verified with measurements on both the Birmingham and iThemba beamlines [78]. A representation of the general layout of the Hybrid system is shown in Figure 5.1. Precise separations of components were dependent on the specific investigation being performed. The spatial ordering of the components remained constant. Experimental investigations on the Birmingham MC40 cyclotron were then performed. This section describes the general system set-up along with the devices and phantoms used in both simulation and experiment.

The general system layout shown in Figure 5.1 involved beam set-up structures, two proximal tracker units (Trackers 1 and 2), phantom or calibration objects, pixel sensor, and two distal trackers (Trackers 3 and 4).

5.2.1 Beam Set-up

Proton therapy centres were predominantly focused on delivering broad beams of protons during the development phase of the PRAVDA system. The iThemba Labs treatment facility, which the PRAVDA project was specifically designed for, is an example of a facility delivering broad beams. The beam was then degraded by a compensator to

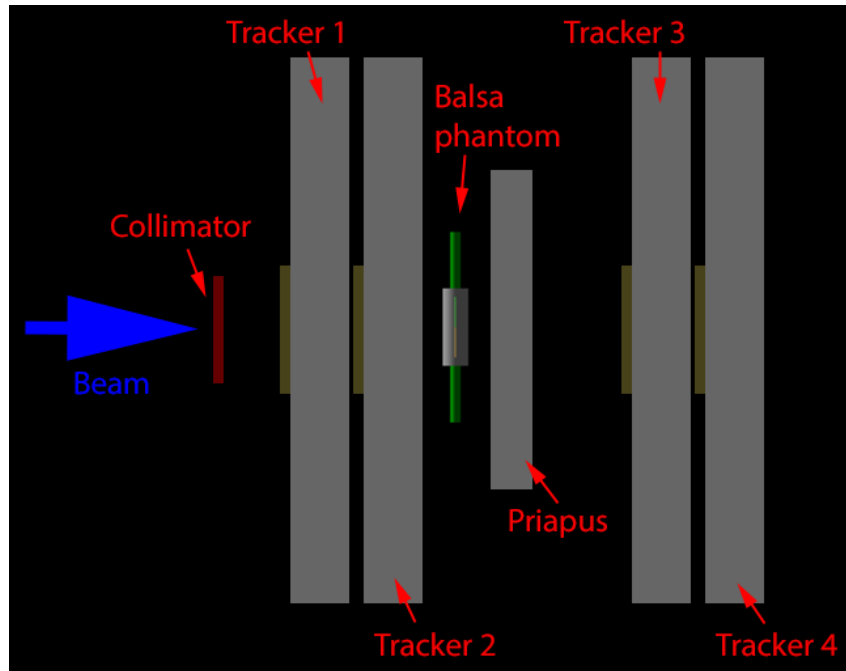


Figure 5.1: Set-up of the PRaVDA Hybrid system on the Birmingham beamline.

achieve a conformal dose to the tumour. The MC40 cyclotron at the University of Birmingham also provided a broad beam for sample irradiation and system testing, but at too low an energy for clinical use. More recent developments of proton therapy have involved focusing on spot scanned beams which can be accurately directed in the beam delivery nozzle. All experiments of the Hybrid approach were performed at the MC40 cyclotron where it was not possible to deliver actively scanned spots of protons. A movable collimator was therefore constructed to collimate the broad beam to be of a comparable spot size to that at a clinical facility. The Hybrid investigations were performed with both a broad beam and a pseudo-spot scanned beam to demonstrate suitability with both delivery methods.

5.2.1.1 Broad Beam

The broad beam of the Birmingham MC40 cyclotron is a uniformly distributed circular beam of protons with a 5cm diameter. A 36.45 ± 0.15 MeV proton energy was used in simulation as this has been previously used to match SuSi with data taken on the

cyclotron. A measured divergence of the beam of 1.6 mrad was also included in the simulation.

5.2.1.2 Moving Collimator

A moving collimator was developed to mimic a spot scanned facility as this study aimed for clinical relevance. This beam is referred to as a pseudo-spot beam as it did not directly replicate how a clinical spot beam performs. A diagram of the collimator modelled in Geant4 is shown in Figure 5.2.

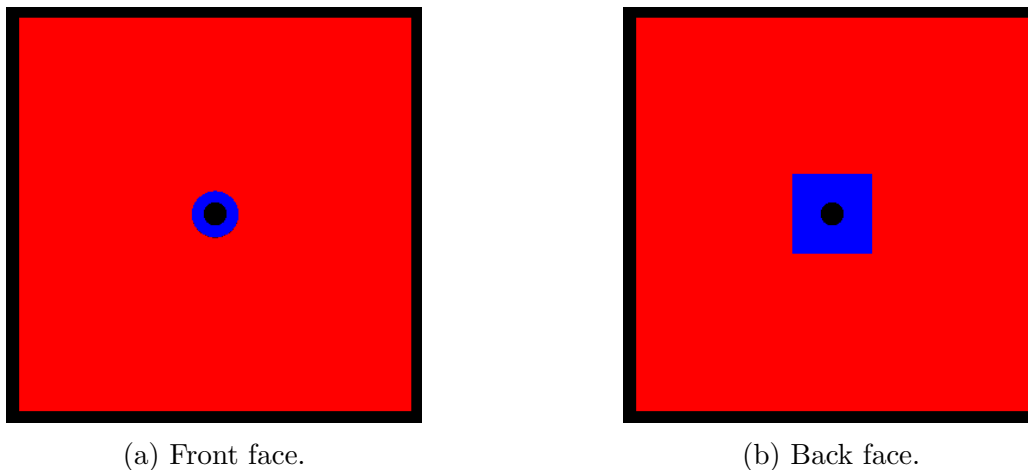


Figure 5.2: Geant4 model of a moving collimator with a 6mm aperture. Red represents aluminium and blue represents tantalum.

The Christie hospital runs with a Gaussian distributed spot scanned beam of $\sigma = 3.2\text{mm}$. The collimator for our system was therefore designed with a 6mm diameter aperture. The main body of the collimator was $10\text{cm} \times 10\text{cm}$ square and had a thickness of 1cm to ensure the entire beam was covered for all possible collimator positions. The red region in Figure 5.2 represents aluminium and the blue region represents tantalum. The tantalum was a smaller $2\text{cm} \times 2\text{cm}$ square plate of 2mm thickness and was inserted into the back face of the collimator. Tantalum, due to its higher density, meant that the protons could be attenuated over a shorter distance. This therefore reduced the potential for scatter

from the edges of the collimator. The protons outside of the 6mm region of interest would be attenuated through a thicker amount of aluminium. The use of aluminium in this outer region reduced the cost of the collimator design. The hole in the aluminium was made larger than the tantalum aperture to reduce any scattering effects of protons which pass through the tantalum aperture.

The entire collimator was mounted on a 2D moving stage which could move the aperture over the entire 5cm diameter beam area to imitate a spot scan.

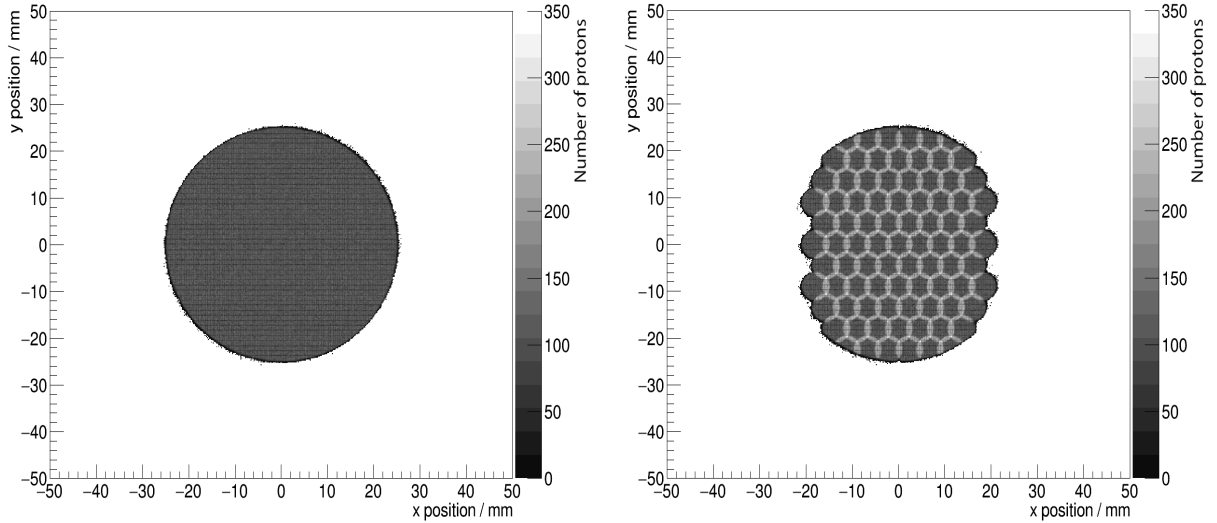
5.2.1.3 Beam Distributions

Figure 5.3 shows the distribution of protons reconstructed in the first tracker unit using simulation. Each simulation was run with 5 million protons in a broad beam centred on (0,0). The presence of the collimator for the pseudo-spot scan meant that many protons were stopped before reaching the trackers. Though computing intensive, it ensured that any variations in proton density of the broad beam at the edges were accounted for in the simulation to best match the experimental data.

5.2.2 Trackers

The tracker units used for this investigation were the PRaVDA trackers. The structure of these trackers is described in detail in Section 3.6.1.

The total size, pitch, thickness, and orientation of the silicon was modelled in SuSi for simulation. The simulation had additional structural details of the physical trackers included such as PCBs, aluminium stiffeners, ASICs and tracker casings. This allowed for accurate modelling of the interaction of protons through the system.



(a) Broad beam proton distribution.

(b) Pseudo-spot beam proton distribution.

Figure 5.3: Distribution of protons in a broad and a pseudo-spot scanned beam on the Birmingham MC40 cyclotron.

5.2.3 Phantoms

5.2.3.1 Balsa Wood Phantom

It is only possible for the 36MeV protons from the Birmingham MC40 cyclotron to pass through approximately 15mm of water before they stop. This short range made it impossible to image a phantom with an approximate size of a human head. A small and low density phantom was instead manufactured in order to allow these protons to pass all the way through the imaging object. The Geant4 model of this phantom is shown in Figure 5.4.

The main cylindrical body of the phantom was manufactured in balsa wood as this is a low density material. The cylinder was manufactured with a 25mm diameter circular face and a height of 75mm. A 2mm hole was drilled through the centre of the cylinder, from one circular face to the other. A 2mm diameter cylindrical rod of Perspex, with a length of 29.5mm, was inserted into one end of the hole. The other half of the hole had nothing inserted so it acted as an air void. Two Perspex rods were then attached to either end of the cylinder in order to mount and rotate the phantom during imaging.

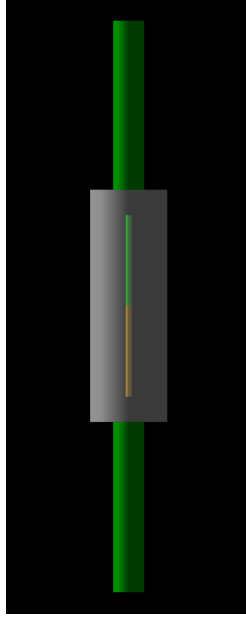


Figure 5.4: The balsa wood phantom. Green represents Perspex, orange represents air and white represents balsa wood.

The G4_PLEXIGLASS and G4_AIR NIST materials [79], with densities of 1.19 gcm^{-3} and $0.00120479 \text{ gcm}^{-3}$ respectively, were used to model the Perspex and air inserts in SuSi. A standard balsa wood material was not predefined in Geant4 and so a new material was constructed. This material was specified to be a hydrocarbon with a structure of C_2OH_4 . This was chosen upon consideration of the main constituents of wood being cellulose and lignin [80] with chemical compositions of $\text{C}_6\text{H}_{10}\text{O}_5$ [81] and $\text{C}_{81}\text{H}_{92}\text{O}_{28}$ [82] respectively. C_2OH_4 was therefore chosen according to the relative elemental proportions by atomic mass of these two predominant constituents. The growth of wood is not homogeneous and so the chemical composition and density of wood can vary largely between species [80] and individual plants. A medium density balsa wood was therefore chosen for the simulation studies with density of 0.16 gcm^{-3} [83]. This value of the density was later confirmed to be appropriate for the wood used to construct the phantom for experiment.

The symmetry of this phantom was chosen such that the number of projections required

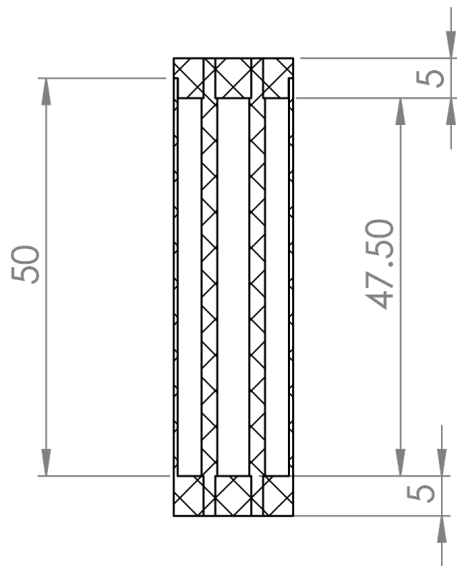
to reconstruct an image could be reduced. The reduction in time to take data for an image was important for the Birmingham MC40 cyclotron as the pseudo-spot scan took much longer to complete than a typical spot scanning system at a hospital. The requirement of 85 spot positions for each projection meant that conducting 180 projections for a full CT image was impractical in the time available. The active spot scanning speed of the clinical system at The Christie is a much faster 10 ms^{-1} , in comparison to the order of minutes for the pseudo-spot system at Birmingham. This means the entire scanned area for a single projection could be covered in the order of a second for a clinical proton facility.

5.2.3.2 Perspex Phantom

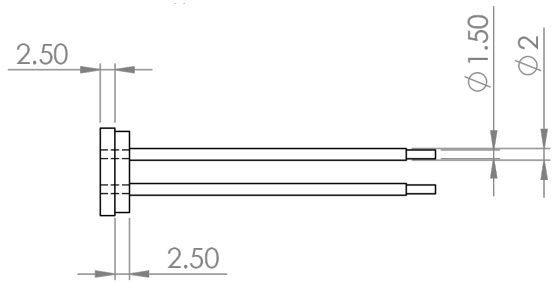
A second phantom was developed for the second experimental investigation. The schematic diagram of this phantom is shown in Figure 5.5.

The phantom was a hollow Perspex cylinder with an outer diameter of 15mm and an overall height of 57.5mm. The walls of the cylinder were milled to be $500\mu\text{m}$ thick and the remaining volume contained air. Two 2mm cylindrical Perspex inserts were positioned within the phantom at a distance of 6mm apart. The phantom was designed in this way such that the maximum proton path length through the phantom was 5.4mm of Perspex (6.3mm water).

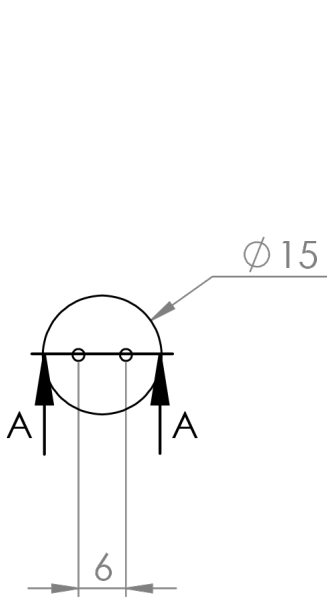
The off-centre inserts of the Perspex phantom meant that different projections would yield different results. This was unlike the 360° symmetry of the balsa wood phantom, meaning for that case, all projections should be the same. Only the broad beam was used to examine this phantom due to the length of time required to conduct a spot scan on the Birmingham MC40 cyclotron. Multiple projections of the Perspex phantom meant that 3D reconstruction could be performed.



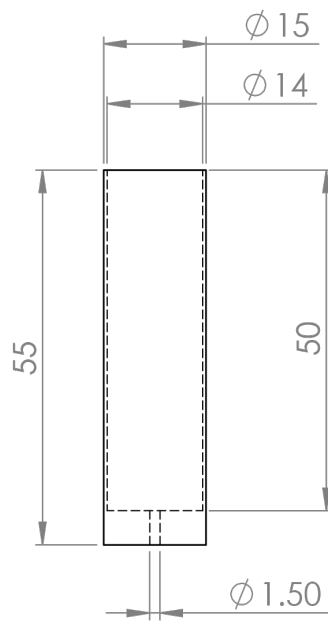
(a) Phantom cross section.



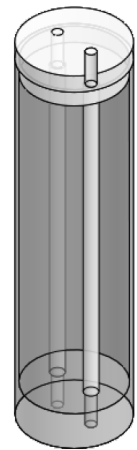
(b) Phantom inserts.



(c) Phantom top.



(d) Phantom wall.



(e) Phantom in 3D.

Figure 5.5: Schematic diagrams of the hollow Perspex phantom.

5.2.3.3 Calibration Arms

The first iteration of the experiment using the balsa wood phantom used Perspex sheets in order to cover the entire 5cm diameter proton beam. Entire coverage of the beam was ensured to degrade the energy of all the protons for each thickness. The thicknesses available in this configuration were in 1mm increments and it was found that the calibration curve was insufficiently constrained. Two calibration arms were designed for the second iteration of the experiment with the Perspex phantom. The calibration results are detailed further within this chapter with each experimental set-up.

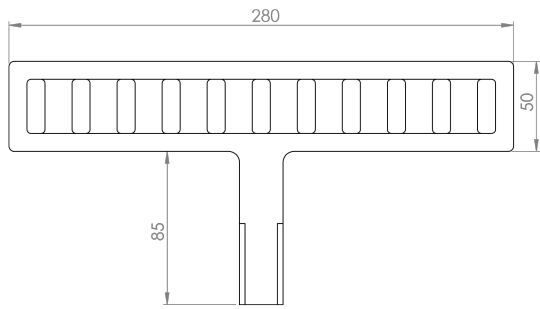
The calibration arms were designed with a series of stepped Perspex thickness with a regular spacing. The different regions of varied thickness were milled from a single piece of Perspex which could be mounted to a moving stage. The position of the moving stage, and hence position of the calibration arm in relation to the beam, could be altered from the cyclotron control room. Their design specifications are shown in Figure 5.6.

5.2.4 Pixel Sensors

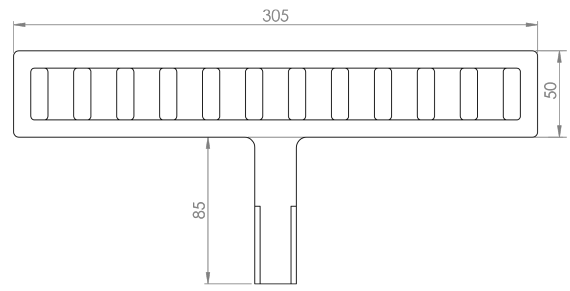
Two iterations of the experiment investigating the Hybrid approach were performed. The first of the experiments used a sensor called Priapus which was developed during the PRaVDA project [84]. The second experiment used a small version of a commercially available pixel sensor called LASSENA [85].

5.2.4.1 Priapus

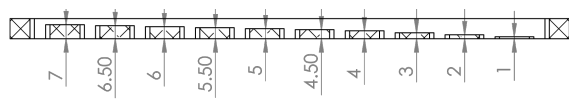
Priapus has a pitch of $198\mu\text{m}$, an epitaxial thickness of $18\mu\text{m}$, substrate thickness of $735\mu\text{m}$ and covers an active area of $5\text{cm} \times 10\text{cm}$ [84]. Two of these sensors were butted together to form a total active area of $10\text{cm} \times 10\text{cm}$. This active area is suitable for the imaging of small objects such as the phantoms designed for this investigation. Larger



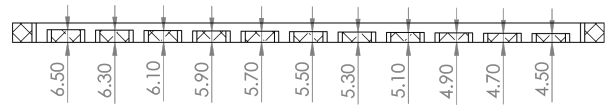
(a) Arm A.



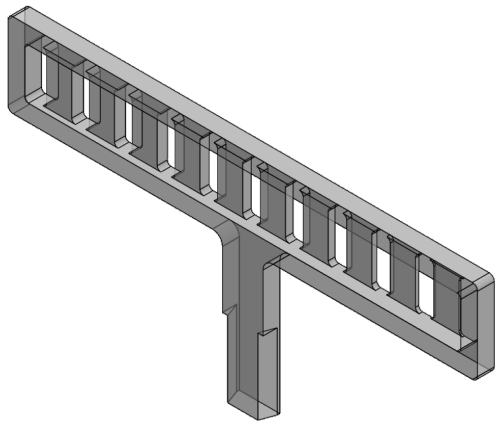
(b) Arm B.



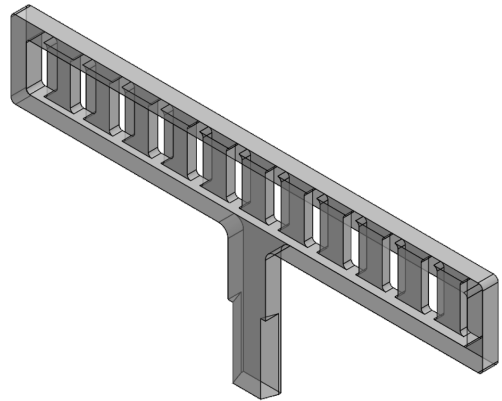
(c) Arm A top.



(d) Arm B top.



(e) Arm A in 3D.



(f) Arm B in 3D.

Figure 5.6: Schematic diagrams of the calibration arms comprising various thicknesses of Perspex.

imaging areas may be achievable through tiling of sensors or using devices which are buttable on multiple sides.

Priapus was read out every 22ms, which was slower than the 38ns of the trackers. This slower readout rate meant that Priapus would contain signals from multiple protons in every frame. The averaging technique used in the Hybrid approach utilises the increased statistics that this offers for the signal measurement.

5.2.4.2 LASSENA

The LASSENA sensor used for the second iteration of the Hybrid experiment had an active area of $60.2\text{mm} \times 62.4\text{mm}$ with $50\mu\text{m}$ pitch. The sensor read out every 29ms which was slightly slower than Priapus. This slightly slower readout rate was not detrimental to the Hybrid study as the analysis technique required all recorded frames to be summed together. The thickness of the epitaxial layer of silicon is $5\mu\text{m}$ on a $700\mu\text{m}$ thick substrate.

The version of the LASSENA sensor used in this investigation was smaller than the full sized version [85]. The full sized sensor has the advantage of covering a much larger area of $12\text{cm} \times 14\text{cm}$. The full sized version has also been developed to be buttable on three of its sides. The sensor being able to be butted against neighbouring sensors allows for a much larger area to be instrumented and be comparable to the requirement in a clinical setting. The small version of LASSENA used for these investigations allowed proof of principle of using such a device. There is also the advantage of the sensor being commercially available if such a system were to be adopted clinically.

5.2.4.3 Pixel Sensor Simulation Model

A charge transport model for the operation of a realistic silicon MAPS device was developed in SuSi. This model simulates the generation of charge, subsequent diffusion, collection, and charge sharing across pixels. It was initially developed during the early stages of PRaVDA and was based upon the Dynamic range Adjustable for Medical Imaging Technology (DynAMITe) sensor [86]. The simulation therefore has built within it the capability of modelling $50\mu\text{m}$ pixels. This pixel size is suitable for the simulation of the LASSENA sensor. The Priapus sensor was modelled by grouping pixels in a 4×4 array to replicate the $200\mu\text{m}$ pitch.

5.3 Analysis Method

A proton deposits some energy in the silicon of each tracker unit as it traverses the detector substrate. The tracker units output the strip numbers for any strips which have a signal above the set threshold in each of the three layers. This threshold is set sufficiently high such that any detection due to noise is minimised. The threshold is kept low enough such that the energy deposition from a minimum ionising particle is still detectable. The mean energy loss in silicon for a minimum ionising particle is $388\text{eV}\mu\text{m}^{-1}$ [42] and is indicated in Figure 2.1.

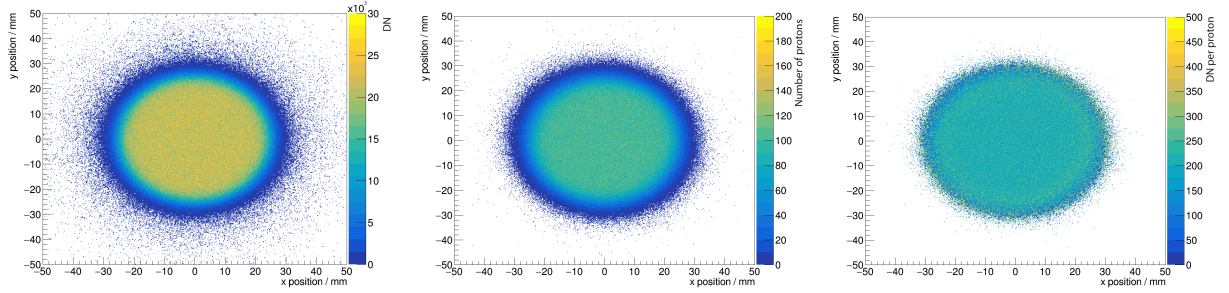
The strip hit information is then passed through the ROSETA reconstruction software, outlined in Section 3.6.5. This reconstruction software determines the position which the proton passed through the tracker from the crossing points of hit strips. This position is outputted as an x-y coordinate. Proton tracks are also reconstructed which synchronises the x-y coordinates in each tracker unit from the same proton. This synchronisation is completed using timestamp information outputted with the triggered strip numbers.

The position of the proton as it passed through the pixel sensor is calculated by projecting the outgoing track back to its surface. A corresponding pixel can be determined from this position. This back projection is completed for every proton passing through the system and is used to count the number of protons which pass through each pixel. Not all protons generate a hit in each tracker which consequently affects the number of tracks reconstructed. Missing hit information can be due to factors such as high angle scatters where the protons leave the system, protons not passing through the entire length of the system, or depositions in dead strips. These protons which do not register within the system have an impact on the tracking efficiency, ϵ , which is defined as

$$\epsilon = \frac{N_T}{N_1} \quad , \quad (5.4)$$

where N_T is the number of tracks reconstructed through the system, and N_1 is the number of hits reconstructed in Tracker 1.

The pixel sensor was read out as frequently as possible when collecting experimental data. All of the frames read out were summed together to give a total signal generated for each pixel for the entire acquisition. This signal is measured in units of “Digital Number” (DN), which has an independent scaling for both pixel devices. The DN is proportional to the number of charge carriers collected in the pixel. Dividing this total signal by the number of protons passing through each pixel gave an average signal generated per proton. This is proportional to the stopping power of the sensitive material in the pixel at the energy of the proton traversing it (Equation 5.3). This averaging process is referred to as normalisation. Every proton determined to have traversed a given pixel is then assigned to have generated that pixels average signal. Figure 5.7 demonstrates the process of averaging for the described set-up with no Perspex in place using simulated data.



(a) Total Digital Number per pixel in Priapus. (b) Number of reconstructed hits per pixel. (c) Digital Number per proton per pixel normalised from reconstructed hits in Priapus.

Figure 5.7: Normalisation process using reconstructed hits in Priapus with simulated data.

Each proton, using the determined average signal, is then assigned an equivalent Perspex thickness through which it passed according to a derived calibration curve. This is called its Perspex Equivalent Path Length (PEPL). A conversion factor of 1.15 was used to convert the PEPL to a Water Equivalent Path Length (WEPL). This conversion factor was experimentally determined in other tests performed by the PRAVDA consortium. It is this WEPL which is used for any final 3D image reconstruction.

5.4 Calibration

Each pixel sensor had to be calibrated in order to relate the signal to a traversed material thickness. Perspex thicknesses of 1mm to 7mm in 1mm increments were used with an additional measurement with no Perspex in place for the simulation and first experiment. These Perspex sheets were larger than the 5cm diameter beam size to ensure that all protons were degraded. Figure 5.8 shows the Geant4 model of this calibration set-up.

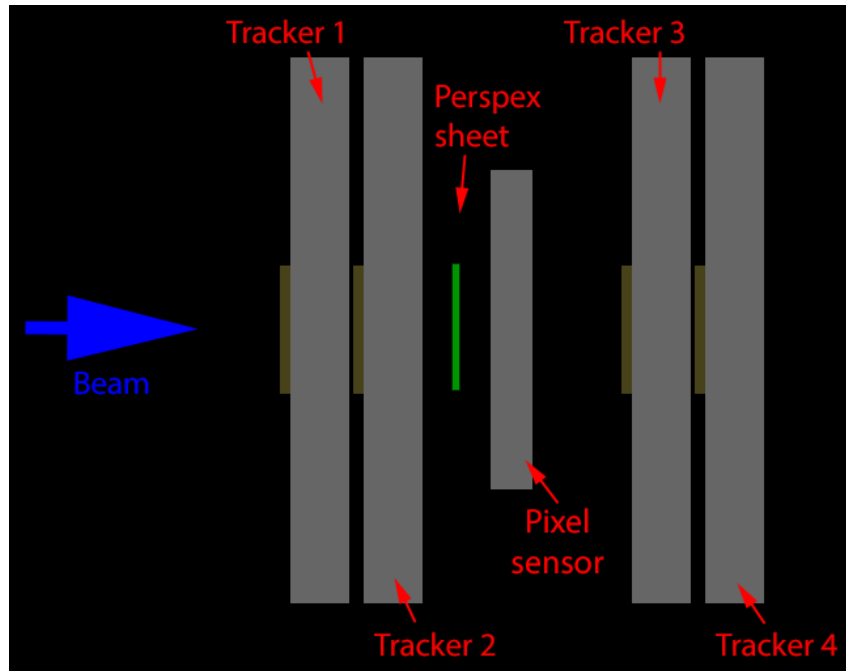


Figure 5.8: System set-up on the Birmingham MC40 cyclotron for calibration.

5.4.1 Calibration Methods

Two different methods of analysis were developed for the calibration procedure:

- Averaging of the normalised signal using reconstructed tracks.
- Averaging without normalisation using hits in Tracker 3.

Both of these methods were investigated using simulated data and the results compared to confirm agreement between the processes. The motivation for this work was because of restrictions which arose during experimental data collection, where an improperly operating fourth tracker unit gave a low track reconstruction efficiency of less than 10%. The low track reconstruction efficiency meant a realistic number of protons could not be counted using the reconstructed tracks, so counting only hits in Tracker 3 was investigated as an alternative.

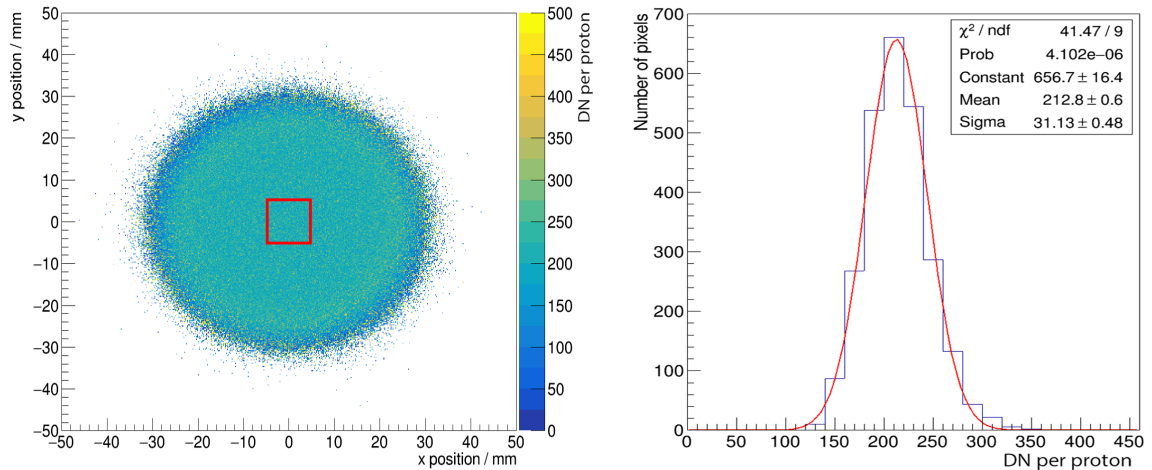
5.4.1.1 Calibration using Reconstructed Tracks and Normalisation

This process was considered for the calibration as it followed the same processing procedure as the projection data. During this process, the total signal generated from all protons passing through each pixel was summed and binned in a 2D histogram. The x and y dimensions of each bin was set to be the same as the pixel size of the pixel device used during testing. The proton hit positions in Trackers 3 and 4 were used to reconstruct the position within the pixel sensor that the proton passed through. This track reconstruction was performed on a proton by proton basis and the number of protons traversing each pixel summed in a similar 2D histogram. The division of these histograms gave the average signal generated within each pixel by each proton traversing that pixel. An example of this distribution is shown in Figure 5.9a.

The normalised average signal within a $1\text{cm} \times 1\text{cm}$ pixel area in the centre of the proton beam was then binned in a 1D histogram. This region of interest is indicated on Figure 5.9a by the red square. A Gaussian fit was fitted to this distribution and the mean value of the normalised pixel signal determined for the given thickness of Perspex. An example of this distribution is shown in Figure 5.9b. This process is conducted for all Perspex thicknesses.

5.4.2 Calibration using Hits in Tracker 3 without Normalisation

This alternative method performs counting of the protons using reconstructed hits in Tracker 3. The same $1\text{cm} \times 1\text{cm}$ region of interest is considered in the pixel sensor and the total signal in each pixel is binned into a 1D histogram. The number of proton hits in each pixel sized bin of the third tracker is also binned into a 1D histogram. These two distributions were then fitted with a Gaussian and their mean values calculated. The division of the mean total signal per pixel and the mean number of proton hits then gave the average signal per proton per pixel required for calibration. This was repeated for



(a) The average signal generated per proton per pixel. (b) 1D histogram of the average signal per pixel in the region of interest.

Figure 5.9: The method of determining the average signal per proton within a pixel. The red region in Figure 5.9a shows the region of interest containing the pixels considered for the histogram shown in Figure 5.9b.

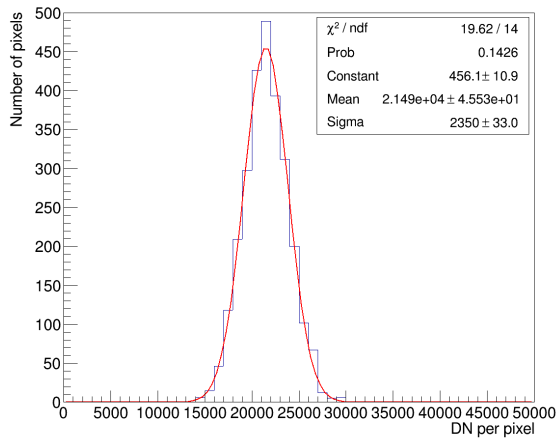
each thickness of Perspex. An example of these histograms is shown in Figure 5.10.

This method is only possible providing the third tracker unit is located close enough to the pixel sensor. This allows for the assumption that there is an equal number of protons scattering into the region of interest as out of it between the pixel sensor and the tracker. Comparison of the calibration curves using both counting methods allowed for the validity of this assumption to be examined.

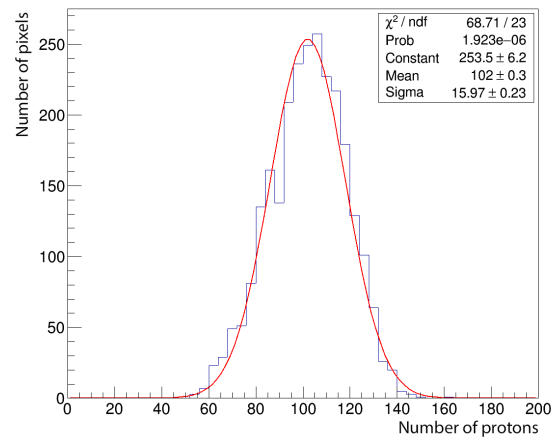
5.4.3 Calibration Methods Comparison

The measured average signal as a function of Perspex thickness for both of the described calibration methods is shown in Figure 5.11 and is fitted with Equation 5.2.

The first calibration method using reconstructed tracks in the pixel sensor is the most representative of the true method of analysis for the experiment. This study therefore examined the level of agreement if protons were counted based on the region of interest



(a) Total signal per pixel.



(b) Proton hits per pixel area in Tracker 3.

Figure 5.10: An alternative calibration method which uses proton hits in Tracker 3 to determine the average number of protons per pixel.

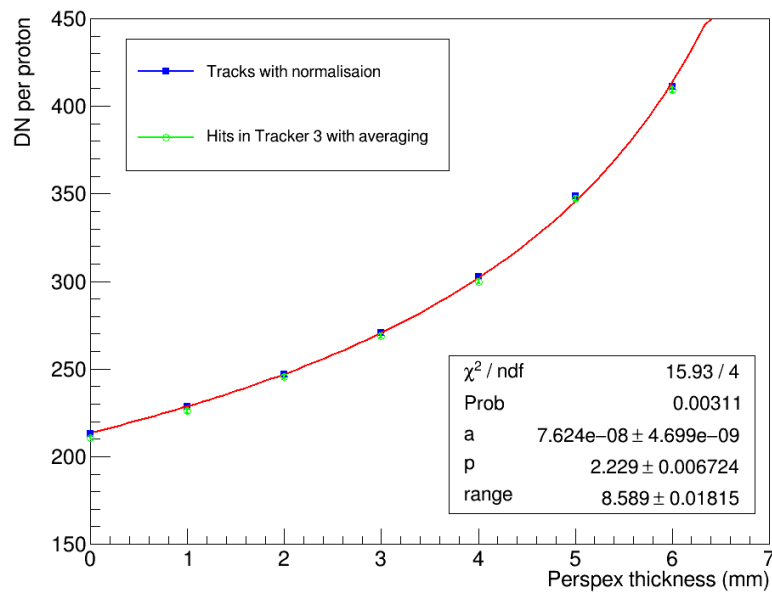


Figure 5.11: A calibration curve obtained using two alternative methods using simulated data. The blue points shows the average signal (Digital Number) generated per proton after normalisation with reconstructed tracks. The green points show the alternative averaging method which uses an average number of proton hits per pixel in Tracker 3.

in Tracker 3.

A value for the χ^2 per degree of freedom of 4.0 was determined for the fit showing acceptable agreement with the data points. The errors propagated to these points were

based on the standard error on the mean determined from the Gaussian fits applied to the associated distributions as shown in Figures 5.9 and 5.10.

The main caveat of the calibration with Tracker 3 is the additional scattering not accounted for which the protons undergo with thicker Perspex. The Tracker 3 method assumes that the number of protons entering and leaving the region of interest are the same. This is not strictly correct as there is an overall divergence of the beam ($<1^\circ$ between the pixel sensor and Tracker 3) which marginally reduces the number of protons in this region between the pixel sensor and Tracker 3. The region of interest was selected to be sufficiently small in order to reduce the contribution to this effect from the protons at the periphery of the beam. All points lie within 1σ of each other for each Perspex thickness showing good agreement. Proton counting using hits in Tracker 3 was therefore deemed a suitable alternative method to calibrate the sensor.

5.5 Balsa Phantom Study

The experiment and simulation of the balsa phantom was used to examine the initial concept of the Hybrid approach. This experiment was also performed with a 5cm diameter broad beam and a 6mm diameter spot scanned beam. This allowed examination of the ability of the Hybrid approach to perform in facilities able to deliver both types of proton beams. The experimental set-up on the Birmingham MC40 cyclotron was matched to the simulation so results could be directly compared.

5.5.1 Set-up

The experimental and simulated set-up with the balsa phantom is shown in Figure 5.12.

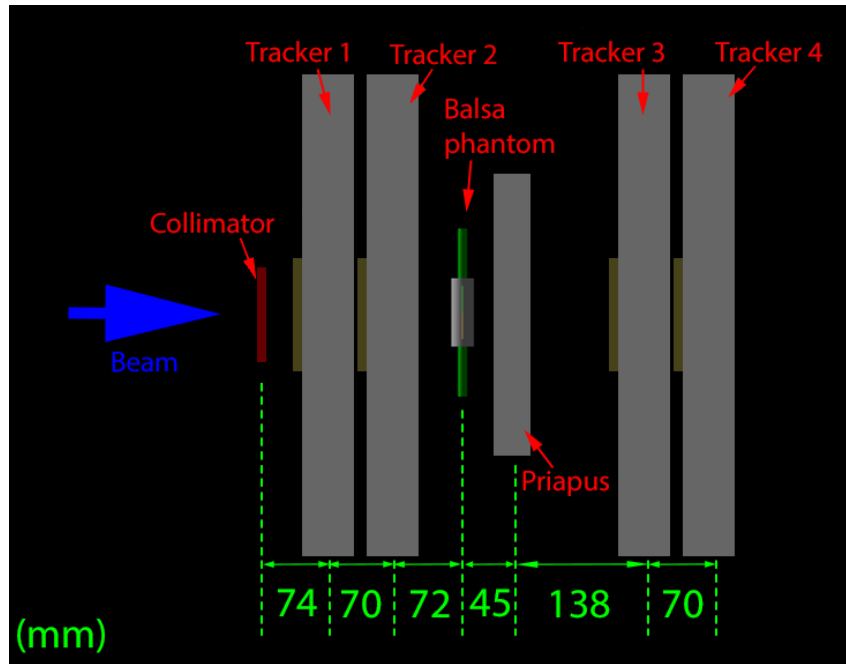


Figure 5.12: Set-up of the balsa phantom experiment and simulation. Dimensions are in mm and the diagram is not to scale.

The low 36MeV proton energy at the Birmingham MC40 cyclotron compared with clinical proton energies meant that the components of the system had to be positioned as closely as possible. Additional spacing would increase the amount of air through which the protons lose energy and decrease the potential imaging depth through the phantom. The larger spacing between Priapus and Tracker 3 was due to the size of the structure used to mount the sensor.

The low density phantom with a main body of balsa wood was used for this investigation. The collimator was mounted on a motor driven moving stage which allowed 2D movement to vary the spot position when performing the pseudo-spot scan. This collimator was removed for the broad beam investigations with all other system components in the same positions. The broad beam used was of 5cm diameter.

5.5.2 Simulated Calibration

The calibration for this experiment was performed with thicknesses of Perspex from 0mm to 7mm in 1mm increments. The 10cm \times 10cm active area of silicon strip and pixel sensors meant the entire beam could be covered. The position of the Perspex sheets was the same as the balsa phantom position labelled in Figure 5.12.

5.5.3 Simulated Projection

The calibration method using normalisation was used for the analysis of the simulated projection data. The parameters of the fitted curve using Equation 5.2 are shown in Figure 5.13.

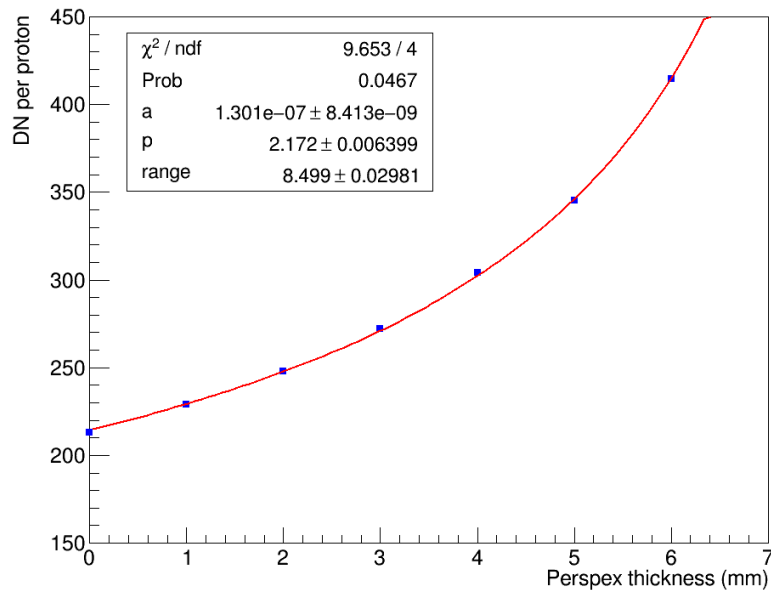


Figure 5.13: The calibration curve for the balsa phantom set-up fitted with Equation 5.2 using simulated data.

The symmetry of the balsa wood phantom simplified the simulation as rotation was not required. A projection of the phantom with both broad and pseudo-spot scanned beams was performed. The signal in the pixel sensor was summed for all protons and then

normalised using reconstructed tracks projected back to the pixel layer. A PEPL value was determined for each pixel using the average signal per proton and the parameters obtained from the calibration curve. PEPL was then converted to a WEPL using the experimentally obtained 1.15 conversion factor.

Figure 5.14 shows the average signal per proton per pixel normalised from reconstructed hits in Priapus for both the broad beam and the spot scan simulations. Figure 5.15 shows the WEPL for both incident beam types.

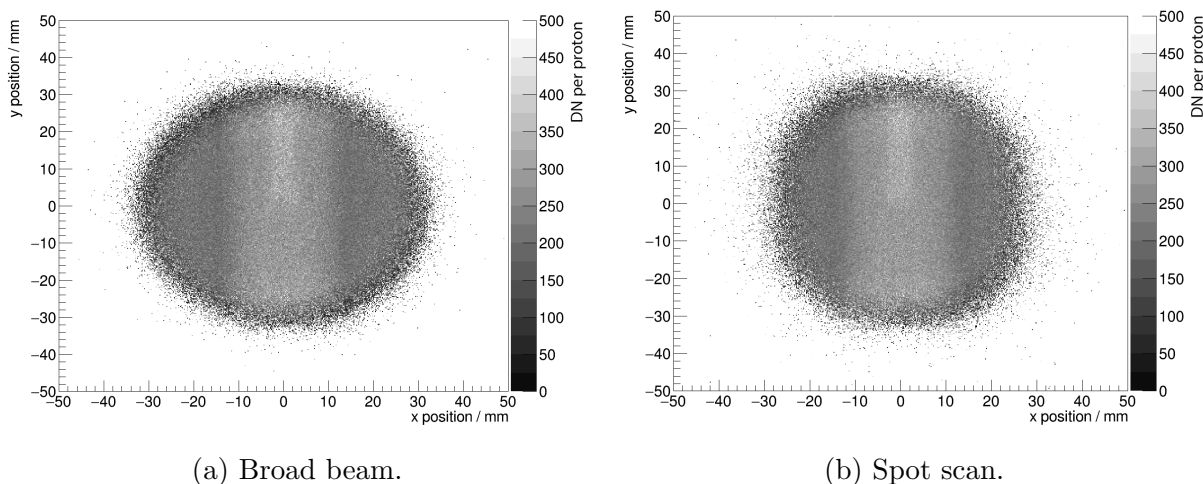


Figure 5.14: Average signal (in units of Digital Number) per proton per pixel in Priapus normalised from reconstructed hits in Priapus for broad beam and spot scan simulated data.

It can be seen in Figures 5.14 and 5.15 that there is no clear difference in the quality of the 2D radiographic images between a broad beam and pseudo-spot scanned beam. Line profiles were taken across the top and bottom regions of the phantom to examine the difference in quality of the images more closely. This analysis is also more reflective of clinical practice due to the requirement of measuring the WEPL of internal structure. The top half contained the Perspex insert and the bottom half contained the air insert. Figure 5.16 shows these line profiles.

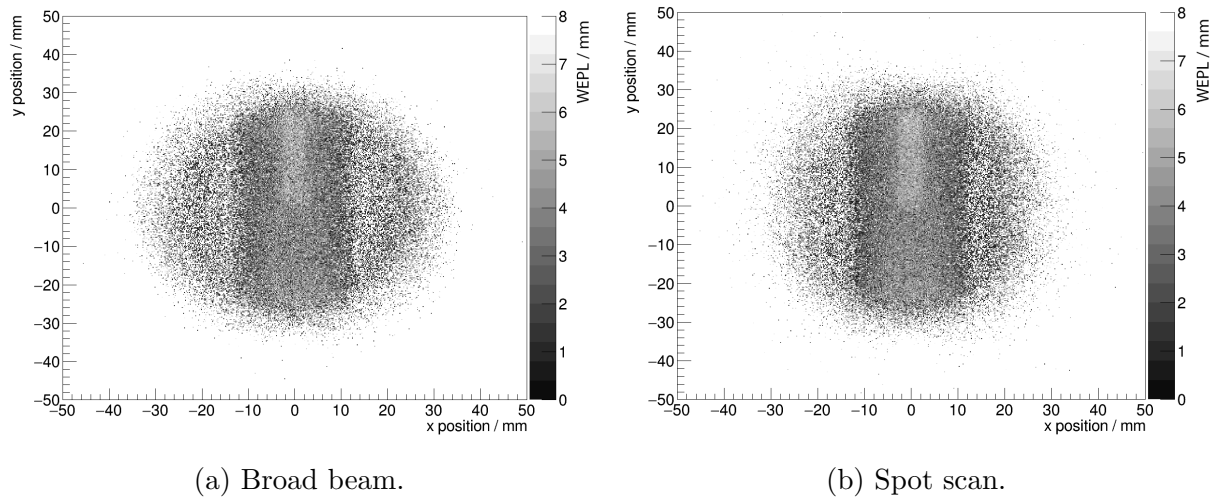
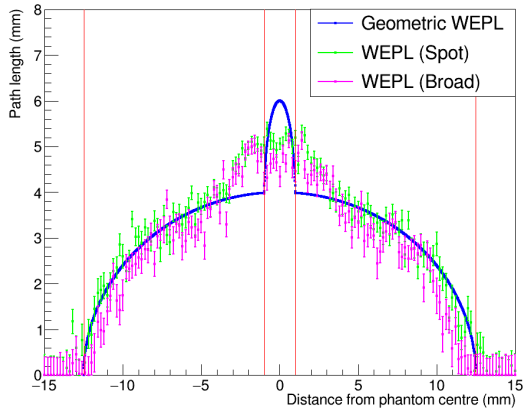


Figure 5.15: Water Equivalent Path Length (WEPL) per proton per pixel in Priapus normalised from reconstructed hits in Priapus for broad beam and spot scan simulated data.

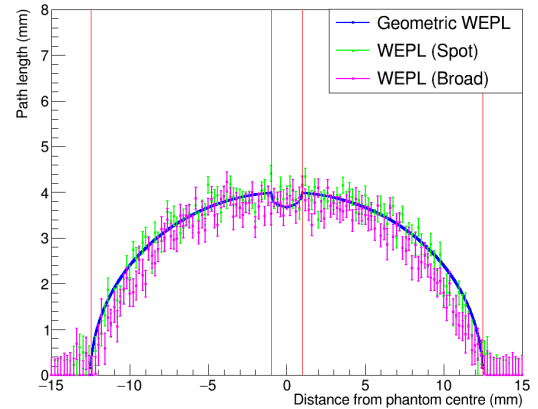
Each point of the measured WEPL from simulation is the average of a region of pixels 10mm high and $200\mu\text{m}$ wide. These average values are plotted as a function of the position across the phantom. The blue curve is the WEPL of the balsa phantom based on the geometry. This WEPL has been calculated using the relative densities of the materials with relation to water. The profiles were determined for both the broad beam and spot scanned beam for direct comparison. The red lines in Figure 5.16 show the position of the outermost edges of the phantom and the edges of the inserts.

It can be seen that the broad beam and spot scanned beam agree with each other in both the top and bottom regions of the phantom. The balsa wood region of the phantom in both halves shows good agreement between the expected WEPL based on the geometry and that which has been measured using simulated data. There is good contrast at the outermost edges of the phantom as a WEPL of 0mm is measured within $200\mu\text{m}$.

The cylindrical shape and low density of the surrounding balsa wood meant that the small air region was difficult to observe in the results, as there was no clear contrast between the materials. The measured values in the air insert do, however, lie within



(a) Top half with Perspex insert.



(b) Bottom half with air insert.

Figure 5.16: Profiles through the top and bottom halves of the balsa phantom using simulated data. The blue curve represents WEPL based on the geometry of the phantom and relative densities of the materials. The red lines indicate the insert and outermost edges of the phantom.

their uncertainties of the expected WEPL based on the geometry in the bottom half of the phantom.

The profile across the top half of the phantom shows agreement between the geometric WEPL and that measured through simulation within the balsa wood section. The presence of the higher density Perspex region in the centre of the phantom is also clear. The magnitude of the WEPL measured from simulation in the centre of the insert does not match entirely with the geometric WEPL. It should be noted that the geometric WEPL is not expected to be identical to the WEPL measured through energy loss. This is because the energy loss rate does not follow a linear relation with the thickness of material. There is also going to be an increase in the scatter of the protons passing through this highest density region which would cause the protons to disperse. This would give rise to a broadening of the peak expected at the Perspex insert, and a decrease in the magnitude at its centre. This effect is clearly observed.

5.5.4 Experimental Calibration

It appeared in the experimental calibration data for the balsa phantom set-up that protons did not have sufficient range in the system to reach Tracker 4 after traversing 6mm and 7mm of Perspex. Calibration was therefore performed using hits in Tracker 3 where all protons were counted. The tracking data for 5mm of Perspex was not usable so has been omitted from the calibration. The calibration curve, fitted with Equation 5.2, is shown in Figure 5.17.

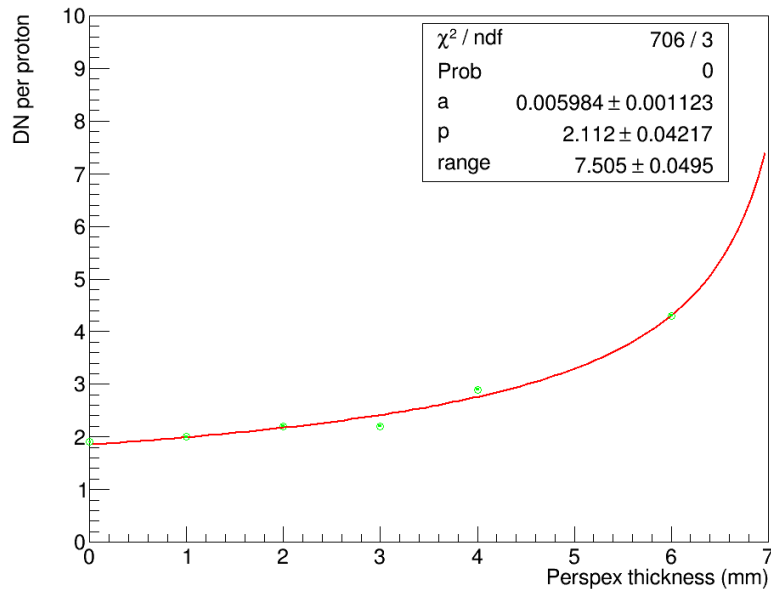


Figure 5.17: Calibration curve obtained from experimental data using the balsa phantom set-up. Calibration was performed by counting hits in Tracker 3.

5.5.5 Experimental Projection

The calibration curve shown in Figure 5.17 was applied to the normalised image in Priapus yielding the WEPL distribution shown in Figure 5.18. The line down the image at $x = 0\text{mm}$ is due to the physical separation between the two halves of the Priapus sensor.

The main body of the balsa phantom can be clearly seen in Figure 5.18. There is

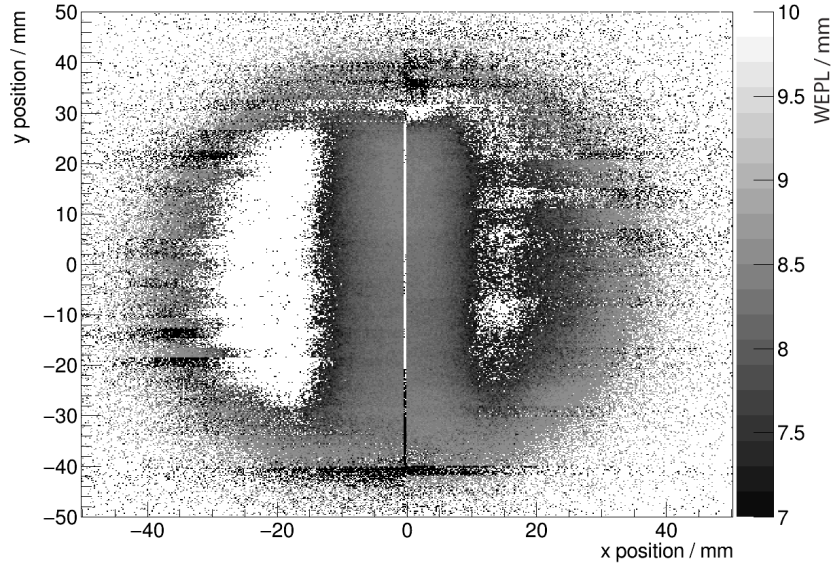


Figure 5.18: 2D distribution of the WEPL of the balsa wood phantom using the calibration curve shown in Figure 5.17 on experimental data.

however little suggestion of the presence of either of the inserts. The value of the WEPL measured is also consistently above what is expected for the phantom. This higher than expected WEPL is because of a consistently low track reconstruction efficiency, of the order of 20%, observed in the calibration data. Section 5.4 outlines that calibration using either reconstructed tracks or hits in Tracker 3 should yield the same results. This is true given the scenario of near 100% track reconstruction efficiency, as had been seen in simulation. The consistently low track reconstruction efficiency meant there was a significant factor between the number of reconstructed tracks and number of reconstructed hits. Consequently, when the hit calibration was applied to the track normalisation required for the projection data, an inflated WEPL was observed.

The normalised projection image, before applying the calibration, shows a very different view of the obtainable image. This distribution is shown in Figure 5.19.

This normalised image demonstrates that the structure of the balsa phantom can be clearly observed in experiment. The average signal can be seen to decrease when moving

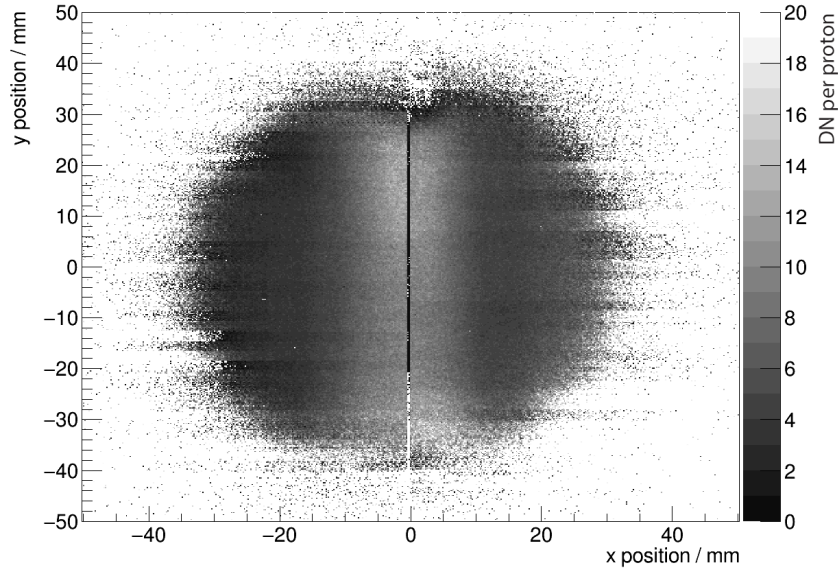


Figure 5.19: The average signal per proton (after normalisation) for a projection of the balsa wood phantom using experimental data.

towards the edges of the phantom as is expected from the reduction in material thickness. The presence of the higher density Perspex insert can be fairly well observed in the top half of the phantom. The air insert is difficult to distinguish in this radiograph, which also agrees with the simulated result (see Figure 5.16b). This normalised image therefore matches the result expected from the simulation study of this set-up well, and demonstrated that there was a critical requirement for a well constrained and accurate calibration curve. This result is very promising for the Hybrid procedure.

5.6 Perspex Phantom Study

5.6.1 Motivation

The experiment with the balsa wood phantom demonstrated the ability to observe its internal structure using the Hybrid system. The analytic procedure proved successful up to obtaining a normalised image in Priapus. Problems with the calibration data however

meant that a conversion of this average signal to a WEPL was inaccurate. The main contributions to the degradation of the final WEPL image were

- An insufficiently constrained calibration curve.
- A track reconstruction efficiency consistently below 20%.
- A phantom thickness which was too large and stopped protons reaching the end of the system.

These problems were addressed in a second iteration of the experiment. The solutions proposed were

- Perform calibration with a larger number of Perspex thicknesses to better constrain the curve.
- Perform a phase sweep¹ to ensure maximum track reconstruction efficiency was achieved.
- Redesign of the phantom to have a more consistent and lower equivalent Perspex thickness.

Additional variations to the experiment were made to improve the results and address additional problems which arose. These are discussed in more detail in the following set-up and procedural discussions.

5.6.2 Set-up

The experimental set-up used to image the Perspex phantom is shown in Figure 5.20.

¹A phase sweep is a set-up procedure of the tracking system to ensure it is synchronised with the cyclotron clock frequency. More detailed discussion is given in Section 3.6.3.

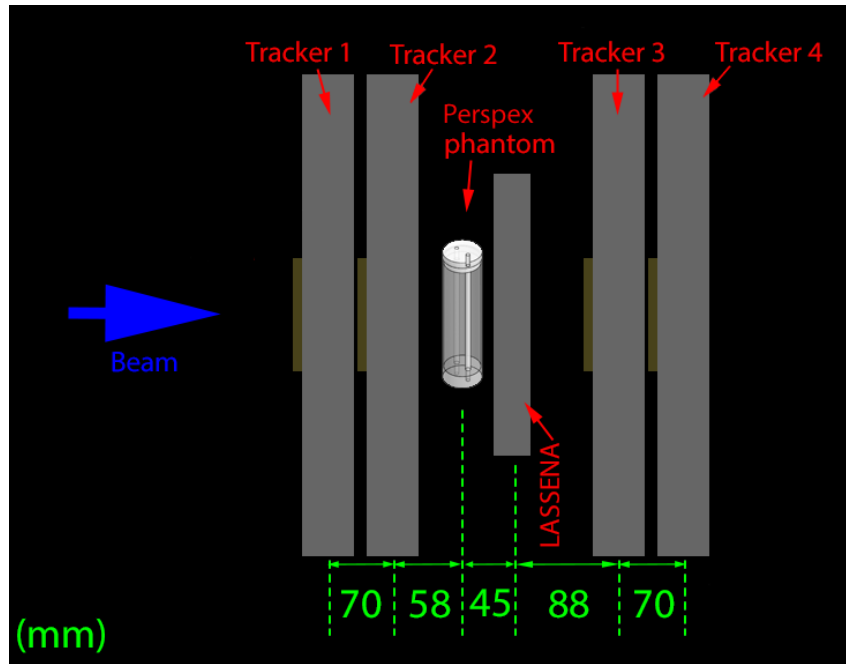
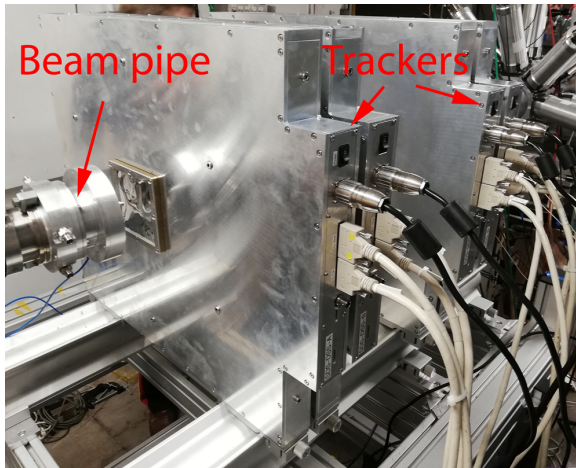


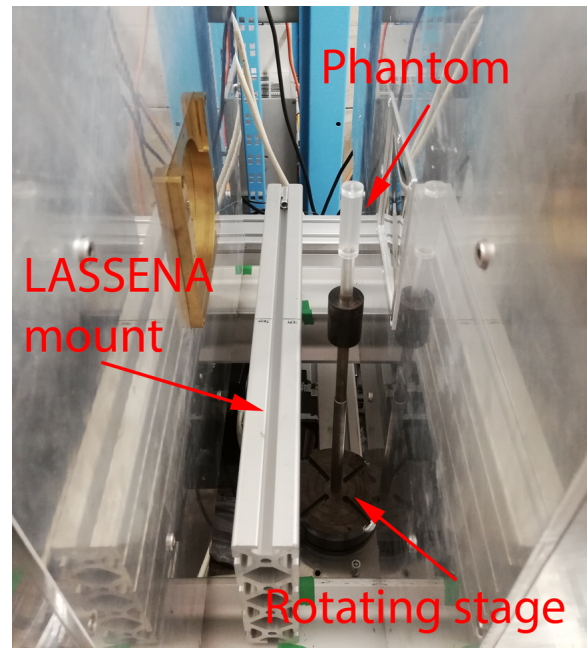
Figure 5.20: Set-up of the Perspex phantom experiment and simulation. Dimensions are in mm and the diagram is not to scale.

Figure 5.21a shows the arrangements of the four tracker units. The system was butted as close to the beam pipe as possible in order to reduce the degradation of the energy of the beam as much as possible before it passed through the system. All the trackers were secured to a bench which allowed for accurate alignment with the beam. There is a separation between the first two and last two tracker units for the mounting of the phantom and pixel sensors. Figure 5.21b shows the region between Trackers 2 and 3. The phantom was mounted on the rotating stage close to the exit window of Tracker 2. The phantom beside this window can be seen in Figure 5.21c. A metal plate was placed across the bench to support the pixel sensor in position in alignment with the phantom and beam. The pixel sensor can be seen in place behind a calibration arm in Figure 5.21d.

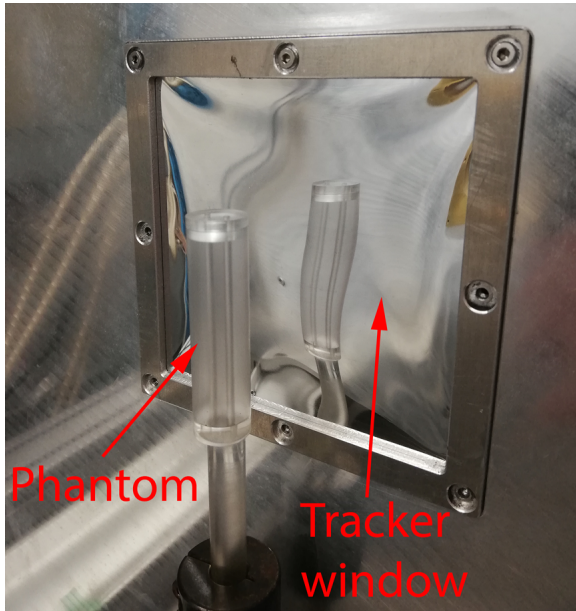
The smaller size of the LASSENA sensor compared to Priapus meant that the full 5cm diameter proton beam could not be used as it had been for with the balsa wood phantom. The 5cm diameter beam was alternatively collimated down to a $1\text{cm} \times 1\text{cm}$ beam when performing calibration and $2\text{cm} \times 2\text{cm}$ when performing the experimental



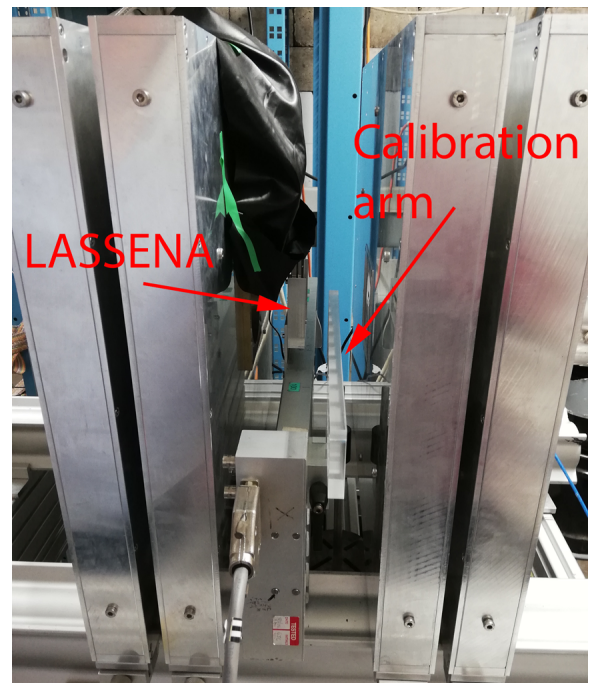
(a) Tracker set-up.



(b) Phantom on rotating stage.



(c) Phantom behind tracker window.



(d) LASSENA in position with calibration arm.

Figure 5.21: Images of the experimental set-up with the Perspex phantom.

projections. The protons had an energy of 36MeV. The simulation of the balsa wood phantom demonstrated that there was no difference between operating in a broad beam mode or a pseudo-spot scanned mode. The broad beam mode was therefore adopted as this significantly reduced the acquisition time for a single projection angle. This allowed the time to be reallocated to obtaining additional projections with the phantom rotated for the purpose of 3D reconstruction. The phantom was mounted on a rotating stage which allowed for 1 degree variations in the angle of the phantom relative to the beam.

The focus of the results using the Perspex phantom were on 0° and 90° rotations. The set-up of these orientations in relation to the beam are shown in Figure 5.22 and shall be referred to throughout the text.

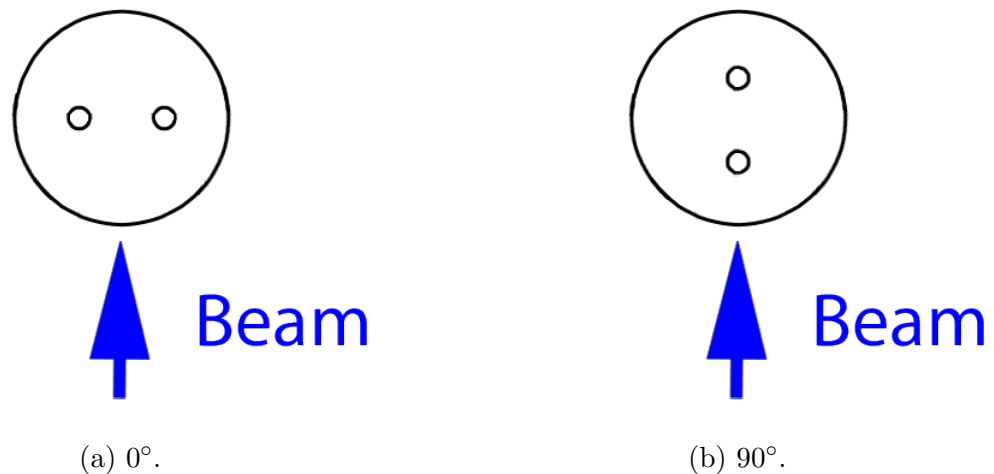


Figure 5.22: The rotation of the Perspex phantom in relation to the proton beam.

The arrangement of the system was adapted from that used in the balsa wood phantom experiment which allowed for a more compact system. Of particular importance was the outgoing trackers being closer to the pixel sensor. This meant that there would be less air for the protons to have to travel through before they reached Tracker 4 and consequently have an increased probability of being detected. This would therefore lead to an increase

in the tracking efficiency; particularly at higher Perspex thicknesses.

5.6.3 Simulated Calibration

The same thicknesses of Perspex were used in simulation for the calibration as were used in the balsa wood phantom simulation. This was because the variation in the calibration curve at low Perspex thickness, and the accuracy of the constraining of the curve, were sufficient to obtain a good calibration without additional data points. These Perspex thicknesses ranged from 0mm to 6mm in 1mm increments. The same analysis method as described in Section 5.4 was used which focused on determining the average signal per pixel in a $1\text{cm} \times 1\text{cm}$ region of interest and allocated this to an equivalent Perspex thickness on the calibration curve. The curve was then fitted with Equation 5.2.

The resultant calibration curve is that which is shown in Figure 5.11. The fit was very close to that obtained for the balsa wood phantom simulation. This is as expected as the general set-up of the simulations was very similar. It was however important to ensure the calibration correctly matched the geometric set-up of the system as was used for the projection, otherwise, additional energy losses as protons travel through the air would affect the results.

5.6.4 Simulated Projection

The analysis process of the projection data was the same as outlined in Section 5.3. Two projections were simulated for analysis; the first at 0° such that the alignment of the inserts was perpendicular to the beam and the second at 90° such that the inserts were aligned parallel with the beam. The resultant average signal per proton for both angles is shown in Figure 5.23. Their conversion using the calibration curve in Figure 5.11 is shown in Figure 5.24.

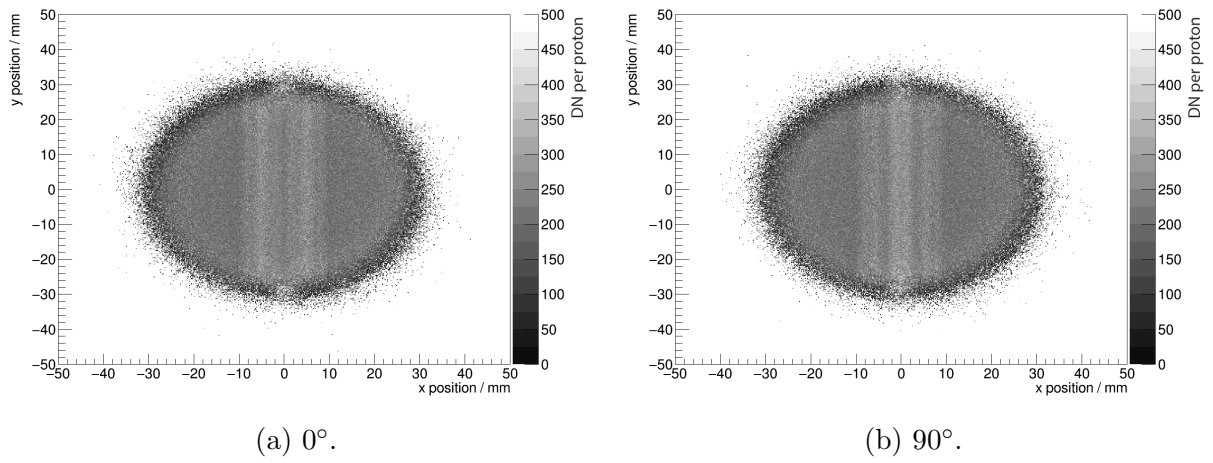


Figure 5.23: 2D distributions of the average signal per proton of the Perspex phantom at two orientations using simulated data. Inserts are aligned perpendicular and parallel to the beam for Figures 5.23a and 5.23b respectively.

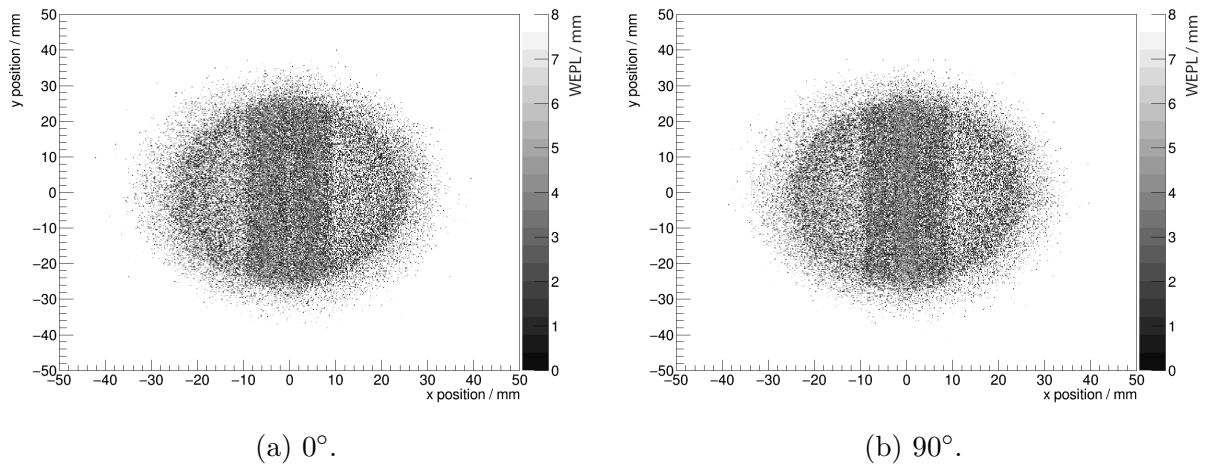


Figure 5.24: 2D distributions of the WEPL per proton of the Perspex phantom at two orientations using simulated data. Inserts are aligned perpendicular and parallel to the beam for Figures 5.24a and 5.24b respectively.

It is apparent from the distribution of the average signal per proton in Figure 5.23a that there is existence of a minimum at $x=0\text{mm}$. Two separated peaks in the distribution are also observed as well as a clear outer boundary of the phantom structure. Figure 5.23b similarly shows a single peak at $x=0\text{mm}$ due to the larger path length caused from the alignment of both inserts with the proton beam. The outer most boundary of the

phantom can similarly be observed in this image surrounding minima created from the void within the phantom.

5.6.4.1 Projection to the Phantom Plane

It is important here to consider that the average signal per proton is a measurement at the plane of the pixel sensor. The use of the calibration curve derives a WEPL at the plane of the phantom from the signal at the plane of the pixels. These 2D WEPL distributions therefore describe the WEPL that each of the protons travelled through when they passed the phantom plane. They have however changed their (x,y) position since traversing the distance between the phantom plane and the pixel plane. The individual proton tracking allows for the projection of the protons back to the phantom plane having now been assigned their WEPL. The resultant 2D distributions of the WEPL at the phantom plane after further back projection is shown in Figure 5.25.

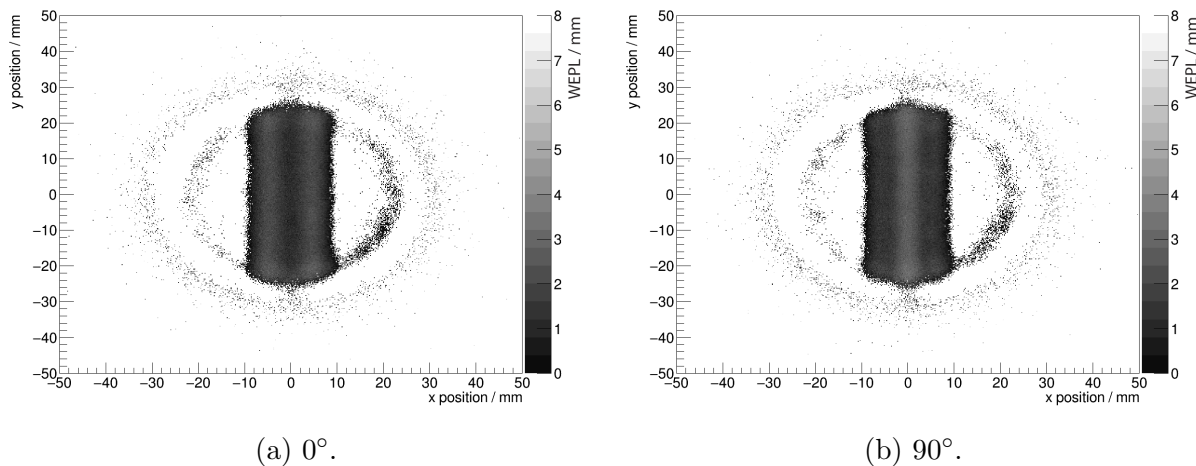


Figure 5.25: 2D distributions of the WEPL of the Perspex phantom at the phantom plane for two orientations using simulated data. Inserts are aligned perpendicular and parallel to the beam for Figures 5.25a and 5.25b respectively.

This additional back projection to the phantom plane determines the equivalent pixel position at this plane for each proton. The mean value of the WEPL in each equivalent

pixel is then calculated to produce the images shown in Figure 5.25. It can be seen that there is a distinct improvement to the clarity of the WEPL image when projected to the phantom plane. This is because this back projected WEPL distribution is determined from the protons which have exited the phantom from the same position, and therefore travelled comparable WEPLs. In comparison, the distributions without back projection has contributions in each pixel from protons travelling an increased variation of WEPLs in the phantom.

There is expected to be some discrepancy between the phantom structure measured in this image and the geometric structure because of the scattering which occurs within the phantom. This discrepancy is expected to be accounted for during the most likely path calculation of 3D reconstruction methods.

5.6.4.2 Insert Position

The off-centre position of the inserts in this phantom allowed for closer inspection of the accuracy of their reconstructed position. This was an observable which was not visible using the 360° symmetric balsa phantom. Line profiles across the phantom at $y=0\text{mm}$ were produced to examine this, for both 0° and 90° projections, and are shown in Figures 5.26a and 5.26b respectively. These have been plotted along with the profile of the geometric WEPL across the phantom. The red lines indicate the boundaries of the walls and inserts of the phantom.

It is apparent from Figure 5.26a that the position of the maxima do not correspond with the geometric position of the inserts. Some features to the line profiles in both the 0° and 90° images are seen at the phantom walls suggesting their presence, but this effect is minimal. The existence of only 2 peaks instead of 4, at 0° rotation, is explained by their position being between the phantom wall and inserts on each side. The scattering of

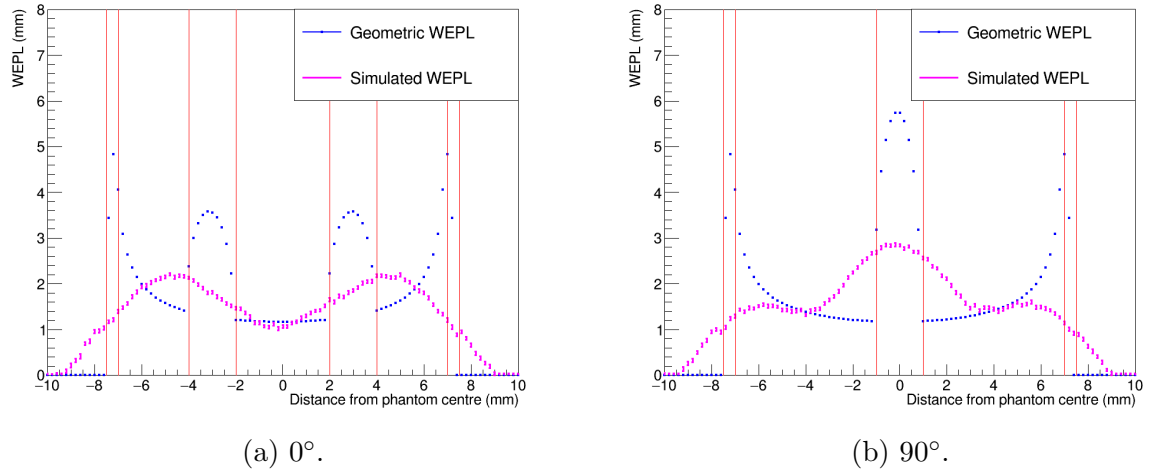


Figure 5.26: Line profiles of the WEPL at a value of $y=0\text{mm}$ for the simulated distributions shown in Figure 5.24.

the protons has caused distortion of the distribution sufficiently in a 2D image that the WEPL measurement from the wall and inserts merge. The peak is not perfectly centred between the wall and insert because of the increased number of protons contributing to a higher WEPL originating from the insert. This is due to the wider 2mm diameter of the insert compared to the $500\mu\text{m}$ thick wall. This statistical contribution leads to a shift of the merged peak to be closer to the insert position.

The 90° projection shown in Figure 5.26b emphasises why this effect was not observed during the balsa phantom studies. This geometry is similar to the balsa phantom with a single central peak. Though the apparent merging of peaks will still be present, there will be no net shift in the position of the maxima due to equal contributions from both positive and negative directions on the x-axis. This emphasises the value of the Perspex phantom study.

5.6.5 Experimental Calibration

The smaller active area of the LASSENA sensor in comparison to Priapus made it more difficult to achieve good alignment of the detector systems and phantom. This was most apparent when using the calibration arms and the $1\text{cm} \times 1\text{cm}$ beam. A small misalignment resulted in only partial beam coverage with the Perspex. This meant that the protons within the beam did not all pass through the same Perspex thickness, and hence distorted the measurement of the average signal. The scattering of the protons would also not be uniform, which would result in the number of protons per pixel within the region of interest of Tracker 3 to be distorted from that expected. An accurate calibration curve could therefore not be obtained which matched the method of analysis for the projection data.

An ideal experiment would be one with a track reconstruction efficiency of 100%. In such a case, the number of reconstructed tracks would match the number of reconstructed hits in each of the tracker units. The number of protons within the region of interest could be considered to be the same in Tracker 2 as in Tracker 3 for a uniform beam traversing the Perspex. This is because despite the increased number of protons scattering out of the region, the same number of protons would scatter into it. This assumption was confirmed to be true through simulation for all Perspex thicknesses from 0mm to 7mm.

A calibration curve was obtained using the number of hits within the $1\text{cm} \times 1\text{cm}$ region of interest in Tracker 2 to perform a calibration. The result of this calibration is shown in Figure 5.27.

The calibration curve obtained using hits in Tracker 2 and experimental data yielded a very positive result for the calibration procedure. The curve when fitted with Equation 5.2 was well constrained with a value of the χ^2 per degree of freedom of 3.2. The edge of the calibration curve where its gradient increased the fastest had many more points

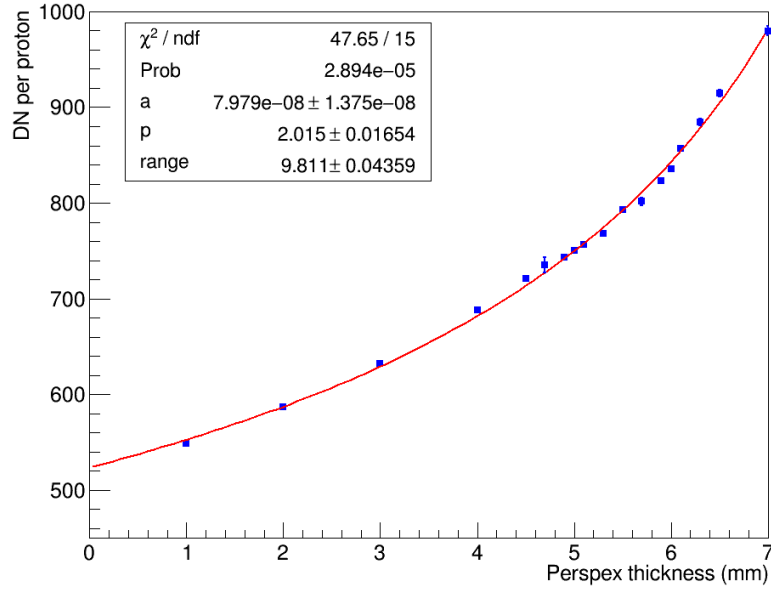


Figure 5.27: The calibration curve obtained for the Perspex phantom experiment. The region of interest considered to count the number of protons per pixel was located in Tracker 2 due to miss-alignment of the beam.

to help constrain it in comparison to the balsa phantom experiment (Figure 5.17). The curve may have been better constrained in the region of smaller Perspex thickness which corresponds to a large proportion of the phantom.

5.6.6 Experimental Projection

Unlike Priapus, the small version of LASSENA had a limited memory which would be overwritten after a short period of acquisition. Synchronisation of the tracker system and the pixel sensor, with consideration of this small on-board memory, meant that only approximately 2 seconds of data could be taken per projection. This reduced the statistics available for the analysis and made it difficult to accurately align the tracks with the pixel distribution for normalisation. It was then not possible to use the calibration curve to get an image of the WEPL without the average signal per proton in each pixel.

The images obtained from the LASSENA sensor were however very promising. These

are shown in Figures 5.28a and 5.28b for 0° and 90° rotations respectively. The pixel distributions have been shifted such that the phantom is centred on $x=0\text{mm}$. The alignment of the phantom along the x-axis has been indicated in red on the Figures.

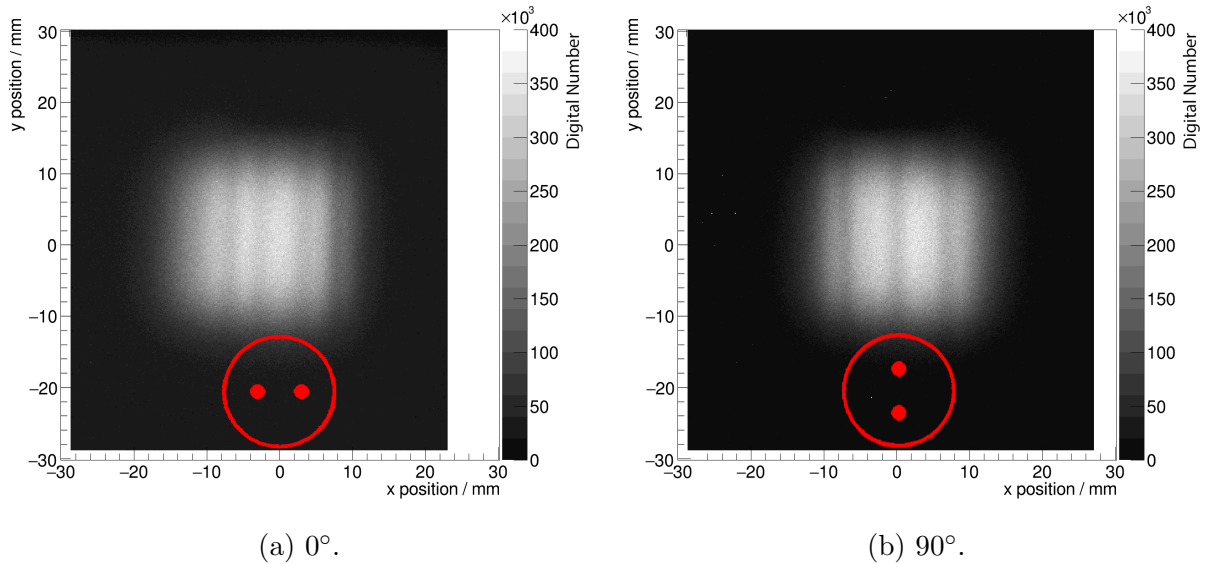


Figure 5.28: 2D distributions of the total signal in each pixel using experimental data from the Perspex phantom at two orientations. Inserts are aligned perpendicular and parallel to the beam for Figures 5.23a and 5.23b respectively. The alignment of the phantom has been indicated in red.

The presence of the walls of the phantom can be clearly seen in both of these projection images. Two inserts can be seen in Figure 5.28a whilst Figure 5.28b shows only the single minima as the inserts are aligned.

5.7 Conclusions

The PRaVDA group developed a system with suitably performing silicon strip trackers for individual proton tracking with minimal ambiguities for a broad beam of protons. The energy measuring device was of the form of a 22 layer Range Telescope which detected the range of protons through a stack of Perspex absorbers in order to accurately

measure the energy. This was suitable for operation at the iThemba Labs [74] 191MeV passively scattered clinical facility, with the addition of a compensator. This compensator degraded the energy of protons which passed through less material in the phantom so they were of a sufficiently low energy to be contained within the Range Telescope.

More modern clinical facilities, such as that which now operates at The Christie in Manchester [24], use spot scanned beams. The use of compensators for proton treatments has become impractical with the multiple gantry angles required for both proton treatment and the long term goal of pCT. Without a compensator, a much larger Range Telescope would be required in order to measure the entire beam energy, which becomes unsuitable for regular clinical treatment. The high proton current at modern facilities adds additional complications to the design of a suitable device which measures the energy of individual protons.

Examination of the proposed system for the Hybrid Approach has been completed using simulation and verified through experiment. It has been shown that there is no difference between the images obtained from this approach when using a broad beam or a spot scanned beam. Simulation of a balsa wood phantom containing Perspex and air inserts showed the WEPL measured using the Hybrid technique agreed well with the WEPL determined from the phantom geometry. An experiment was conducted matching the simulation using a 36MeV from the Birmingham MC40 cyclotron [73]. Low tracking efficiency led to difficulty in obtaining a suitable calibration curve relating the average signal in the pixel device to a WEPL, and consequently impacted the final WEPL images. The presence of the Perspex insert within the balsa wood body of the phantom was clearly evident, matching well with simulation, and proved this approach to be promising.

A second examination using simulation and experiment was performed using a Perspex

phantom containing off-centre inserts. A well constrained calibration curve was achieved experimentally during this investigation. The curve was fitted with Equation 5.2 and yielded a value of the χ^2 per degree of freedom of 3.1. Low statistics in the projection data made it difficult to measure the WEPL using the complete analysis procedure. Clear images within the total signal per pixel in the LASSENA sensor were, however, a good indication of the quality of images that may be obtainable through this approach.

These results with the phantom at a rotation corresponding to an off-centred maxima in the geometrical WEPL showed that the Hybrid method alone is not suitable for reconstructing true geometric positions, and therefore WEPL, in 2D images. This should however not be taken as direct evidence for the unsuitability of the Hybrid approach in clinical practice. Further analysis which includes the full 3D reconstruction of a pCT image would be required in order to reach this conclusion. The contribution of multiple projections to a final 3D image offers additional information which may not be obviously apparent from the 2D distributions. For example, the small features observed in Figures 5.26a and 5.26b at the outer wall boundary, if present for all projections, could result in the accurate position and increased overall WEPL for the phantom wall. This is despite these features in a single projection seeming insignificant.

An influencing factor on the reconstructed position of structures within the phantom is understood to be the scattering of the protons. A deeper consideration of this scatter, including its expected impact on the images, and examination into how it can be used to improve the quality of the images is discussed in Chapter 6.

Chapter 6

Using Proton Scattering Information to Improve Imaging

6.1 Introduction

The investigations described in Chapter 5 demonstrated that a 2D WEPL distribution of a balsa wood phantom could be measured using a compact Hybrid approach to pCT. Further investigations using a Perspex phantom which was not symmetric about 360° emphasised limitations to the technique. The apparent merging in the obtained images of the higher WEPL measurements originating from higher density regions of the Perspex phantom was observed, giving inaccurate structural information on a 2D radiograph. It should be noted that full 3D reconstruction, using a back projection then filtering algorithm [87] which takes into account individual proton paths within the phantom, may still produce an image showing more accurate structural information.

Full 3D reconstruction is the goal of proton imaging, but a 2D radiograph offers the potential for fast confirmation of patient position when on the couch, without an additional cone-beam CT system in a proton treatment facility. The 2D radiograph must therefore be as accurate as possible for the measurement of the position and WEPL of

internal structures within a patient (or for these studies, a phantom). A discrepancy in the magnitude of the measured WEPL of the Perspex insert in the balsa phantom using the Hybrid Approach was still observed despite the 360° symmetry.

The effect which contributes most to these observed discrepancies is expected to be the scattering of the protons within higher density regions. This scatter results in an imperfect location of the measured WEPL and a final image with a broadened high density region. When two high density regions are close together, their apparent merging can then occur in the image.

Single particle tracking is performed before and after the phantom when performing pCT, which allows accurate position and angular information of the protons to be measured. Consideration of parameters relating to the scattering of the protons offers additional information, which when combined with the energy measurement, could improve the positional accuracy of the internal structure of the phantom.

The analysis outlined in this chapter initially uses scattering theory to model the expected scatter occurring within the phantom. This results in an image which is more truly representative of that which is measurable through the Hybrid approach. Through this analysis, it was possible to separate and examine the competing effects of energy loss and scattering.

The second examination discussed is of a scattering only approach to pCT, which requires the trackers and no RERD, to measure the WEPL of each proton through a phantom. The same simulated and experimental data produced for the Hybrid Approach analysis is processed using the scattering algorithms described in this chapter to produce 2D radiographs, with very promising results. Experimental data is processed further with a simple 3D reconstruction algorithm to produce a pCT using this new approach. The

resultant pCT, along with the radiographs, are finally compared with an experimentally obtained x-ray CT (xCT).

6.2 Scattering Theory

The scattering of a proton through a material of thickness, z , is schematically shown in Figure 6.1 with the proton projected onto a plane.

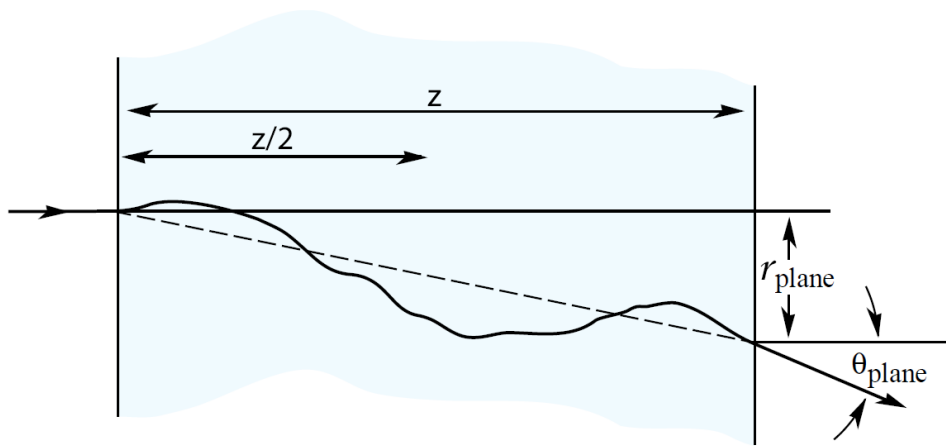


Figure 6.1: A schematic representation of the scattering of a proton through a material of thickness, z . The r_{plane} and θ_{plane} parameters represent the distance from entry and the exit angle, projected onto the x or y planes (x and y plane projections are equivalent) [42].

The statistical nature of proton scattering through small angles means that a proton which enters a material will exit at a position displaced by r in the (x,y) plane. The projection of this displacement onto the x and y planes can then be represented by $r_{plane,x}$ and $r_{plane,y}$ respectively. Projection onto either the x or y planes are equivalent as the scattering is symmetric, so the subscript for the axis designation is omitted for simplicity. The relation between these parameters can be represented as

$$r^2 = r_{plane,x}^2 + r_{plane,y}^2 . \quad (6.1)$$

The scattering angle, θ_{plane} , defined as the angle of the proton as it exits the material relative to the normal to the surface, can be approximated as a Gaussian distribution for the central 98% of proton scatters [42]. The complete distribution has larger tails than those in a Gaussian distribution due to protons scattering through large angles. For the purposes of pCT, and the use of silicon strip trackers, the protons which undergo large angle scatters will likely be lost from the system or be unsuccessfully reconstructed (through various cuts applied during reconstruction). It is therefore appropriate to consider the Gaussian approximation for this application.

The presence of two trackers both before and after the material means the proton entry and exit positions of the material can be measured and used to measure r_{plane} . The outgoing trackers can also measure the scattering angle, θ_{plane} .

In 3D space, the angle between the scattered proton and the normal to the surface is defined as [42]

$$\theta_{space}^2 = \theta_{plane,x}^2 + \theta_{plane,y}^2 . \quad (6.2)$$

The rms width of the Gaussian approximation of the plane projected scattering angle has been developed by Highland [88], and further by Lynch & Dahl [89]. It should be noted that there are variations in unit conventions and misprints within these papers, which has been noted to cause confusion [90] [91]. Units for this equation are therefore explicitly stated for clarity. The width of the distribution, in radians, is given by the equation [89]

$$\theta_{plane}^{rms} = \frac{13.6MeV}{\beta cp} q \sqrt{\frac{z\rho}{X_0}} \left[1 + 0.038 \ln\left(\frac{z\rho q^2}{X_0\beta^2}\right) \right] , \quad (6.3)$$

where p , βc and q are the momentum [MeV/c], velocity and charge number of the incident particle, and z , ρ and X_0 are the thickness [cm], density [gcm⁻³], and radiation length

[gcm^{-2}] of the medium traversed. The rms width of the Gaussian approximation for the separation of the proton from its initial entry position can also be represented by [42]

$$r_{plane}^{rms} = \frac{1}{\sqrt{3}} z \theta_{plane}^{rms} . \quad (6.4)$$

6.3 Modelling the Scatter

6.3.1 Outline

Both the balsa phantom and Perspex phantom had known internal geometries and materials. This allowed for the calculation of the geometric WEPL as a function of position. The 2D distribution of the geometric WEPL of the balsa phantom is shown in Figure 6.2a, binned in $200\mu\text{m}$ pixels. The 2D distribution of the geometric WEPL of the Perspex phantom is similarly shown in Figures 6.3a and 6.4a, for 0° and 90° rotations respectively, binned in $200\mu\text{m}$ pixels.

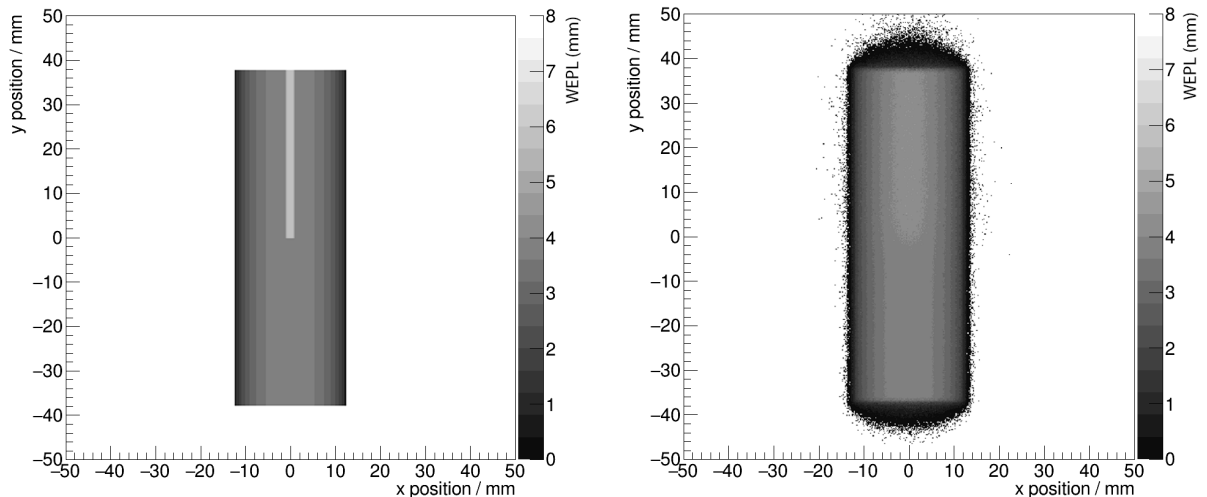
The consideration of the scattering theory of protons using the geometric WEPL allowed for the expected distortion of the simulated and experimental distributions to be modelled. The distortion in the image was primarily of the form of broadened high density regions, reduced WEPL measurements at the maxima, and changes to the position of high density regions.

6.3.2 Scattering Model Process

The rms width of the angular scatter, θ_{plane}^{rms} , and separation, r_{plane}^{rms} , were calculated using Equations 6.3 and 6.4 respectively for each pixel in the 2D distributions.

A Gaussian distribution with a standard deviation of r_{plane}^{rms} was assigned to each pixel according to its geometric WEPL value. The WEPL of the pixel was then binned in a pixel of a second histogram (referred to as the “scattered” histogram). The position of the pixel for binning in the scattered histogram is translated by the distance determined from a random sampling of the Gaussian distribution defined by r_{plane}^{rms} in both x and y dimensions. This sampling was repeated 100 times for each pixel and the number of protons in each pixel of the scattered histogram recorded. This scattered histogram was then averaged using the number of protons in each pixel and the result shown in Figure 6.2b for the balsa phantom and Figures 6.3b and 6.4b for the Perspex phantom projections.

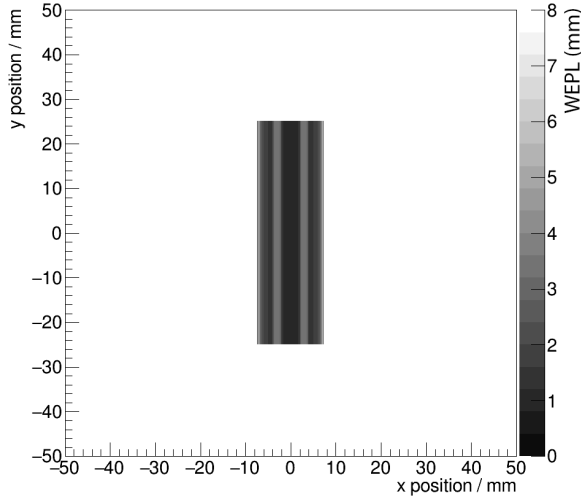
Profiles across the geometric and scattered distributions were calculated and shown in Figure 6.5 for the balsa phantom and Figures 6.6 and 6.7 for 0° and 90° rotations respectively of the Perspex phantom. Profiles across the top and bottom halves of the balsa phantom have been separately considered.



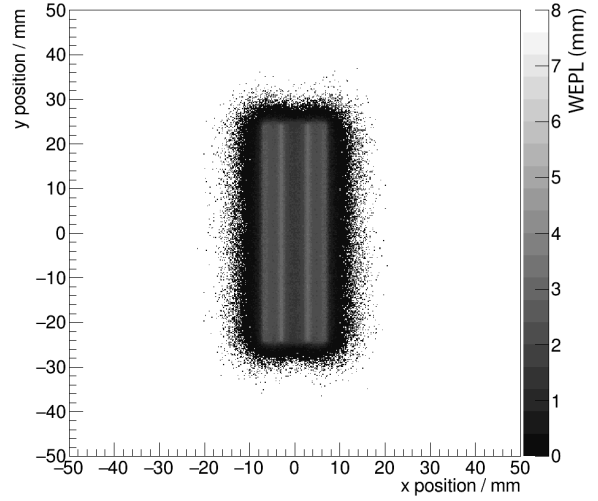
(a) Geometric WEPL.

(b) Scattered geometric WEPL.

Figure 6.2: Distributions of the geometric WEPL as a function of position before (6.2a) and after (6.2b) considering the scattering of protons through the balsa phantom.

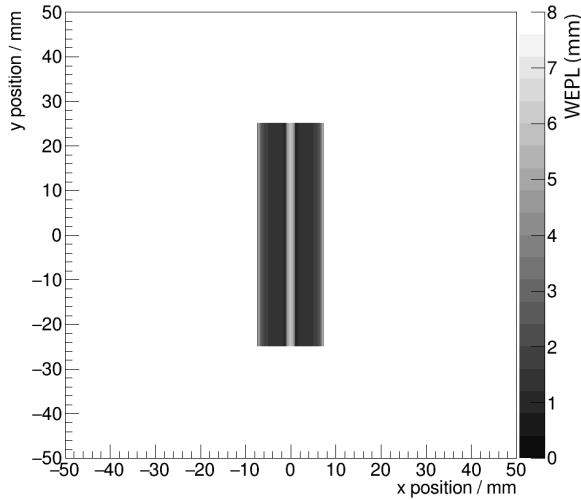


(a) Geometric WEPL.

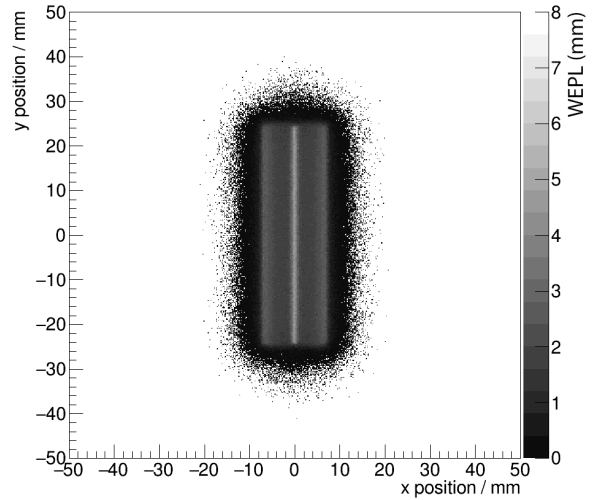


(b) Scattered geometric WEPL.

Figure 6.3: Distributions of the geometric WEPL as a function of position before (6.3a) and after (6.3b) considering the scattering of protons through the Perspex phantom.



(a) Geometric WEPL.



(b) Scattered geometric WEPL.

Figure 6.4: Distributions of the geometric WEPL as a function of position before (6.4a) and after (6.4b) considering the scattering of protons through the Perspex phantom. The phantom is rotated at 90° .

6.3.3 Scattering Model Results

Figure 6.6 shows a large reduction in the magnitude of the WEPL at the outermost walls of the Perspex phantom compared to the geometric projection. This is because the larger

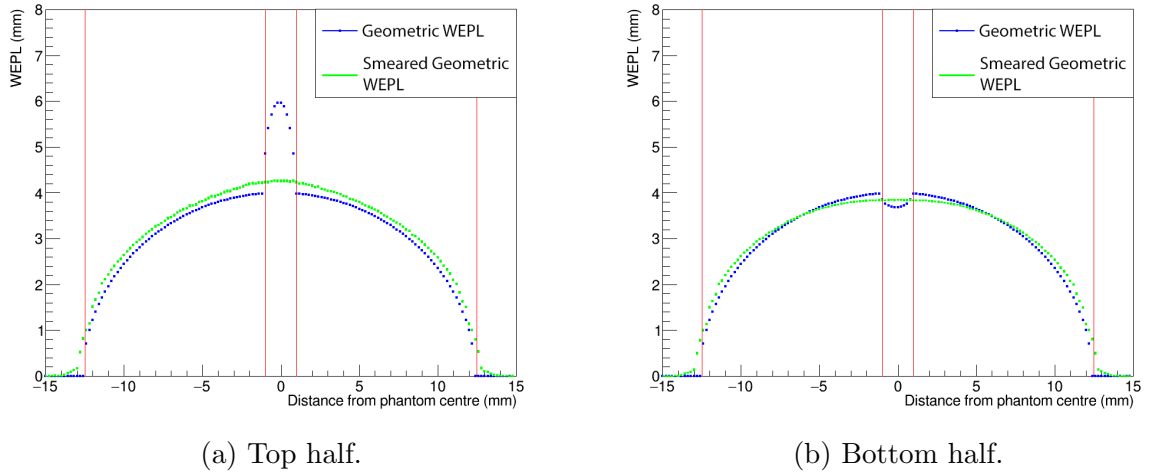


Figure 6.5: 1D profiles of the geometric WEPL as a function of position before and after considering the scattering of protons through the balsa phantom.

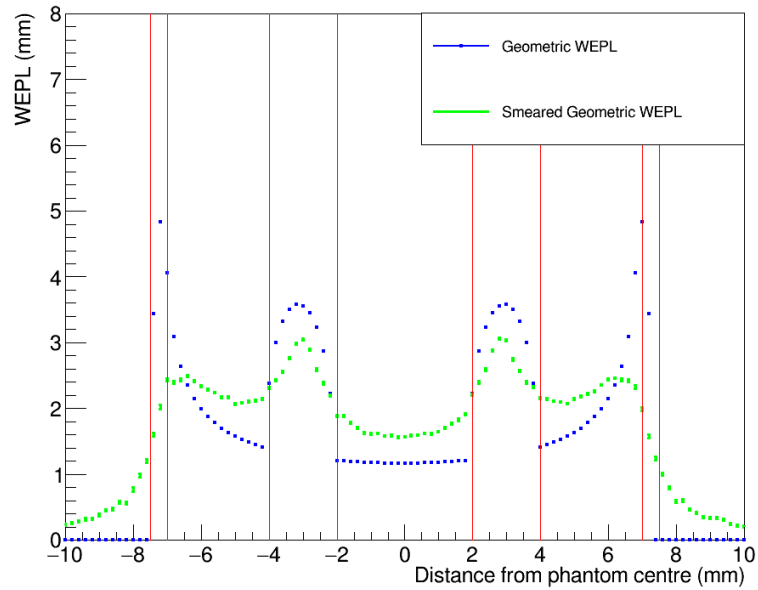


Figure 6.6: 1D profiles of the geometric WEPL as a function of position before and after considering the scattering of protons through the Perspex phantom.

thickness of Perspex contributes to an increased scatter of the protons. The thin wall also means that there are fewer protons passing through this higher thickness, which results in a smaller statistical contribution of the high WEPL to the scattered distribution. Conversely, the lower thickness results in a lower displacement of the protons from their original position within the phantom, so their magnitude is reduced less significantly.

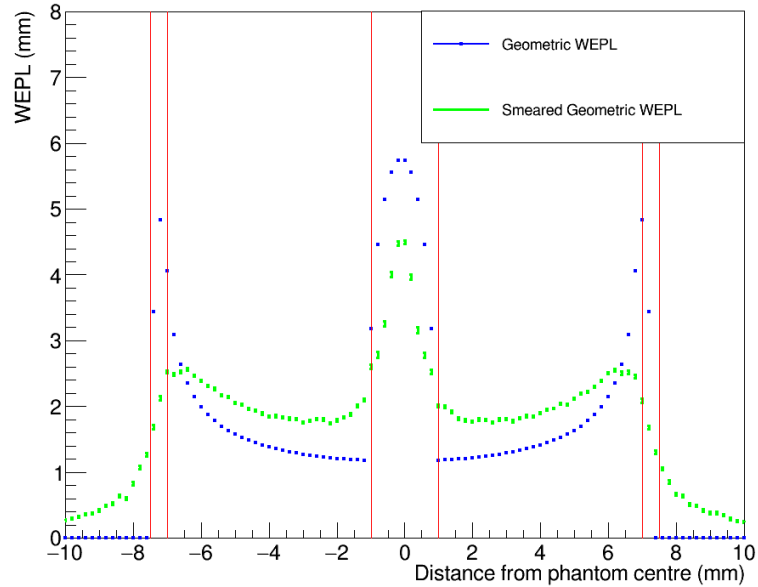


Figure 6.7: 1D profiles of the geometric WEPL as a function of position before and after considering the scattering of protons through the Perspex phantom. The phantom is rotated at 90° .

A reduction in the magnitude of the WEPL in the centre of the inserts is similarly observed with this consideration of the scatter. The additional scatter which these protons undergo in the insert results in them contributing to the measured WEPL outside of the insert position. Consequently, a broadening of the peak of the insert is observed. This is the effect that was observed most noticeably in Figure 5.16a, with the reduction in magnitude of the WEPL at the centre of the insert, and a broadening outside of the insert. This is therefore confirmation that the proton scatter is the origin of the broadening in the reconstructed image of the higher density regions.

The scattering model additionally confirms the rapid reduction of the measured WEPL for the walls of the Perspex phantom, in comparison to the reduction of the WEPL of the inserts. This is because the wall is very thin, and there is a high gradient in the geometric WEPL with distance from the wall. The thin wall means that few protons will actually travel through this maximum possible WEPL, based on the geometry, because

of their scatter within the Perspex. For example, many protons entering the phantom through the wall will scatter into the void inside the phantom. The WEPL which the protons travel is therefore significantly reduced, as a consequence of entering a very low density region. The inserts, however, have a smaller gradient in the geometric WEPL with distance from their maximum. There is consequently less difference between their traversed WEPL, and the WEPL expected from the geometry at the entry position.

6.4 A Tracking Only Approach to pCT

6.4.1 Motivation

The scattering model confirmed that the features in the radiographs produced from the Hybrid Approach were being distorted by the proton scatter. The deeper consideration of the theoretical description for the proton scatter led to the development of an alternative approach which used the scatter as the source of measurement to produce an image.

The trackers used as part of the pCT system are able to measure the scattering parameters which were used to apply the scattering in the described model. The measurement of these parameters, and subsequent plotting as 2D radiographs, showed a remarkable accuracy in the position of internal structure. The measurement of these parameters, and their associated radiographs, are described in more detail in this section.

A pCT image suitable for treatment planning is not straightforward to obtain from the scattering parameters, as the pCT requires a description of the stopping power or WEPL. A pCT image can be obtained [92], but it describes the “scattering power”, which is unsuitable by itself for proton treatment planning.

This section describes the process of measuring these parameters using the PRaVDA

trackers in the set-ups described in Chapter 5. The simulated and experimental data analysed are the same as those used for the Hybrid analysis to demonstrate how the structural information of the phantom can be resolved through using this new approach. A calibration curve is also obtained in order to relate the scattering parameters to a WEPL. It should be noted that this WEPL is different from the WEPL described previously. This WEPL describes the water equivalent path length required to scatter the proton, as opposed to that required to degrade the energy which has been discussed until this point. For clarity in this section, the scattering WEPL will have a separate notation, sWEPL, from the energy WEPL, which will maintain its reference as WEPL.

6.4.2 Measuring Scattering Parameters

This Scattering Approach requires two tracker units placed before and two after the phantom. The investigations for this study were performed with the same data sets used for the balsa phantom and Perspex phantom Hybrid approach studies. There was therefore a pixel sensor ($705\mu\text{m}$ of silicon) also in place behind the phantom and before Tracker 3. Its presence was ignored for the purpose of this analysis. It will however contribute to additional scatter of the protons, and so degrade any image obtained.

The protons were forward projected onto the phantom using their reconstructed positions in Trackers 1 and 2 to determine an x-y entry coordinate to the phantom. The protons were similarly back projected using reconstructed positions in Trackers 3 and 4 to determine an exit coordinate. A 2D histogram was filled with the calculated exit angle of the proton track when projected onto the x and y planes. This angle was binned in the bin corresponding to the proton entry position to the phantom. The scattering angle parameter, and the separation parameter between entry and exit positions when projected onto a plane are shown on the schematic diagram in Figure 6.8.

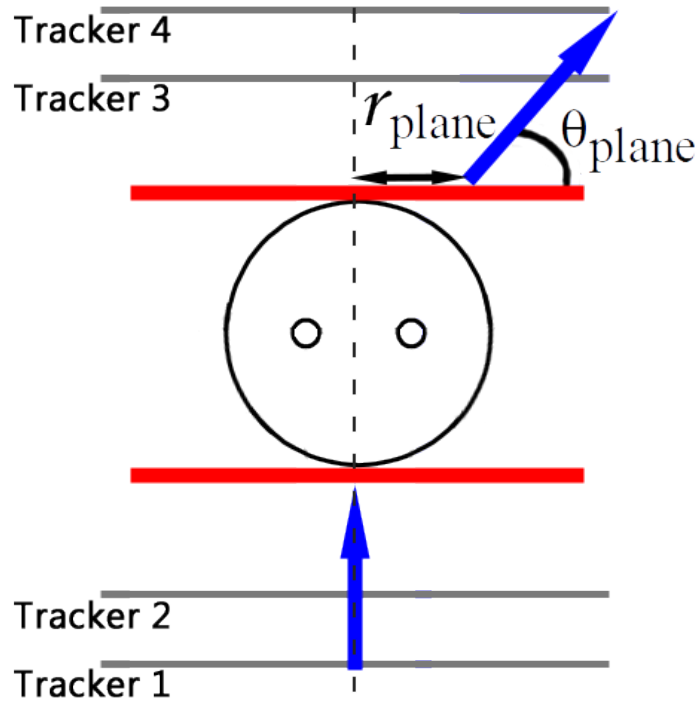


Figure 6.8: A schematic diagram showing the scattering parameters for measurement. The proton trajectories are shown in blue and the planes for projection shown in red. r_{plane} is the distance from the position of entry, and θ_{plane} is the angle of scatter, with both parameters projected onto either the x or y plane.

An entry plane was considered for the produced radiograph which ran tangential to the surface of the cylindrical body of the phantom closest to Tracker 2. This plane can be considered analogous to an x-ray radiograph (with the same initial beam direction), where the transmission of photons travelling directly through the phantom is measured. This imaging plane was segmented into a $200\mu\text{m} \times 200\mu\text{m}$ grid to correspond with the images obtained using the Hybrid Approach. Every pixel in this grid was assigned a 1D histogram to be filled with the plane projected exit angle of every proton which entered it. Each histogram was fitted with a Gaussian distribution once all protons had been processed. The mean and standard deviation of each bin then corresponds to the mean θ_{plane} , and the θ_{plane}^{rms} parameters respectively which were described in Section 6.2.

6.4.3 Scattering Calibration

The sWEPL, which describes the equivalent thickness of water required to broaden the scattering distribution by a given angle, was acquired through a calibration curve relating the θ_{plane}^{rms} parameter to the sWEPL. This calibration curve was produced through placement of Perspex sheets at the phantom position, with thicknesses ranging from 0mm to 6mm in 1mm increments. The average value of θ_{plane}^{rms} in a $1\text{cm} \times 1\text{cm}$ area in the centre of the radiograph was measured and assigned to its corresponding Perspex thickness.

The θ_{plane}^{rms} parameter can be approximated by the Highland formula (Equation 6.3) and is proportional to the square root of the material thickness. However, this relation does not represent the β dependence well for small thicknesses [42]. In a high β regime, the rate of energy loss in accordance with the Bethe-Bloch relation remains approximately constant. The stopping power, which is proportional to the rate of interaction, means that the rate of increase in scatter follows the rate of increase in stopping power. Therefore, in the regime where the stopping power remains approximately constant, the square root dependence with the material thickness, in accordance with Equation 6.3, holds true.

However, as the protons approach their range limit, the energy loss rate becomes increasingly dominant, resulting in the characteristic Bragg peak. The low energy of the Birmingham cyclotron (36MeV), in comparison to clinical facilities, means the protons used for these studies near the end of their range within the system. As the protons leave their near constant stopping power regime before the Bragg peak, the increased stopping power results in an increased scatter. The θ_{plane}^{rms} parameter therefore no longer follows the Highland relationship, and instead sharply increases. The variation in the proton energy with Perspex thickness is shown in Figure 6.9. The standard deviation of the proton energy is shown by the error bars. The increased rate of decreasing energy becomes apparent after approximately 4mm of Perspex, along with an increase in the

standard deviation of the energies.

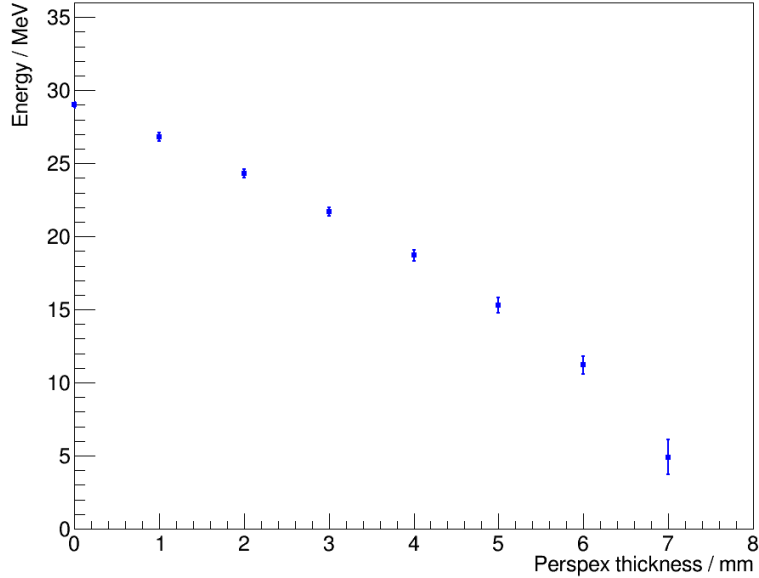


Figure 6.9: The energy of protons through the simulated system after a 36MeV beam has traversed 1.65mm of silicon (trackers and pixel sensor) and the specified thickness of Perspex. The error bars represent the standard deviation of the proton energy.

A good representation could therefore not be obtained for the measured θ_{plane}^{rms} with Perspex thickness, in accordance with the Highland formula, over the entire range of Perspex thicknesses. Instead, a third order polynomial was fitted which was found to be the best representation of the data. This fit matched the points which followed the square root dependence well, whilst also capturing those which deviated. The calibration curve obtained from simulation for both the balsa wood and Perspex phantom set-ups is shown in Figure 6.10. The small difference between the balsa wood and Perspex phantom set-ups was insufficient to alter the parameters of the calibration curves. The red curve represents the third order polynomial fit to the data.

The green curve in Figure 6.10 is a demonstration of the square root dependence with material thickness. The low β of these protons means the Highland relation does not fit well, but a square root dependence can be observed at lower Perspex thicknesses.

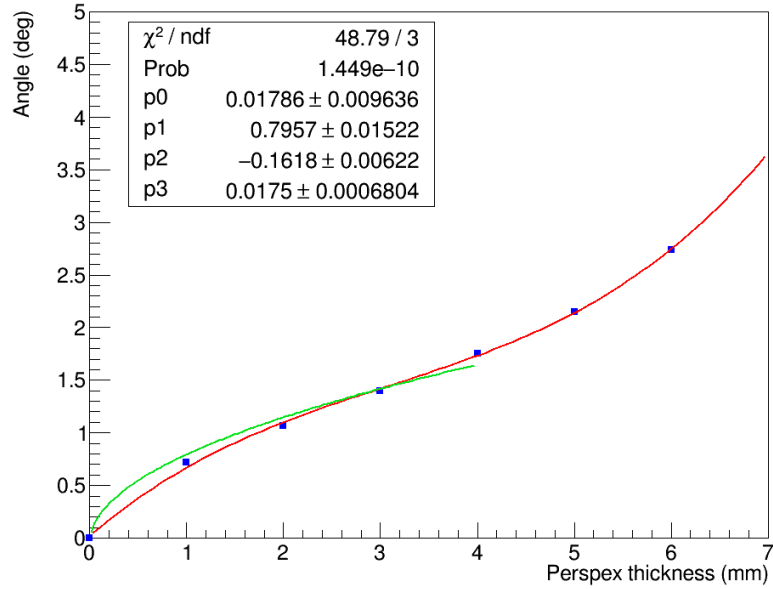


Figure 6.10: A calibration curve relating the thickness of Perspex required to scatter protons according to a Gaussian distribution with standard deviation of θ_{plane}^{rms} using simulated data in both the balsa wood and Perspex phantom set-ups. The red curve is a third order polynomial fit to the data. The green curve shows the square root dependence with Perspex thickness up to 4mm.

6.4.4 Balsa Phantom Results

The Scattering Approach was performed on the simulated and experimental balsa phantom data, and the results shown together for ease of comparison. The calibration curves for the simulated and experimental data sets are shown in Figures 6.10 and 6.11 respectively. Both calibration curves are fitted with third order polynomial fits, shown in red. Approximate square root dependencies are shown in green.

The 2D distributions of θ_{plane}^{rms} are shown in Figures 6.12a and 6.12b for the simulation and experimental data respectively. The respective 2D distributions of the sWEPL determined using their associated calibration curves are shown in Figures 6.13a and 6.13b. Profiles of the distributions across the top and bottom half of the sWEPL

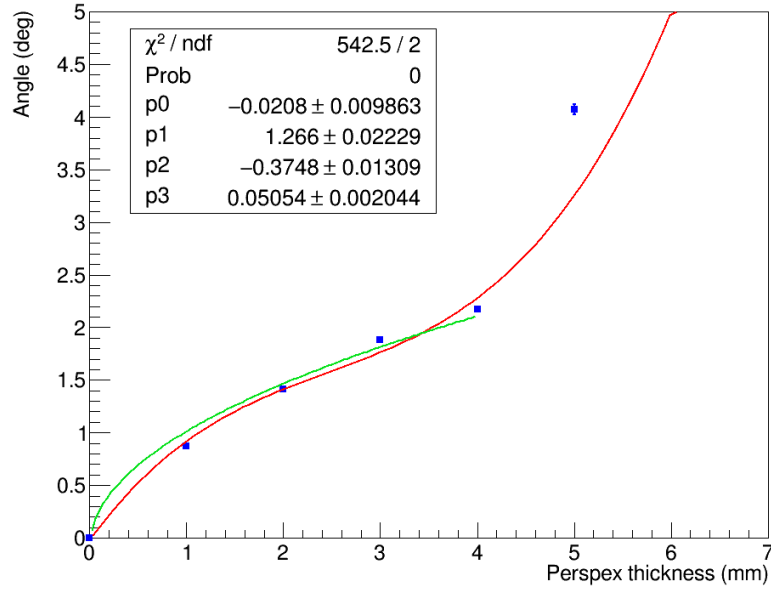


Figure 6.11: The calibration curve relating the thickness of Perspex required to scatter protons according to a Gaussian distribution with standard deviation of θ_{plane}^{rms} for experimental data. This set-up was for imaging the balsa phantom with the system configuration shown in Figure 5.12.

radiographs are shown in Figures 6.14 and 6.15 respectively.

The calibration curves from both simulation and experiment show similar results, most notably in the trend below 4mm of Perspex. Their dependence follows the expected proportionality with the square root of the material thickness in accordance with the Highland formula (Equation 6.3) in this region. This square root dependence is fitted to the data up to 4mm of Perspex, shown in green. There is a small increase in the θ_{plane}^{rms} for all Perspex thicknesses in the experimental calibration in comparison to the simulated result. In addition to this, the increase in gradient occurs at lower Perspex thickness in experiment compared to simulation.

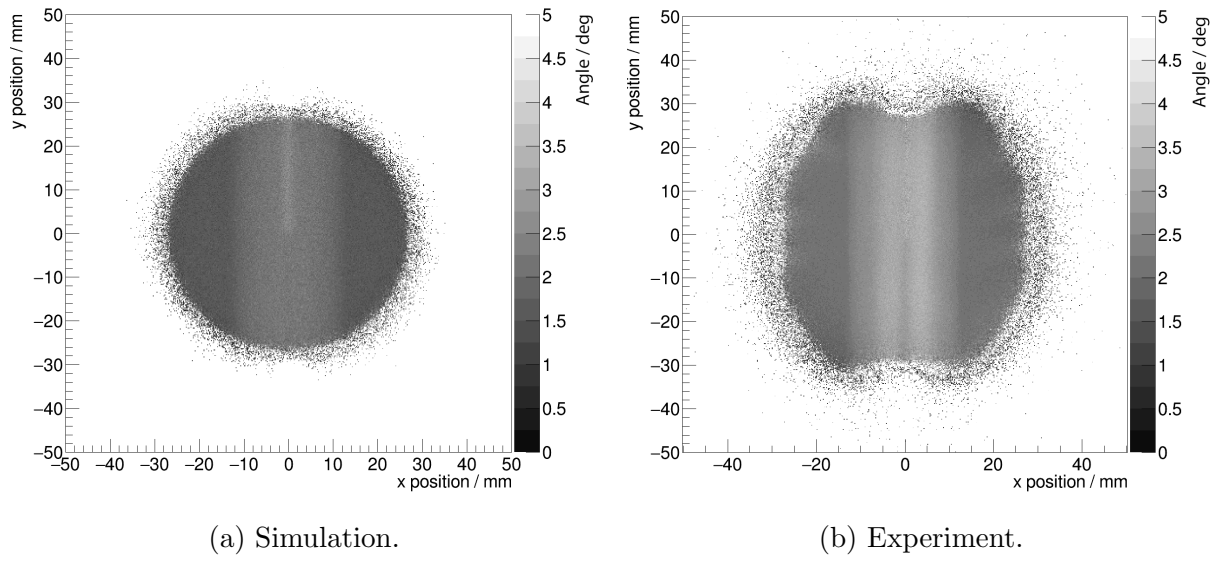


Figure 6.12: 2D distributions of θ_{plane}^{rms} of the balsa phantom for simulated and experimental data.

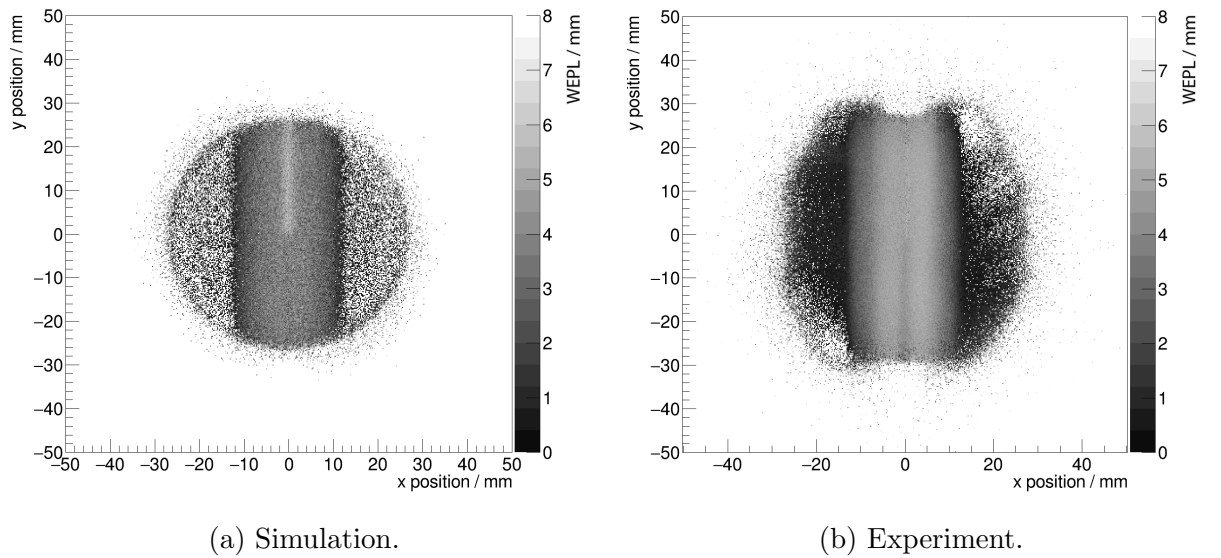
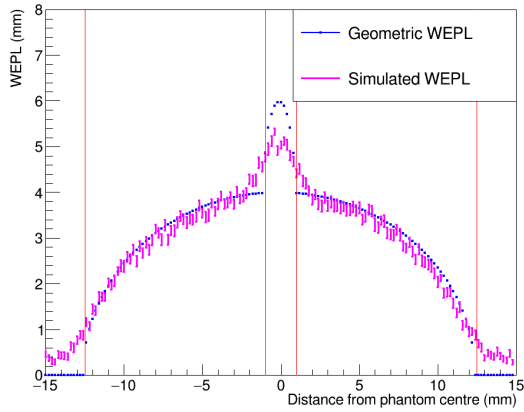
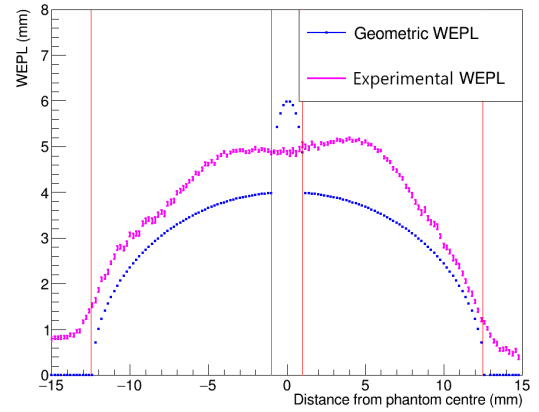


Figure 6.13: 2D distributions of the sWEPL of the balsa phantom for simulated and experimental data.

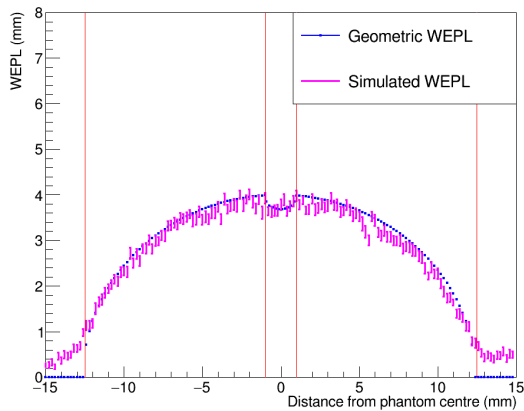


(a) Simulation.

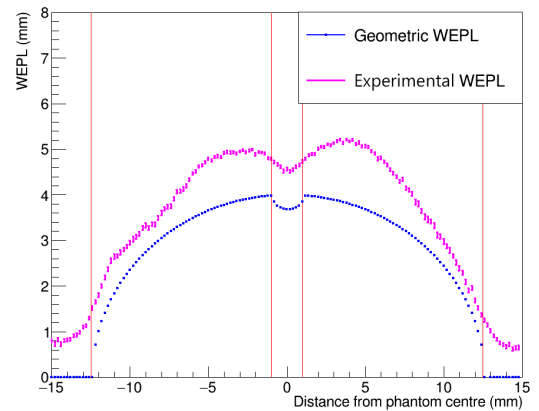


(b) Experiment.

Figure 6.14: 1D profiles across the sWEPL distributions in Figure 6.13 across the top half of the balsa phantom containing the Perspex insert.



(a) Simulation.



(b) Experiment.

Figure 6.15: 1D profiles across the sWEPL distributions in Figure 6.13 across the bottom half of the balsa phantom containing the air insert.

The increased θ_{plane}^{rms} value over the entire range of thicknesses is likely due to a slightly lower proton energy than the 36MeV simulated, which can be expected during realistic operation of the cyclotron. A lower incident proton energy would mean all θ_{plane}^{rms} values increase due to the increased frequency of interaction in accordance with the Bethe-Bloch relation. The point at which the gradient of the curve becomes increasingly positive would also move to a lower thickness as the protons would reach the Bragg peak earlier in the system. Both of these variations are observed in the experimental calibration, which suggests this difference originates from differing energies.

Examination of the profiles from simulation in Figures 6.14a and 6.15a shows very accurate mapping of the thickness of the phantom is possible within the balsa wood. There is little suggestion of the existence of the air insert in Figure 6.15a, but this is expected when considering its small size (2mm diameter) and the low density of the surrounding balsa wood. There is clear evidence of the presence of the Perspex insert in Figure 6.14a, with some small broadening occurring. The broadening is significantly reduced in comparison to that seen using the Hybrid Approach (Figure 5.16a), which highlights the advantage of the Scattering Approach. The extent of the broadening does not extend beyond 1mm from the edge of the insert which is a very positive result when considering the typical size of a voxel used in x-ray CT imaging is 1mm³.

The profiles from experiment are similar to those from simulation, but all values appear to be displaced positively in the y-axis. The simulation was run with a uniform density material for the balsa wood, but the displacement in the positive axis for the experimental data could be a result of a physical difference in the density of the true phantom material. The nature of wood also means that there could be density variations within the structure, which would also account for some variations within the sWEPL e.g. asymmetry in the x-axis. A radiograph obtained at the University Hospitals Birmingham NHS Foundation Trust [93] confirmed that the balsa wood had density variations, which

can be seen in Figure 6.16. The density variation is most obvious when considering the phantom symmetry about $x=0\text{mm}$. The main focus should therefore be on the general shape of the profiles, which follows closely up to a sWEPL of approximately 3.5mm.

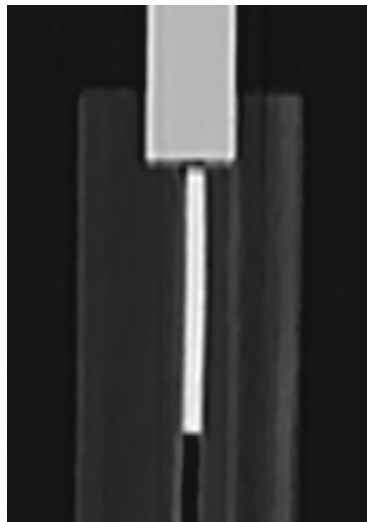


Figure 6.16: A radiograph of the balsa wood phantom obtained experimentally using x-rays. Differing densities within the wood can be seen.

There is a strong resemblance of the experimental 2D distributions of θ_{plane}^{rms} and sWEPL to those from simulation. The outer boundaries of the phantom can be clearly seen, along with the increase in thickness of the phantom when moving closer to 0mm on the x-axis. The existence of the air insert in the experimental distributions appears to be clearer than that from the simulation. This additional clarity is due to the increased contrast between the lower density air region and the neighbouring balsa wood, as a consequence of the fast change in gradient of the calibration curve at this thickness. The width of the trough at the air insert is promising in Figure 6.15b, being comparable to the width of the peak from simulation in Figure 6.14a, as it supports the observation of reduced broadening of regions in comparison to the Hybrid Approach.

The main difference between the simulated and experimental profiles are the sWEPL values above 3.5mm. This is where the protons are in the regime where they are not well represented by the Highland relationship. Their scatter increases at a faster rate in this

regime, as seen in the calibration curve with the increasing gradient, which leads to the sharp increase in sWEPL away from the geometric WEPL in the profiles. This deviation is most apparent when offsetting the geometric WEPL of the balsa wood to align it with the measured background scatter outside of the phantom. This offset geometric WEPL is shown in Figure 6.17 alongside the profiles across the top (Perspex insert) and bottom (air insert) halves of the phantom for direct comparison. It should be noted that the geometric WEPL data points have been removed in the region of the insert as the two profiles measure different materials.

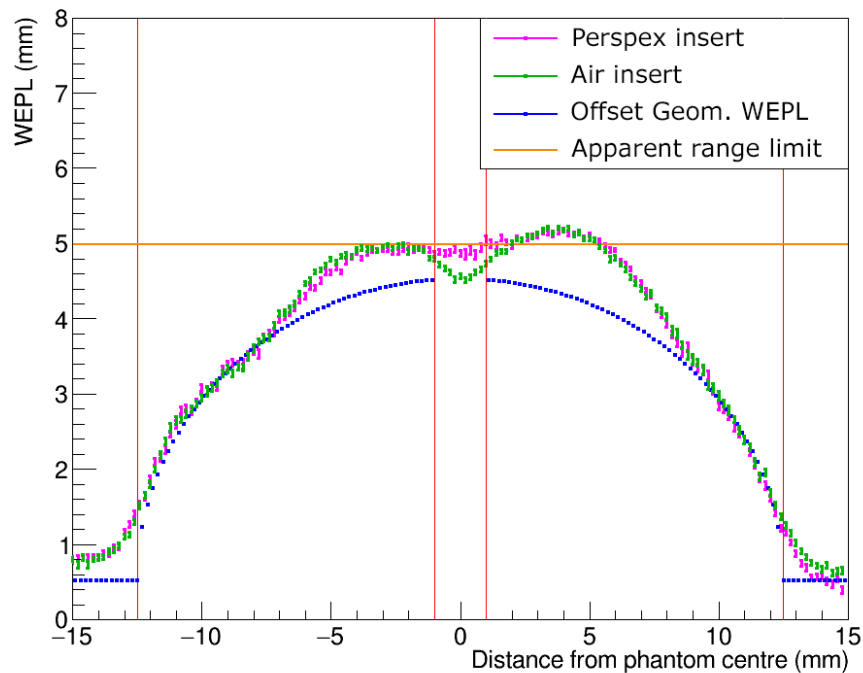


Figure 6.17: 1D profiles across the sWEPL distributions from the top and bottom halves of the balsa wood phantom (same as in Figures 6.14b and 6.15b) alongside an offset geometric WEPL in the balsa wood region. Note that the geometric WEPL data points have been removed at the insert location.

The profiles in the region of the balsa wood match closely, except at the insert position which is expected. The sWEPL, however, reaches an apparent 5mm limit and flattens in both of the profiles across the top and bottom halves of the phantom (except for the air insert, where a reduced amount of scatter and energy loss is occurring). The

apparent range limit of 5mm is marked by the orange line in Figure 6.17 as a guide. This flattening is a result of the protons reaching the end of their range within the system. Protons which are at the end of their range will stop within the system, and therefore not contribute to vary the distribution of the plane projected scattering angle. This is confirmed by the flatness of the distribution at this apparent range limit, otherwise an increased value of θ_{plane}^{rms} would still be measured for the Perspex insert. This is especially true because only a small change in θ_{plane}^{rms} is required to observe a large change in the sWEPL at this thickness. The protons reaching the end of their range was also evident during the Hybrid Approach studies, and was one of the motivations (described in Section 5.6.1) for designing the Perspex phantom.

6.4.5 Perspex Phantom Results

The calibration curves for converting θ_{plane}^{rms} to sWEPL for the simulated and experimental data in the Perspex phantom set-up are shown in Figures 6.10 and 6.18 respectively. 2D distributions of the θ_{plane}^{rms} parameter for the 0° and 90° rotated Perspex phantom are shown in Figures 6.19a and 6.19b respectively using simulated data. Conversion of the respective simulated θ_{plane}^{rms} distributions to sWEPL results in Figures 6.20a and 6.20b. Their corresponding 1D profiles are shown in Figures 6.21a and 6.21b.

Experimental 2D distributions of the θ_{plane}^{rms} parameter for the 0° and 90° rotated Perspex phantom are shown in Figures 6.22a and 6.22b respectively. Respective conversions to sWEPL using the calibration curve results in the experimental distributions shown in Figures 6.23a and 6.23b. Their corresponding 1D profiles are shown in Figures 6.24a and 6.24b.

The 2D profiles of θ_{plane}^{rms} and the sWEPL show exceptional clarity with the simulated data. The same distributions using the experimental data further confirm the achievable

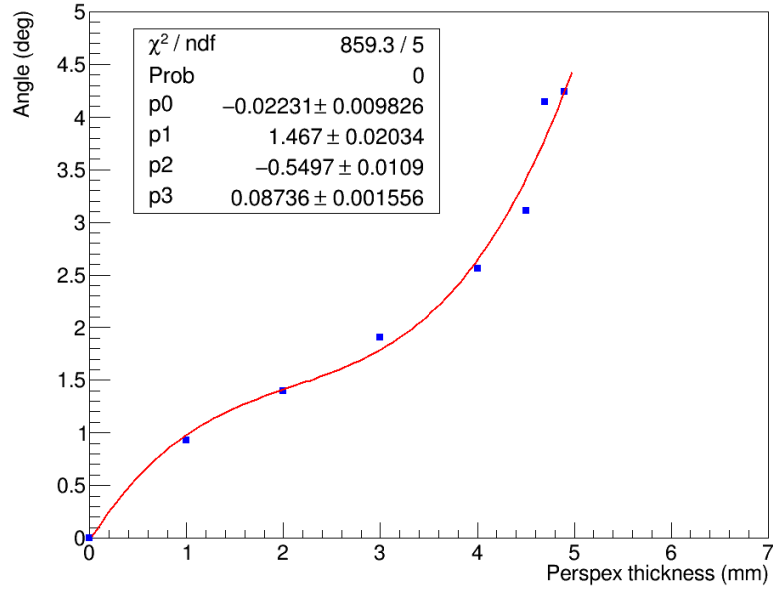


Figure 6.18: The calibration curve relating the thickness of Perspex required to scatter protons according to a Gaussian distribution with standard deviation of θ_{plane}^{rms} for experimental data. This set-up was for imaging the Perspex phantom with the system configuration shown in Figure 5.20.

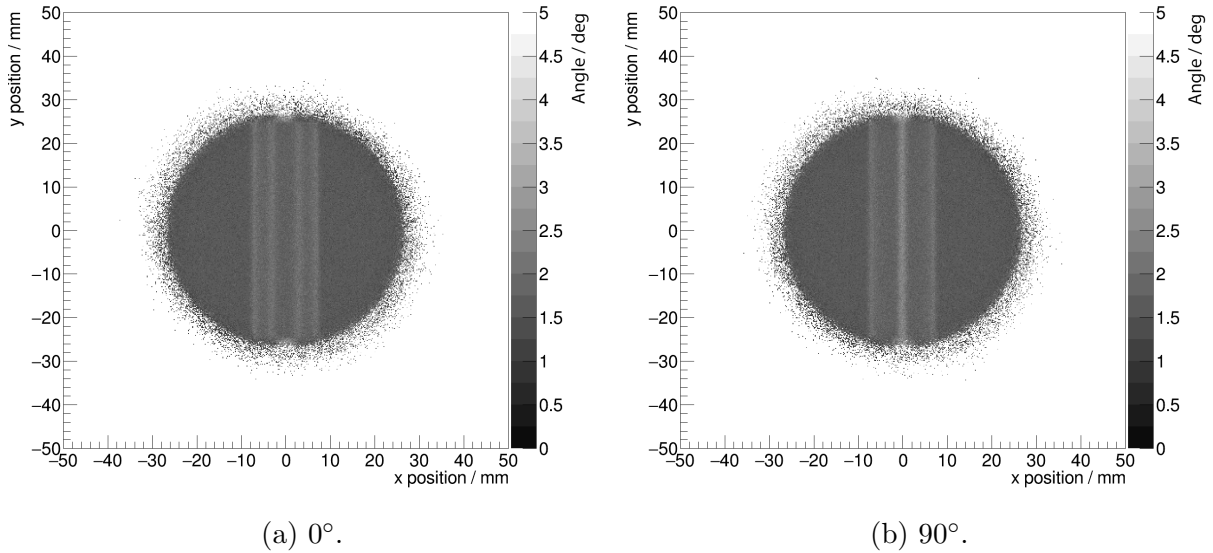


Figure 6.19: 2D distributions θ_{plane}^{rms} for 0° and 90° rotations of the Perspex phantom using simulated data.

clarity of these images using this technique. Inserts and the phantom wall are observable in all images.

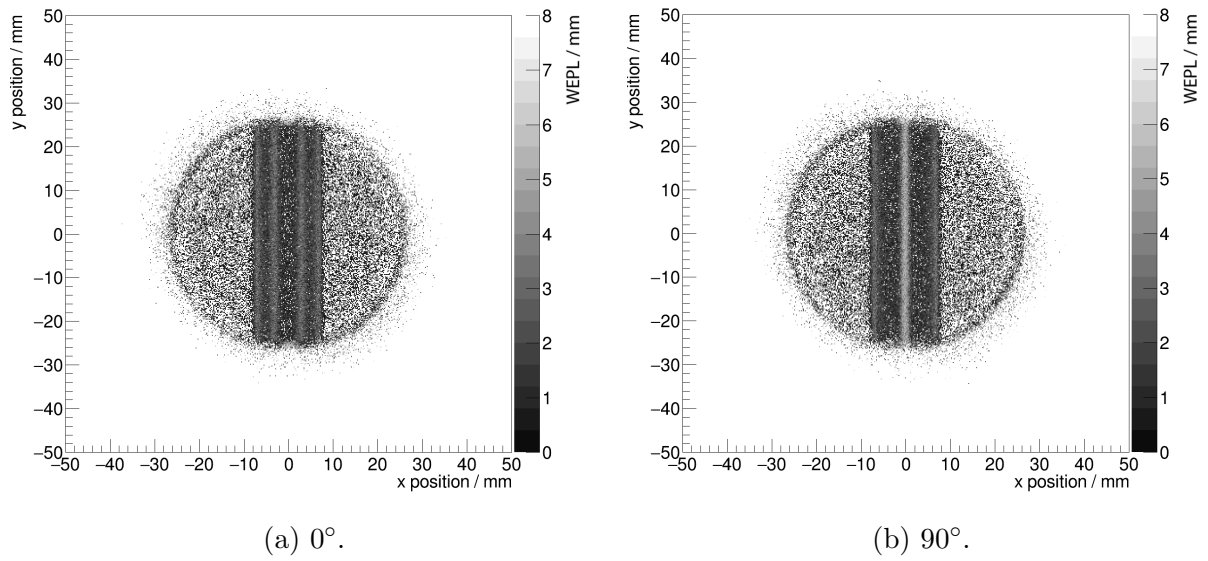


Figure 6.20: 2D distributions of the sWEPL measured using the θ_{plane}^{rms} parameter for 0° and 90° projections of the Perspex phantom using simulated data.

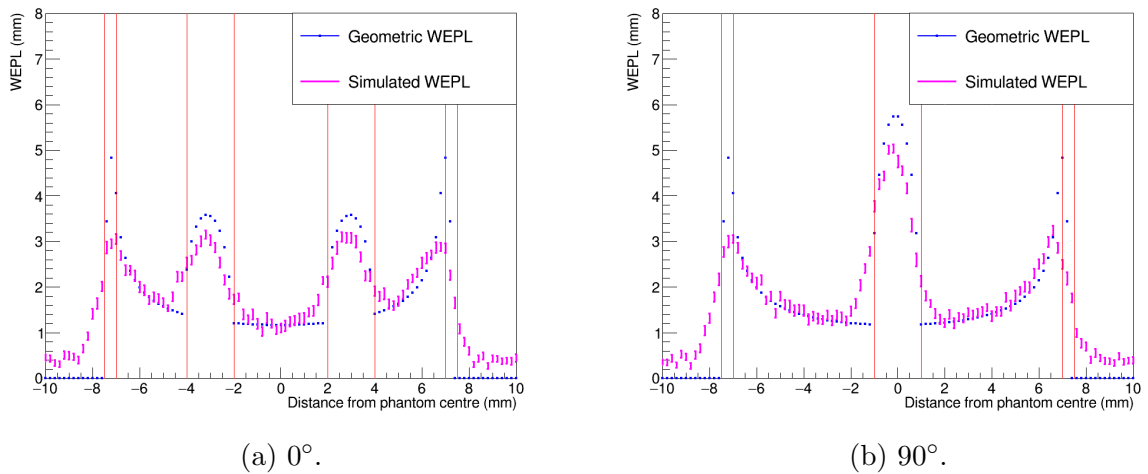


Figure 6.21: 1D profiles of the sWEPL in Figure 6.20 for 0° and 90° projections of the Perspex phantom using simulated data.

The rectangular white region in the 2D distributions for the experimental data (Figures 6.22 and 6.23 between 5mm and 10mm on the y-axis) is the top of the Perspex phantom. This 5mm height region is indicated in Figure 5.5a and is a solid piece of Perspex. The protons would stop in such a thickness of Perspex and so the distributions are as expected.

The simulated sWEPL profiles in Figure 6.21 show a significant improvement in clarity

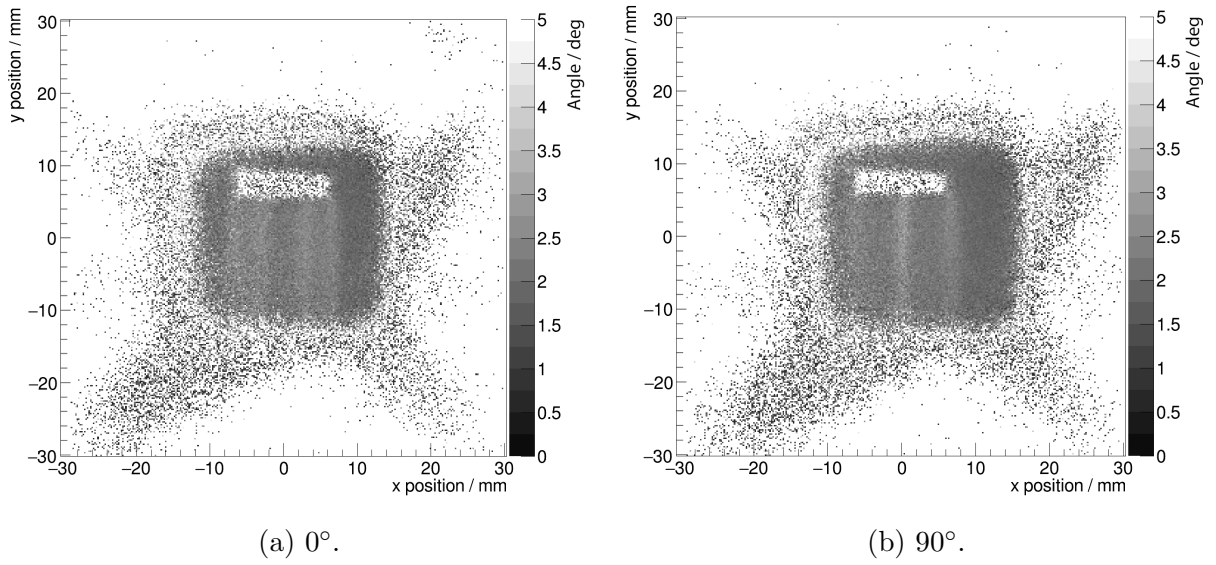


Figure 6.22: 2D distributions θ_{plane}^{rms} for 0° and 90° rotations of the Perspex phantom using experimental data.

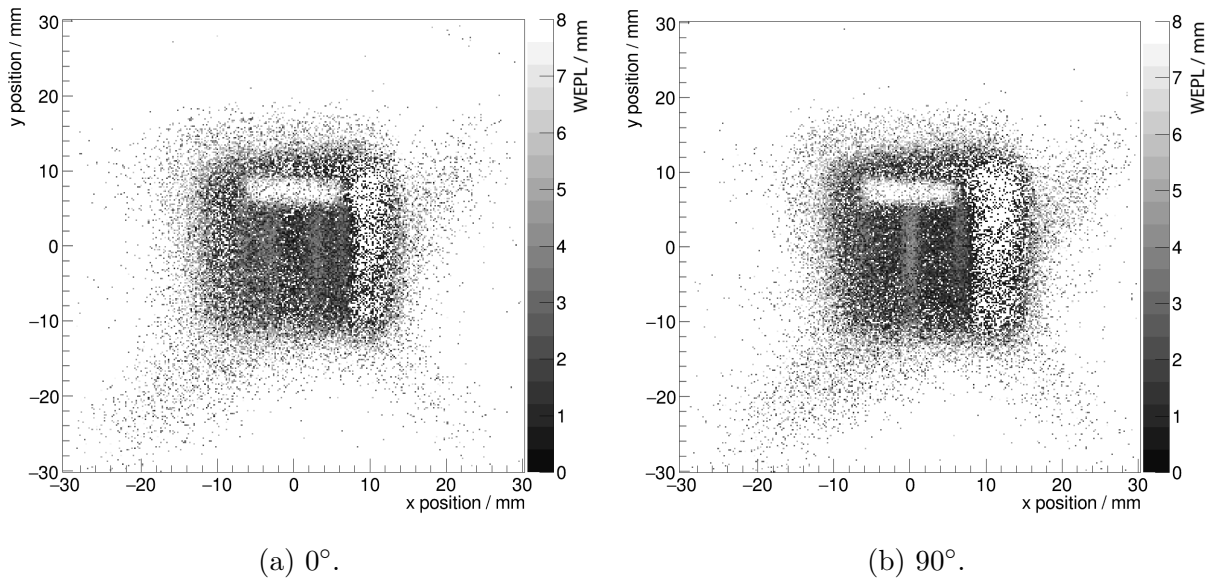


Figure 6.23: 2D distributions of the sWEPL measured using the θ_{plane}^{rms} parameter for 0° and 90° projections of the Perspex phantom using experimental data.

over those obtained from the Hybrid Approach. The apparent merging of the walls with the inserts in the image, as seen when using the Hybrid Approach, is no longer observed. The walls and inserts are clearly separated, and measured sWEPL values closely match that expected from the geometry.

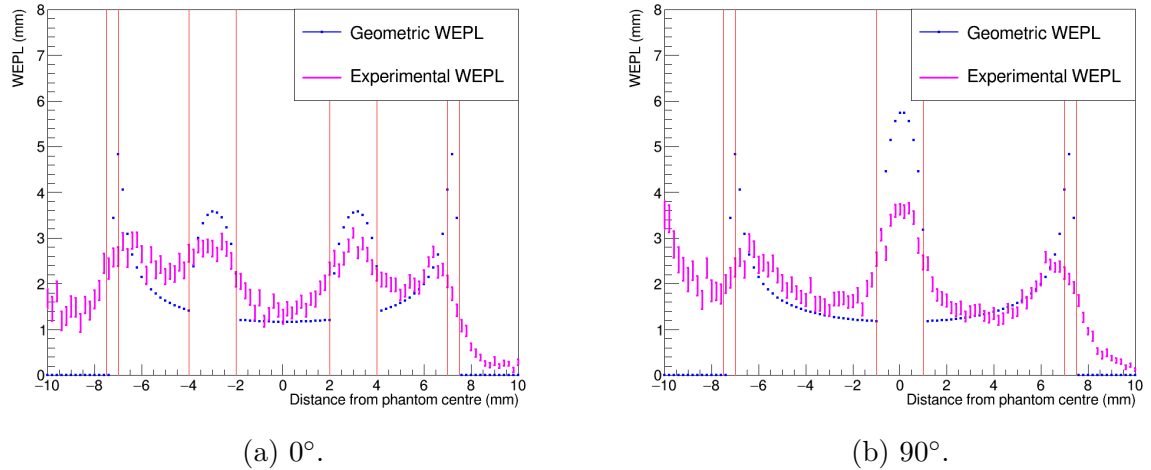


Figure 6.24: 1D profiles of the sWEPL in Figure 6.23 for 0° and 90° projections of the Perspex phantom using experimental data.

The experimental results confirm that the improvement in the quality of the images is an effect of using this new approach. Inserts and walls are correctly positioned, and the apparent merging of structures in the image does not appear to be an issue within the phantom. The profiles show that the sWEPL falls off sharply at the right hand side boundary of the phantom, as seen in simulation. The left hand side does not fall as sharply and remains above 1mm sWEPL in both 0° and 90° projections. This is an effect of the reduced number of protons at the left hand boundary due to the alignment of the beam. This can be seen most clearly in Figure 6.23b, where the phantom is positioned near the left hand side of the beam (the square grey region). This would be remedied through use of a larger beam, or with an increased scanning area if operating in a spot scanned facility.

6.4.6 Experimental pCT

The Scattering Approach demonstrated a superiority to the Hybrid Approach of producing clear 2D radiographs showing the internal structure of phantoms. 180

projections, from 0° to 180° in 1° steps, of the Perspex phantom were taken during the experimental data collection. The symmetry of the Perspex phantom meant that these same data sets could be used to cover the remaining 180° . A simple back projection algorithm was developed to produce a 3D image based on the obtained sWEPL measurements for each projection.

6.4.6.1 A Simple pCT Reconstruction Algorithm

The described Scattering Approach works differently from other pCT methods as it does not require a most likely path reconstruction for each proton. The most likely path modelling is critical when using individual proton WEPL measurements to correct for the scatter which occurs within the phantom. This scattering technique differs by taking the scattering into account when performing the WEPL measurement itself. It is envisaged that only a straight line path projection of the WEPL as a function of (x,y) position on a radiograph is required to perform 3D reconstruction.

The developed 3D reconstruction algorithm takes the sWEPL of each bin in (x,y) of a projection, and divides it by the number of bins contained in the straight line path through the phantom at the corresponding position. The bin size equates to the voxel size of the final 3D image, which was $200\mu\text{m}$ for this analysis. This gives an average sWEPL for each voxel along the given path.

The average sWEPL per voxel for a given path of a projection is added to every element of a 3D array along that path. This is performed for each projection, where the paths through the phantom are rotated by the corresponding projection angle.

6.4.6.2 pCT Image

A $200\mu\text{m}$ slice of the resultant 3D image of the Perspex phantom along its centre is shown in Figure 6.25a.

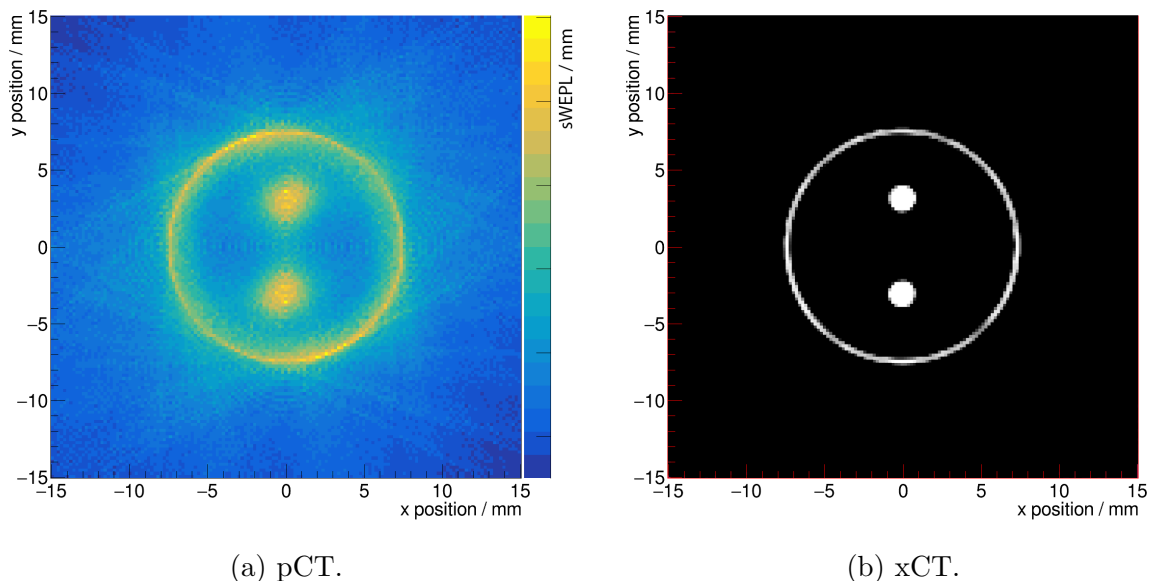


Figure 6.25: Axial slices from the experimentally obtained pCT and xCT images of the Perspex phantom.

The image demonstrates remarkable clarity of the structure within the phantom. The $500\mu\text{m}$ wall is clearly defined relative to the surrounding air. The inserts are accurately positioned, and no apparent merging of the structure is observed in the image. Such promising results from a very simplistic approach to the 3D reconstruction shows the significant potential for this technique.

A limitation of too few protons for each projection in the experimental data meant that an accurate measured value of the sWEPL for each voxel could not be determined. An increased number of protons per pixel in each projection would enable a more accurate measure of the θ_{plane}^{rms} parameter, and correspondingly, a more accurate measure of sWEPL.

The relative scale of the values in each voxel however remain a valuable result from this image. This image, unlike the 2D radiographs shown previously, contains information about the type of material of a given voxel. Each pixel in a radiograph only represents the SWEPL of the straight line path through the phantom; it does not contain information such as density. A profile across this 3D image is therefore expected to indicate the same voxel value for a given material, irrespective of its position within the phantom. This is discussed further in Section 6.4.6.3.

6.4.6.3 xCT

An x-ray CT (xCT) was obtained of the Perspex phantom at the University of Birmingham NHS Foundation Trust [93]. This image allowed for comparison with the obtained pCT of the Perspex phantom. Figures 6.26a and 6.26b show the x-ray radiographs of the 0° and 90° rotations of the Perspex phantom respectively. Phantom structure and accurate positioning is present in these images. The reconstructed voxel size in the xCT is $200\mu\text{m} \times 200\mu\text{m} \times 800\mu\text{m}$, with the $800\mu\text{m}$ being the thickness of the axial slices (y -axis in these images). This voxel size is smaller than that used clinically, which helps with a comparison with the obtained pCT. However, the $800\mu\text{m}$ slice thickness remains larger than the pCT's $200\mu\text{m}$.

A slice through the xCT of the Perspex phantom is shown in Figure 6.25b alongside the pCT using the Scattering Approach. The profile of the measured value of each voxel across the reconstructed 3D images in the pCT and xCT are shown in Figure 6.27. The voxel values have been normalised such that their relative values across the phantom within each image can be compared, as well as directly comparing the pCT and xCT with each other.

The red line in Figure 6.27 indicates the expected values for the profile across the



(a) 0° .



(b) 90° .

Figure 6.26: Reconstructed radiographs of the Perspex phantom from an experimental x-ray CT.

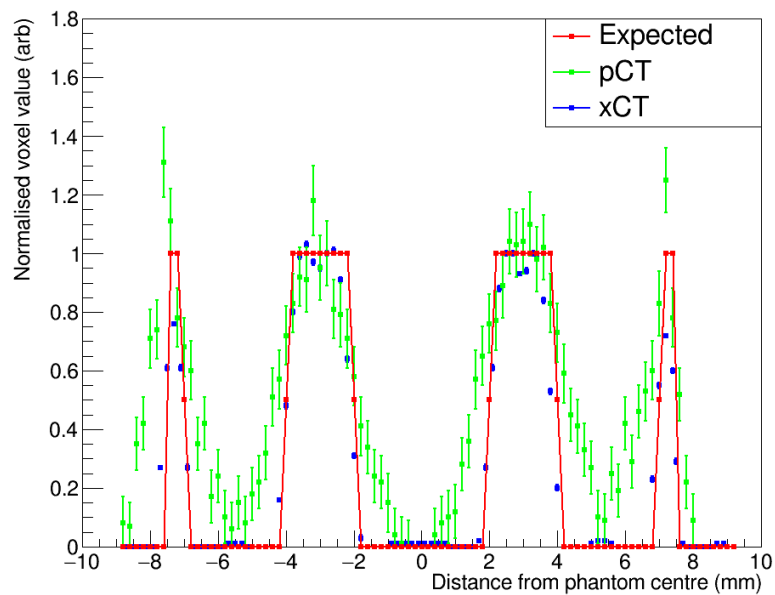


Figure 6.27: A profile of the pCT and xCT images shown in Figures 6.25a and 6.25b respectively along the central line of the phantom through both inserts. The red line indicates the expected relative values across the profile, with 1 being Perspex, and 0 being air.

phantom, normalised such that Perspex is 1, and air is 0. The blue curve from the xCT shows an improved contrast compared to the pCT, as the voxel values better capture the boundaries between Perspex and air. Some contribution to this improved contrast will be due to the thicker axial slice of the xCT. The largest discrepancy between the xCT

voxel values and the expected values are at the phantom wall, where the voxel values remain below 0.8. The pCT voxel values however appear to be much more comparable to the values measured within the inserts, as expected with them being made of the same material. This result indicates that the pCT obtained through the Scattering Approach could potentially offer a more accurate measure of the WEPL for small structures in comparison to xCT. More investigation would be required to confirm this.

The potential power of the Scattering Approach is also demonstrated through the manner in which the xCT was obtained. The xCT scanner was run in a mode which was not used clinically, allowing a higher resolution image to be obtained, though still not as high as the pCT. The scan was performed after recommissioning the xCT scanner with the latest reconstruction software. All images shown were also the best which could be obtained, with optimisation performed by an experienced operator of the scanner.

6.5 Conclusions

The multiple Coulomb scattering which occurs as protons traverse a phantom is a complex challenge for 3D reconstruction. This chapter outlined a study which considered the contribution to the limited spatial resolution of radiographs obtained during the Hybrid Approach investigations (discussed in Chapter 5) due to the scattering. The study allowed the effects from scattering to be examined separately from those of increased energy loss rate as the proton slows. The scattering was identified as the cause of the reduced spatial resolution in the radiographs when using the Hybrid Approach, which was most obvious in the apparent merging of structures within the phantom.

The limitations of the Hybrid Approach, most notably in the area of proton radiography, emphasised the extensive impact of proton scattering on measured images. A new

approach was therefore developed, referred to as the Scattering Approach, which used the scattering of the protons to measure the WEPL within a phantom.

The Scattering Approach, if it continues to prove successful in its development following such promising results, offers significant advantages over “traditional” proton CT systems which have been developed by groups to date. Firstly, the size of the system is reduced to require only upstream and downstream trackers. These devices can be made to be compact, with minimal effect on the beam, so can be envisioned to be mounted on the rotating gantry without too much difficulty. Secondly, the necessity of an energy measuring device is negated as a measurement of the energy of the protons is no longer required. This helps with the design of the pCT system as developing an energy measuring device with fast enough readout and capability of resolving multiple protons per frame has proven to be a significant challenge.

The Scattering Approach has been demonstrated to show clear structural detail for a small Perspex phantom using simulated data. Experimental data using a 36MeV proton beam on the Birmingham MC40 cyclotron confirmed the capability of the technique to resolve internal structure of the phantom, including a $500\mu\text{m}$ thick wall, in a radiograph. Furthering this success was the reconstruction of a 3D image using a simple back projection algorithm using this experimental data. The 3D image was reconstructed on a $200\mu\text{m}$ scale, 5 times smaller than typical clinical x-ray CT images, showing clear and accurately positioned structures.

An x-ray CT image was obtained for the Perspex phantom to allow direct comparison between the relative voxel values of the xCT and pCT. The xCT appeared to show improved contrast when compared with the pCT, but did not capture the expected value at the phantom walls. The pCT, despite having a reduced contrast, resulted in voxel values which better matched those expected at the phantom walls.

Further work is required, but these initial investigations prove to be very promising. The scalability of this technique with energy is one such investigation which is required. The increased energy on a clinical beam would result in a reduced amount of scatter, but would also be compensated by the increased scatter from larger thicknesses of material in the imaged phantom. The exact correlation between these effects therefore needs examination.

Another area of investigation is in how well the derived WEPL based on scattering, referred to as the sWEPL in this chapter, correlates to the WEPL derived from energy measurements. The separate designation of sWEPL was used in this chapter to make clear that their correlation is not sufficiently known to say they are the same. Treatment planning using pCT requires knowledge of the WEPL of the tissues in the patient to derive where the protons of a specific energy would stop. It is therefore critical to know accurately how sWEPL relates to the WEPL to describe how energy is lost through the patient.

The third key continuation of the studies for this technique is in the 3D reconstruction algorithm. The reconstruction algorithm developed performs a simple straight line back projection at each angle. The methodology of the Scattering Approach means that a straight line projection should be sufficient, instead of requiring a most likely path estimation for individual protons. However, developments to help improve the level of noise, and reduce artifacts in the final image would help with the image quality and accuracy. Techniques such as those developed for x-ray CT are expected to help here as they follow a similar straight line back projection approach to the reconstruction.

Chapter 7

Conclusions and Outlook

Imaging using x-ray CT, with conversion to proton stopping power for proton treatment planning, introduces a 3.5% uncertainty on the proton range. This uncertainty originating from the conversion of Hounsfield Units to proton stopping powers may be removed if a proton CT device is developed, which is suitable for a clinical environment. The development of a suitable device given the constraints of clinical facilities is not trivial, and has not yet been implemented in the clinic.

The work described here outlined studies for the optimisation and prototyping of a practical pCT device. The devices discussed included silicon strip tracking detectors for individual proton tracking. A study was performed which optimised the design of these trackers by varying the silicon strip pitch and silicon thickness in a Geant4 simulation. The optimisation of the devices was based on the achievable position and tracking resolutions. It was found that there was no improvement to the tracking resolution of the distal trackers measuring the outgoing proton trajectory between $50\mu\text{m}$, $90.8\mu\text{m}$ and $200\mu\text{m}$ strip pitch. A small improvement was observed by reducing the silicon thickness from $150\mu\text{m}$ to $100\mu\text{m}$, but was considered to be insufficient to justify the increased manufacturing cost of the silicon, reduction in structural integrity of the device, and increased data output. Optimal design parameters were concluded to be a $200\mu\text{m}$ strip

pitch and a $100\mu\text{m}$ thickness.

One of the main challenges of designing a practical pCT system is the requirement for a suitably small but accurate Residual Energy Range Detector (RERD). The device is required to measure multiple protons per readout frame, over a small area (typically a 6mm diameter spot), with energies up to 245MeV. This challenge has been in obtaining a sufficiently fast and segmented energy measuring device, or a small enough range measuring device.

The Hybrid Approach described here involved using a single layer of silicon pixels to measure the average signal per proton as a function of position in the device. All protons which passed through a given pixel were then assigned to have traveled the specified Water Equivalent Path Length (WEPL), derived from a calibration curve relating the average signal to the WEPL. 2D radiographs were produced of the WEPL for the Hybrid Approach both experimentally, using the MC40 cyclotron in Birmingham, and using simulation. Results were promising, but limitations were observed to the achievable spatial resolution of internal structures due to the scattering of the protons within the phantoms.

These studies show that the Hybrid Approach, without a deeper consideration of the scattering, is insufficient for proton radiography. However, typical 3D reconstruction methods using protons involve a most likely path approximation through the phantom to model the scatter. These studies did not extend to the 3D reconstruction of the Hybrid Approach results. It is therefore not possible to rule out the potential of the Hybrid Approach for pCT. Analysis of the achievable stopping powers obtained using a suitable 3D reconstruction algorithm would be required to determine this.

A deeper consideration of the proton scatter was conducted during this work, which led

to the development of a novel approach to pCT which has not been previously discussed in literature. This approach uses the distribution of the plane projected proton scattering angle as a function of entry position of the phantom to construct an image. Examination of simulated and experimental data on the MC40 cyclotron showed remarkable positional accuracy in 2D radiographs, as well as accurately measured sWEPL (separately defined from the WEPL to distinguish it from the WEPL determined using energy measurements).

One of the key advantages of the Scattering Approach is that the pCT system only requires the trackers, and no RERD. This elimination of the RERD makes a clinically practical pCT system immediately more conceivable. Tracking technologies already exist with sufficient spatial resolution, readout rate, and compactness to be mounted on a gantry. The studies described in Chapter 4 also help to bring such technology to the clinic.

The algorithms developed for the Scattering Approach measure a parameter which is dependent on the entry position to the phantom. Their paths can then be modelled as parallel to the initial beam direction when reconstructing in 3D. This makes the 3D reconstruction for the Scattering Approach more analogous to an x-ray CT reconstruction algorithm, which measures the transmission of x-ray on a parallel path through the patient. As a result, the 3D reconstruction algorithms are expected to be more simplistic, again, being more analogous to x-ray CT reconstruction techniques.

A very simplistic 3D reconstruction algorithm was developed which back projected the 2D radiographs at each angle. Reconstruction of experimental data collected on the MC40 cyclotron showed exceptional positional accuracy of the internal structure of a 15mm diameter cylindrical phantom. The phantom was hollow, with $500\mu\text{m}$ walls, and contained two 2mm diameter inserts, located 6mm apart. The algorithm, which reconstructed in 3D on a $200\mu\text{m}$ scale clearly showed this thin phantom wall. Consideration of typical clinical x-ray CT images being reconstructed with voxels on a

1mm scale shows how promising this technique could be.

An x-ray CT image was obtained of the Perspex phantom, which showed improved contrast between the air and Perspex inserts in comparison to the pCT. This is expected when considering the simplicity of the pCT reconstruction algorithm. Further development of the algorithm would likely improve the contrast. Improved voxel values were observed at the phantom walls in the case of the pCT in comparison to the xCT, which shows real promise for the technique.

The $200\mu\text{m}$ sized voxels demonstrated here, though better than clinical x-ray CT, is not the limit of this approach. The statistical nature of this approach, as it measures the standard deviation of the plane projected scattering angle, means that an increased number of protons for the image helps to reduce the uncertainty on the measured value. These scattering angles may be binned in a radiograph at any required scale, providing sufficient statistics are achieved to measure the standard deviation of the 1D histogram assigned to each bin. This approach therefore offers the potential of a variable spatial resolution with dose. For example, an improved resolution can be achieved by increasing the number of protons per projection, and with it the dose to the patient. Conversely, the dose to a patient can be reduced, at the cost of a larger voxel size.

Further studies are required for the Scattering Approach to examine its full potential. One such examination is in the 3D reconstruction algorithm, which due to the limitations of statistics in the experimental data meant that accurate voxel values could not be deduced. A deeper examination of the achievable WEPL (or stopping power) resolution can be completed with sufficient statistics, both in simulation and experiment. Techniques should also be implemented which are used in 3D reconstruction algorithms to reduce the noise and artifacts in the image.

The study with the most priority is how the technique scales with energy. A higher energy would result in less scatter of the protons, conceivably reducing the variation in the scatter, and impacting negatively on the WEPL measurement. However, at the higher proton energies of a clinic, larger phantoms (or patients) would be imaged. These larger thicknesses would therefore result in an increased amount of scatter. This means that the reduced scatter due to a higher energy may be compensated for by the increased thickness, but this remains to be examined in detail.

The work described regarding the Scattering Approach used the separate notation of sWEPL, in comparison to the WEPL notation used elsewhere. This is because the WEPL derived from this measurement describes the WEPL required to produce a specific standard deviation of the plane projected scattering angle. Treatment planning, however, predominantly requires a WEPL relating to energy loss (though scattering information is also advantageous). An examination of the correlation between the WEPL relating to energy loss and the sWEPL relating to scattering should therefore be conducted.

Bibliography

- [1] Vincent Van Gogh. *The Complete Letters of Vincent Van Gogh*. Vol.1. Thames and Hudson Ltd, 1978. ISBN:05002302110.
- [2] Cancer Research UK. Accessed January 2021. <https://www.cancerresearchuk.org/health-professional/cancer-statistics/mortality>.
- [3] National Cancer Research Institute. *Cancer research spend in the UK 2002-2011*. 2013.
- [4] Cancer Research UK. *Annual Report and Accounts 2018/2019*. 2019.
- [5] Cancer Research UK. Accessed January 2021. <https://www.cancerresearchuk.org/health-professional/cancer-statistics/survival>.
- [6] D.Hanahan, R.Weinberg. *Hallmarks of Cancer: The Next Generation*. Cell. Mar 4;144(5):646-74, 2011. doi:10.1016/j.cell.2011.02.013.
- [7] S.Elmore. *Apoptosis: a review of programmed cell death*. Toxicol Pathol. 35(4):495-516, 2007. doi:10.1080/01926230701320337.
- [8] T.H.Adair, J.P.Montani. *Angiogenesis*. San Rafael (CA): Morgan Claypool Life Sciences, 2010.
- [9] A.Armour, et al. *Walter and Miller's textbook of radiotherapy : radiation physics, therapy and oncology (7th Edition)*. Edinburgh : Churchill Livingstone, 2012. ISBN: 0443074860.

- [10] A.Barzilai, K.Yamamoto. *DNA damage responses to oxidative stress*. DNA Repair Vol.3:1109-1115, 2004. doi:10.1016/j.dnarep.2004.03.002.
- [11] J.Lundkvist, et al. *Proton therapy of cancer: potential clinical advantages and cost-effectiveness*. Acta Oncol. 44(8):850-861, 2005. doi:10.1080/02841860500341157.
- [12] Z.Kang, et al. *DNA Repair in Cancer*. Journal of Oncology. Volume 2019, Article ID 8676947, 2019. doi:10.1155/2019/8676947.
- [13] E.B.Podgorsak, et al. *Radiation Oncology Physics: A Handbook for Teachers and Students*. IAEA, 2005. ISBN:92-0-107304-6.
- [14] G.Knoll. *Radiation Detection and Measurement*. 3rd Edition, 2000. ISBN: 978-0-470-13148-0.
- [15] M.deBruin. *Glossary of terms used in nuclear analytical chemistry*. Pure and Applied Chemistry, Vol.54, Issue 8, 1982. doi:10.1351/pac198254081533.
- [16] R.D.Evans. *The Atomic Nucleus*. Tata McGraw-Hill Publishing Company Ltd. pp.712, 1955.
- [17] I.Y.Jo, et al. *Radiation Oncology: A Physicist's-Eye View*. Oncotarget. 8(2):3059-3063, 2008. doi:10.18632/oncotarget.13830.
- [18] N.Lee, et al. *Intensity-modulated radiation therapy in head and neck cancers: An update*. Head Neck, 29: 387-400, 2007. doi:10.1002/hed.20332.
- [19] T.C.Ling, et al. *Evaluation of normal tissue exposure in patients receiving radiotherapy for pancreatic cancer based on RTOG 0848*. Journal of Gastrointestinal Oncology. 6(2):108-114, 2015.
- [20] M.Peszynska-Piorun, et al. *Doses in organs at risk during head and neck radiotherapy using IMRT and 3D-CRT*. Radiol Oncol. 46(4):328-336, 2012. doi:10.2478/v10019-012-0050-y.

- [21] Proton Therapy Co-operative Group. Accessed January 2021. <https://www.ptcog.ch/index.php/facilities-in-operation>.
- [22] Proton Therapy Co-operative Group. Accessed January 2021. <https://www.ptcog.ch/index.php/facilities-under-construction>.
- [23] The Clatterbridge Cancer Centre NHS Foundation Trust. Accessed January 2021. <https://www.clatterbridgecc.nhs.uk/patients/treatment-and-support/proton-therapy>.
- [24] The Christie NHS Foundation Trust Proton Therapy Centre. Accessed January 2021. <https://www.christie.nhs.uk/patients-and-visitors/services/protons>.
- [25] University College London Hospitals NHS Foundation Trust Proton Therapy Centre. Accessed January 2021. <https://www.uclh.nhs.uk/our-services/find-service/cancer-services/proton-beam-therapy-pbt>.
- [26] U.W.Langner, et al. *Comparison of multi-institutional Varian ProBeam pencil beam scanning proton beam commissioning data*. J. Appl. Clin. Med. Phys. 18:3:96–107, 2017. doi:10.1002/acm2.12078.
- [27] W.D.Newhauser, R.Zhang. *The physics of proton therapy*. IOP. Physics in Medicine and Biology. 60:R155-R209, 2015. doi:10.1088/0031-9155/60/8/R155.
- [28] M.Goitein. *Radiation Oncology: A Physicist's-Eye View*. Springer, 2008. ISBN: 978-0-387-72645-8.
- [29] R.Marassi, F.Nobili. *MEASUREMENT METHODS - Structural and Chemical Properties: Transmission Electron Microscopy*. Encyclopedia of Electrochemical Power Sources, pp.769-789, 2009. ISBN:978-0-444-52745-5.
- [30] K.A.Olive, et al. *Review of Particle Physics*. Particle Data Group. Chin. Phys. C38., 2014. doi:10.1088/1674-1137/38/9/090001.

- [31] S.Agostinelli, et al. *Geant4: a simulation toolkit*. Nucl.Instrum.Meth.A. 506:250-303, 2003.
- [32] Markus Chamber. Accessed January 2021. <https://www.ptwdosimetry.com/en/products/advanced-markus-electron-chamber>.
- [33] V.A.Bashkirov, et al. *Novel scintillation detector design and performance for proton radiography and computed tomography*. Med. Phys. 43 (2), 2016. doi:10.1118/1.4939255.
- [34] H.E.S.Pettersen, et al. *Accuracy of parameterized proton range models; A comparison*. Radiation Physics and Chemistry, Volume 144, pg.295-297., 2018. doi:10.1016/j.radphyschem.2017.08.028.
- [35] W.Ulmer, E.Matsinos. *Theoretical methods for the calculation of Bragg curves and 3D distributions of proton beams*. Eur. Phys. J. Spec. Top. 190, 1–81, 2010. doi:10.1140/epjst/e2010-01335-7.
- [36] C.Greco, S.Wolden. *Current Status of Radiotherapy With Proton and Light Ion Beams*. Cancer:109(7):1227-38, 2007. doi:10.1002/cncr.22542.
- [37] C.Karger, P.Peschke. *RBE and related modeling in carbon-ion therapy*. Phys. Med. Biol. Vol.63 01TR02, 2017. doi:10.1088/1361-6560/aa9102.
- [38] T.Kamada, et al. *Carbon-Ion Radiotherapy: Principles, Practices, and Treatment Planning*. Springer, 2014. doi:10.1007/978-4-431-54457-9.
- [39] S.B.Curtis. *Calculated LET Distributions of Heavy Ion Beams*. Int. J. Radiation Oncology. Biol. Phys. Volume 3. pp.87-91, 1977. doi:10.1016/0360-3016(77)90232-2.
- [40] P.Fossati, et al. *Radiobiological issues in prospective carbon ion therapy trials*. Med Phys. 201845(11):e1096-e1110, 2018. doi:10.1002/mp.12506.

- [41] G.Lutz. *Semiconductor Radiation Detectors*. Springer-Verlag Berlin Heidelberg, 2007. doi:10.1007/978-3-540-71679-2.
- [42] M Tanabashi, et al. *The Review of Particle Physics - C33: Passage of Particles Through Matter*. Phys. Rev. D 98, 030001, 2018. doi:10.1103/PhysRevD.98.030001.
- [43] P.Allport. *Applications of silicon strip and pixel-based particle tracking detectors*. Nat Rev Phys 1, 567–576, 2019. doi:/10.1038/s42254-019-0081-z.
- [44] C.Argos. *A Silicon Strip Detector for the Phase II High Luminosity Upgrade of the ATLAS Detector at the Large Hadron Collider*. Valencia University. CERN-THESIS-2014-217, 2015. arXiv:1501.02903.
- [45] L.Rossi, O.Bruning et al. *High Luminosity Large Hadron Collider; A description for the European Strategy Preparatory Group*. CERN-ATS-2012-236, 2012.
- [46] J.P.Colinge, C.A.Colinge. *Physics of Semiconductor Devices*. Kluwer Academic Publishers, 2002. ISBN:9780306476228.
- [47] S.M.Sze, K.K.Ng. *Physics of Semiconductor Devices*. John Wiley Sons, 2006. ISBN: 9780471143239.
- [48] M.Sykora. *Tests of Semiconductor Detectors for ATLAS Upgrade*. Faculty of Mathematics and Physics - Charles University, 2017.
- [49] M.Moll. *Radiation damage in silicon particle detectors : microscopic defects and macroscopic properties*. Hamburg : DESY, 1999.
- [50] G.Lindstrom. *Radiation damage in silicon detectors*. Nucl. Instrum. Methods A 512 30–43, 2003. doi:10.1016/S0168-9002(03)01874-6.
- [51] F.Hartmann. *Evolution of Silicon Sensor Technology in Particle Physics*. 2nd Edition, 2017. ISBN:978-3-319-64434-9.

- [52] J.Cotterill. *Hybrid Readout Testing of the ABCN250 ASIC for the Phase-II ATLAS Tracker Upgrade*. University of Birmingham. Year 4 Project Report, 2016.
- [53] H.Spieler. *Semiconductor Detector Systems*. Oxford University Press, 2005. ISBN: 9780198527848.
- [54] J.T.Taylor, et al. *A new silicon tracker for proton imaging and dosimetry*. Nucl.Instrum.Meth.A, 2016. doi:10.1016/j.nima.2016.02.013.
- [55] J.T.Taylor, et al. *Proton tracking for medical imaging and dosimetry*. Jinst, 2014. doi:10.1088/1748-0221/10/02/C02015.
- [56] R.Coath. *Advanced Pixel Architectures for Scientific Image Sensors*. Rutherford Appleton Laboratory, STFC.
- [57] W.Snoeys. *CMOS monolithic active pixel sensors for high energy physics*. Nucl. Instrum. Methods A 765 167-171, 2014. doi:10.1016/j.nima.2014.07.017.
- [58] M.Yang, et al. *Comprehensive analysis of proton range uncertainties related to patient stopping-power-ratio estimation using the stoichiometric calibration*. Phys.Med.Biol. 57:4095–4115, 2012. doi:10.1088/0031-9155/57/13/4095.
- [59] A.A.Mustafa, D.F.Jackson. *The relation between x-ray CT numbers and charged particle stopping powers and its significance for radiotherapy treatment planning*. Physics in Medicine and Biology 28. 169, 1983.
- [60] H.Li, et al. *Robust optimization in intensity-modulated proton therapy to account for anatomy changes in lung cancer patients*. Radiother Oncol. 2015;114(3):367-372, 2015. doi:10.1016/j.radonc.2015.01.017.
- [61] Y.Z.Szeto, et al. *Effects of anatomical changes on pencil beam scanning proton plans in locally advanced NSCLC patients*. Radiother Oncol. 2016;120(2):286-292, 2016. doi:10.1016/j.radonc.2016.04.002.

- [62] C.Kurz, et al. *Comparing cone-beam CT intensity correction methods for dose recalculation in adaptive intensity-modulated photon and proton therapy for head and neck cancer*. Acta Oncologica, 54:9, 1651-1657, 2015. doi:10.3109/0284186X.2015.1061206.
- [63] U.Schneider, et al. *The calibration of CT Hounsfield units for radiotherapy treatment planning*. Physics in Medicine and Biology 41. 111-124, 1996.
- [64] R.P.Johnson. *Review of medical radiography and tomography with proton beams*. Rep. Prog. Phys. 81. 016701, 2018. doi:10.1088/1361-6633/aa8b1d.
- [65] Y.Saraya, et al. *A Fast Experimental Scanner for Proton CT: Technical Performance and First Experience With Phantom Scans*. IEEE Transactions on Nuclear Science, vol. 63, no. 1, pp. 52-60., 2016. doi:10.1109/TNS.2015.2491918.
- [66] R.P.Johnson, et al. *Study of spatial resolution of proton computed tomography using a silicon strip detector*. Nucl. Instrum. Methods A 735, 485-489., 2014. doi:10.1016/j.nima.2013.09.051.
- [67] Md.Naimuddin, et al. *Development of a proton Computed Tomography detector system*. Jinst 11, 2016. doi:10.1088/1748-0221/11/02/C02012.
- [68] M.Esposito, et al. *PRaVDA: The first solid-state system for proton computed tomography*. Phys Med. 2018; 55:149-154., 2018. doi:10.1016/j.ejmp.2018.10.020.
- [69] M.Scaringella, et al. *The PRIMA (PRoton IMAGING) collaboration: Development of a proton Computed Tomography apparatus*. Nucl. Instrum. Methods A 730, 178-183., 2013. doi:10.1016/j.nima.2013.05.181.
- [70] pCT Collaboration. Accessed January 2021. http://scipp.ucsc.edu/pCT/about_us.html.
- [71] Wellcome Trust. Accessed January 2021. <https://wellcome.org>.

- [72] S.Manger. *The application of proton computed tomography to reduce proton therapy range uncertainties*. PhD Thesis, University of Warwick, 2018. <http://wrap.warwick.ac.uk/129257>.
- [73] University of Birmingham MC40 Cyclotron. Accessed January 2021. <https://www.birmingham.ac.uk/research/activity/nuclear/about-us/facilities/mc40-cyclotron-facility.aspx>.
- [74] iThemba Labs. Accessed January 2021. <https://tlabs.ac.za>.
- [75] P.Arce, et al. *Report on G4-Med, a Geant4 benchmarking system for medical physics applications developed by the Geant4 Medical Simulation Benchmarking Group*. International Journal of Medical Physics Research and Practice., 2020. doi:10.1002/mp.14226.
- [76] M.Novak. *Physics I.: Physics Lists*. First Geant4 Tutorial Workshop at Instituto de Física da Universidade de São Paulo, Accessed January 2021. <https://indico.cern.ch/event/776050/contributions/3237925/attachments/1789252/2914238/PhysLists.pdf>.
- [77] OPTIma: Optimising Proton Therapy through Imaging. Accessed January 2021. <https://gtr.ukri.org/projects?ref=EP%2FR023220%2F1>.
- [78] T.Price, et al. *WP 11.5: University of Birmingham MC40 Cyclotron*. Presentation, AIDA-2020 2nd Annual Meeting, Paris, 2017.
- [79] Geant4 Material Database. Accessed January 2021. <https://geant4-userdoc.web.cern.ch/UsersGuides/ForApplicationDeveloper/html/Appendix/materialNames.html>.
- [80] W.A.Cote. *Chemical Composition of Wood*. In: *Principles of Wood Science and Technology*. Springer, Berlin, Heidelberg., 1968. doi:10.1007/978-3-642-87928-9_2.

- [81] National Center for Biotechnology Information. *PubChem Compound Summary for CID 16211032, Cellulose*. Accessed January 2021. <https://pubchem.ncbi.nlm.nih.gov/compound/Cellulose>.
- [82] National Center for Biotechnology Information. *PubChem Compound Summary for CID 73555271, Lignin, organosolv*. Accessed January 2021. https://pubchem.ncbi.nlm.nih.gov/compound/Lignin_-organosolv.
- [83] A.D.Silva, S.Kyriavidea. *Compressive response and failure of balsa wood*. Elsevier. International Journal of Solids and Structures. 44:8685-8717, 2007.
- [84] M.Esposito, et al. *A large area CMOS Active Pixel Sensor for imaging in proton therapy*. Jinst 13 P11017., 2018. doi:10.1088/1748-0221/13/11/P11017.
- [85] I.Sedgwick, et al. *LASSENA: a 6.7 megapixel, 3-sides buttable wafer-scale CMOS sensor using a novel grid- addressing architecture*. Proc Int Image Sens Work.3-6., 2013.
- [86] M.Esposito, et al. *DynAMITe: a wafer scale sensor for biomedical applications*. Jinst, 2011. doi:10.1088/1748-0221/6/12/C12064.
- [87] G.Poludniowski, et al. *Proton computed tomography reconstruction using a backprojection-then-filtering approach*. IOP. Physics in Medicine and Biology. 59:7905-7918, 2014.
- [88] V. Highland. *Some practical remarks on multiple scattering*. Medical Physics , 43 (11) pp. 6129-6136., 2016. doi:10.1118/1.4965809.
- [89] G.R.Lynch, O.IDahl. *Approximations to Multiple Coulomb Scattering*. Nucl. Instrum. Methods B58, 6, 1991. Eq. 12.
- [90] M.Geisel-Brinck. *Revision of the multiple scattering algorithms in PROPOSAL*. University in Dortmund, Germany., 2013.

- [91] B.Gottschalk. *Radiotherapy Proton Interactions in Matter*. 2018. arXiv:1804.00022.
- [92] J.T.Taylor, et al. *An experimental demonstration of a new type of proton computed tomography using a novel silicon tracking detector*. *Medical Physics*, Vol.43, No.11, 2016. doi:10.1118/1.4965809.
- [93] University Hospitals Birmingham NHS Foundation Trust. Accessed January 2021. <https://www.uhb.nhs.uk>.